In-line Tapered Fiber Mach-Zehnder Interferometer for Biosensing Applications

By

Maryam Alharbi

A Thesis Submitted in Partial Fulfillment of
the Requirements for the Degree of

Master of Science

Department of Physics and Physical Oceanography
Memorial University of Newfoundland

May 2018

St. John's Newfoundland

Abstract

Due to the advantages of compact size, light weight, immunity to electromagnetic interference and remote sensing, optical fiber sensors have been studied extensively since the 60s. In particular, interferometric Mach-Zehnder fiber sensors are favourable for their flexibility and high sensitivity. The principle of operation for these sensors bases upon the interference between the light propagation in the core mode and the excited cladding modes. The work presented in this thesis focuses on the fabrication of tapered Mach-Zehnder interferometer in a single-mode fiber and its applications in biosensing.

In this study, two kinds of tapered fiber Mach-Zehnder interferometer, either symmetric or asymmetric, have been fabricated using fusion splicing technique. In both cases, the effects of varying the waist diameter, separation distance between tapers, and propagation direction are studied. The symmetrical tapered fiber Mach-Zehnder interferometer has been explored for biosensing applications. Using the dipping layer-by-layer method, multiple thin films have been deposited on the fiber structure for the detection of streptavidin which is a common target material used to test the effectiveness of a biosensor. The sensing mechanism here relies on the electrostatic attraction between cationic and anionic materials, in which the cationic material used in this study is poly (allylamin hidrocloride) (PAH). While, the anionic material adopted here is either SiO_2 core/Au shell nanoparticles or poly (sodium 4-styrenesulfonate) (PSS). For the best of our knowledge, this is the first time the tapered fiber Mach-Zehnder interferometer is used for streptavidin sensing by applying the layer-by-layer technique.

Two types of multilayered structure are fabricated on the tapered region of the fiber interferometer. The first multilayered structure consists of SiO_2:Au nanoparticles, in which the deposition of a monolayer of the PAH polymer and a monolayer of the negatively charged SiO_2:Au NPs represents a single bilayer of (PAH/SiO_2:Au NPs). The second multilayered structure bases on the deposition of PAH and PSS polymer. Following the fabrication of the multilayered structures is the functionalization with biotin which is a vitamin that possesses a strong binding ability with streptavidin so it functions as an adhesive material to streptavidin. The sensing response of the sensors on detecting aqueous solutions of streptavidin has been observed by measuring the shift in the wavelength of the transmission spectrum of the tapered fiber interferometer. The effects of depositing (PAH/SiO_2:Au NPs) and (PAH/PSS) films in multilayered structures, as well as the influences of different device specifications are investigated.

Acknowledgments

I would like to thank my supervisors Dr. Qiying Chen and Dr. Liqiu Men for granting me the opportunity to be part of the research group, the guidance, instructions that helped me to learn, explore and succeed in finishing this work.

I would like to thank the Saudi Cultural Bureau for the scholarship and funding of this research work.

Endless thanks to my beloved family for their continuous support, especially my husband, Alaa Althmaeri, for being the greatest source of energy, comfort and encouragement throughout the course of my research and studies.

Table of Contents

List of Tables

List of Figures

List of Abbreviations

FOS	Fiber-Optic Sensors
RI	Refractive Index
FBG	Fiber Bragg Grating
SMF	Single-Mode Fiber
MMF	Multi-Mode Fiber
FPI	Fapry-Perot Interferometer
MZI	Mach-Zehnder Interferometer
TFMZI	Tapered Fiber Mach-Zehnder Interferometer
SFMZI	Symmetrical Fiber Mach-Zehnder Interferometer
AFMZI	Asymmetrical Fiber Mach-Zehnder Interferometer
LPG	Long Period Grating
PAH	Poly (allylamin hidrocloride)
SV	Streptavidin
LBL	Layer-By-Layer
ISAM	Ionic Self-Assembly Monolayer
ESA	Electrostatic Self-Assembly
LB	Langmuir-Blodgett
PSS	Poly (sodium 4-styrenesulfonate)
NPs	Nanoparticles
OSA	Optical Spectrum Analyzer
PCBS	Poly {1-[4-(3-carboxy-4 hydroxyphenylazo)-benzensulfonamido]-1, 2-ethanediyl, sodium salt}
FSR	Free Spectral Range

Chapter 1

Introduction

Fiber optic sensor technology has brought an innovative solution to many problems in the sectors of transportation, industry, entertainment and medical technology due to their merits of remote ability sensing, small size and enormous advantages. The 1960s witnessed the birth of a huge interest in fiber-optic sensors technology. Intensive research and experimental work accompanied such interest to achieve better performance devices with lower energy loss. Researches in the following decade managed to develop these sensors and took a step further in marketing fiber-optic sensors and implement the technology in different applications [1]. Such interest on developing optical fiber sensors continues until present time. Fiber-optic sensors are possibly found to be used in monitoring and evaluation

of damaged structures in dams and bridges. They also can be utilized to evaluate the function of airplanes wings and oil pipelines conditions [1]. In optical fiber sensors, electromagnetic waves emitted from a light source will be guided in the fiber and interacted with the surrounding environment which can be biological, chemical, or physical nature. As a result of the interaction, a modulated signal will be generated, which propagates along the fiber to reach a detector with information about the target. Diverse types of fiber optic sensors were invented to measure different parameters. Some examples of these sensors are strain, pressure, temperature, acceleration, humidity and biological sensors [1].

In this chapter, general information will be introduced on the basic structures of optical fibers, their role as sensors and their types and classifications. Furthermore, interferometric fiber sensors such as Fabry-Perot, Mach-Zehnder, Michelson and Sagnac interferometers will be discussed briefly. This will be followed by coating fibers with thin films, its advantages and drawbacks and some of their coating techniques. Nevertheless, different approaches to apply the layer-by-layer technique will be discussed then a brief review on the work that have been done about optical fiber sensors coated with thin films will be given followed by a discussion on the motivation behind this thesis and an outline of the material.

1.1 Optical Fibers

Optical fibers function as waveguides that allow propagating light to travel for a long distance through the modification of the refractive index (RI) of the fibers. Usually, an optical fiber has an inner part which is known as the core and surrounded by an outer part called the cladding, as illustrated in Fig. 1-1 [2]. Silica (SiO_2) is usually used to fabricate conventional optical fibers. Both the core and cladding are made of either glass, crystals, or polymers relying on the application of the fiber [1]. The cladding has a lower refractive index than that of the core [3, 6]. Some chemical materials, such as aluminum oxide (Al_2O_3), titanium dioxide (TiO_2) [38], germanium dioxide (GeO_2), and phosphorus pentoxide (P_2O_5) are doped into the core for the purpose of increasing its refractive index. However, the cladding is not doped with any material [4, 5]. The difference between the refractive indices of the core and cladding is denoted as Δn. The cladding is surrounded by a protective layer (buffer) that is made of a polymer with a higher refractive index. Usually, most of the light is confined in the core but a small portion of it propagates along the cladding and lost outside of the fiber because of the transmission from the lower refractive index region (cladding) to a medium of higher refractive index (buffer) [2]. Sometimes, the core is kept without being doped, but the cladding is doped with materials such as boron trioxide (B_2O_3) to decrease its refractive index [4, 5].

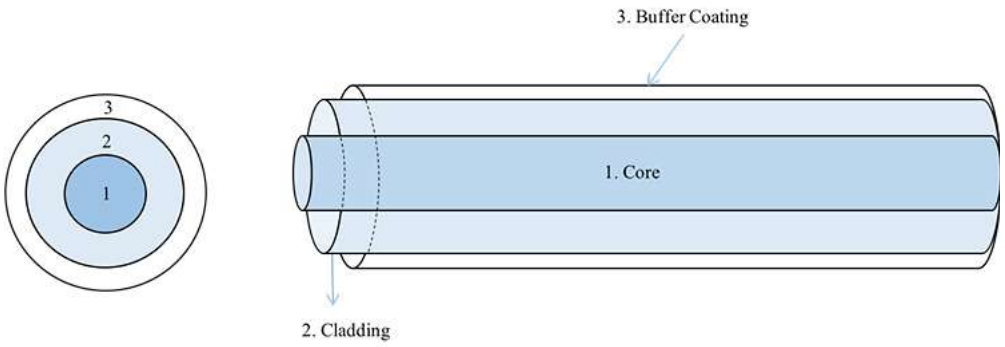

Figure 1-1 Basic structure of an optical fiber.

The common types of optical fibers are divided into single-mode fibers (SMFs) and multi-mode fibers (MMFs). Only one mode travels through single-mode fibers while more than one mode are supported by multi-mode fibers [7]. Typically, a single-mode fiber has a core diameter < 12 μm while its cladding diameter is 125 μm. On the other hand, a multi-mode optical fiber has a core diameter > 20 μm [2].

When light travels along an optical fiber, it obeys the principle of total internal reflection due to the difference in the refractive indices of the fiber layers. In general, if light propagates from a medium (1) with a higher refractive index into a second medium (2) with a lower refractive index, it experiences a refraction when the incidence angle $\theta_{inc} < \theta_c$, where θ_c is the critical angle, it overlaps the normal between the two media when $\theta_{inc} = \theta_c$, or it reflects totally into the medium (1) when $\theta_{inc} > \theta_c$, as Fig. 1-2 shows. In other words, light propagating inside the fiber will be totally confined to the core when $\theta_{inc} > 90^o$ [7].

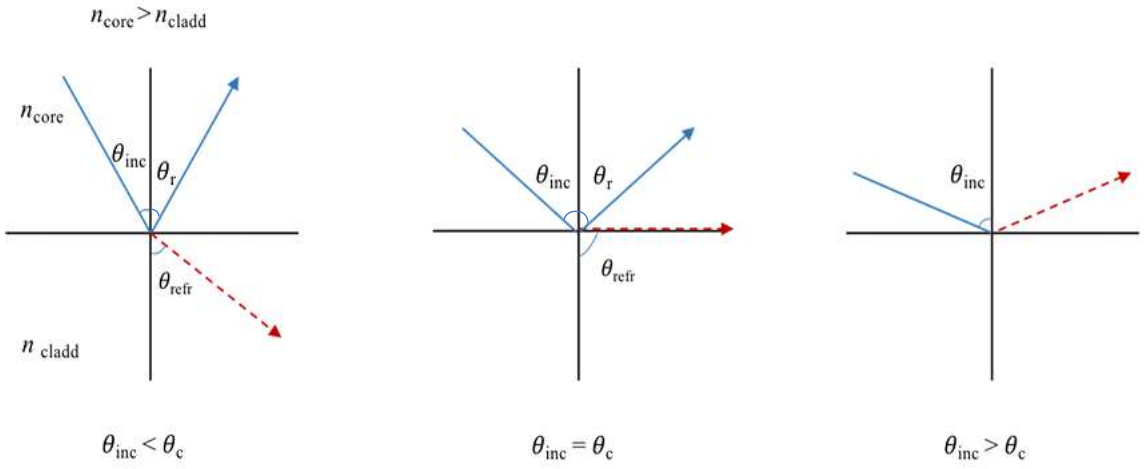

Figure 1-2 Total internal reflection in an optical fiber.

1.2 Optical Fiber Sensors

Due to the development of optical fiber sensors, the opportunity for applying them in different and diverse fields such as the field of chemistry, physics, medicine and telecommunication systems became available [8]. Fiber-optic sensors can possibly be used for detecting strain [9], temperature [10, 11], pressure [12], liquid level [13], refractive index [14-16] and many other parameters. Owing to their unique features such as their ability for remote sensing, to perform under harsh environment, their small size, low signal loss, and immunity to electromagnetic interference, they replaced the conventional electrical and electronic sensors in many applications [8].

1.2.1 Components of Fiber-Optic Sensors

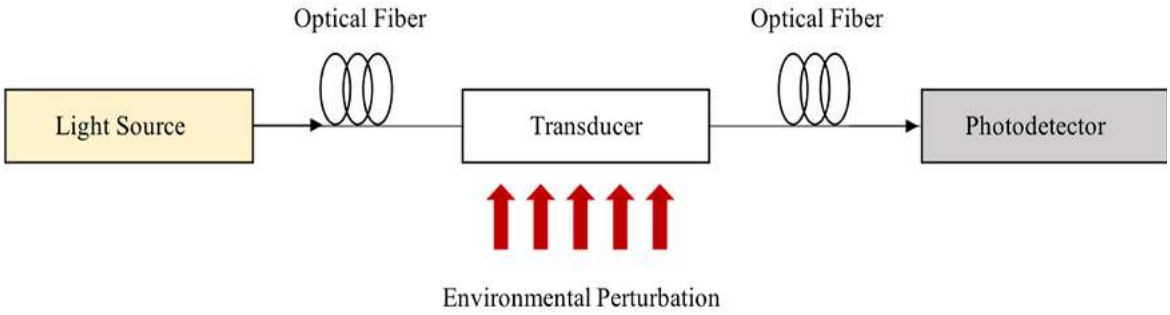

Figure 1-3 Key components in an optical fiber sensor.

Figure 1-3 shows a schematic representation of the key components in an optical fiber sensor. It is worth mentioning that the light source can be a light-emitting or laser. Moreover, the optical fiber can be a single-mode fiber (SMF) or a multi-mode fiber (MMF). In addition to that the transducer (modulator) is a component utilized to convert the measured perturbations to optical signals. Finally, the photodetector, such as an optical spectrum analyzer (OSA), detects the modulated signal [6-8].

1.2.2 Types of Optical Fiber Sensors

Optical fiber sensors can be mainly categorized into four different types. The first type is based on the sensing location where fiber sensors can be either intrinsic or extrinsic [17]. If the fiber itself works as an element to sense the environmental changes and at the same time functions as a carrier of the modulated data, the sensor is described as intrinsic.

On the other hand, when the fiber just transmits the light from a point to another but another optical element is used to detect the changes in the environment, the sensor is found to be extrinsic [17-19]. The second type is based on the property of the electromagnetic wave that is modulated. When an external perturbation modulates the intensity of the light, the sensor then is described to be intensity modulated [17]. There are many reasons to induce the modulation of intensity such as micro and macro bending of the fiber, reflection of the transmitted signal and transmission of light through different media. As a result of the intensity loss caused by those factors, intensity-modulated sensors became unreliable [1]. Other properties of the light can be modulated like the phase, wavelength and polarization states. Phase modulated or interferometric sensors among other sensors are extremely sensitive to the perturbations in the outside environment. In this type of sensors, light passes through two separated arms. One of the arms is exposed to the external environment while the other arm is not. The phase of the light signal that propagates through the first path undergoes changes. Nevertheless, the detected signal from the other path is used as a reference. The two beams are then combined to produce an interference in the output signal [1]. Moreover, when the wavelength of light changes because of the exposure to external environment, the sensor is described as a wavelength modulated fiber-optic sensor. One of the most common sensors of this type is called fiber Bragg grating (FBG) sensor. To form this type of sensors, a periodic structure is inscribed in the core in order to generate changes in its refractive index [20]. The third type of fiber-optic sensors is based on their uses. For instance, sensors that detect temperature, stress and other physical parameters are called physical sensors while those which measure blood flow or pH content are biomedical and chemical sensors, respectively [17]. Finally, based on their range of sensing fiber-optic

sensors are classified into point-by-point, distributed, and quasi-distributed sensors [21]. If the sensor detects the changes that are located at the end of the fiber, it is described as a point-by-point sensor. In contrast, distributed sensors can detect any environmental perturbations at any point along the entire fiber. Quasi-distributed sensors allow the measurement along the fiber only at certain sensitized and discrete points [17].

1.3 Interferometric Optical Fiber Sensors

1.3.1 Fabry-Perot Interferometer

Fabry-Perot interferometer sensors or etalons consist typically of two parallel mirrors that reflect part of the light and transmit the rest of it to the end of the fiber. The two mirrors can be formed either inside or outside the fiber. When they are formed outside the fiber with a cavity in between, the sensor is extrinsic, but when the reflectors are built inside the fiber, the sensor is considered to be intrinsic [22]. The cavity of an extrinsic Fabry-Perot interferometer can be formed by cleaving two fibers ends and inserting them in a cylinder facing each other with an air cavity in between, as illustrated in Fig. 1-4(a) [23]. In other cases, a polymer can be used as a cavity material. The air-cavity based fiber Fabry-Perot interferometer sensors are insensitive to temperature. Therefore, they can be used for refractive index, pressure and strain detection owing to the low thermal expansion coefficient of air. Polymer-cavity based fiber Fabry-Perot interferometer sensors can be built to meet specific needs such as sensing of high temperature and detection of molecules [24]. In spite of the fact that the fabrication of extrinsic Fabry-Perot interferometers is

considered to be relatively simple and inexpensive, their sensors are found to be problematic in terms of packaging, their coupling efficiency are found to be low and they indeed require cautious alignment. [24]. Figure 1-4(b) shows the intrinsic type of interferometric Fabry-Perot. In the intrinsic fiber Fabry-Perot interferometer, the method of directly fabricating the mirror into the fiber is carried out by cleaving the fiber, coating the end using titanium dioxide followed by splicing [23]. Because of the constant light passage inside the fiber, the intensity of a transmitted signal through this type of sensors is higher than that received signal when using an extrinsic Fabry-Perot interferometer. However, the drawbacks of these sensors are limited in their need of expensive cavity formation equipment [24].

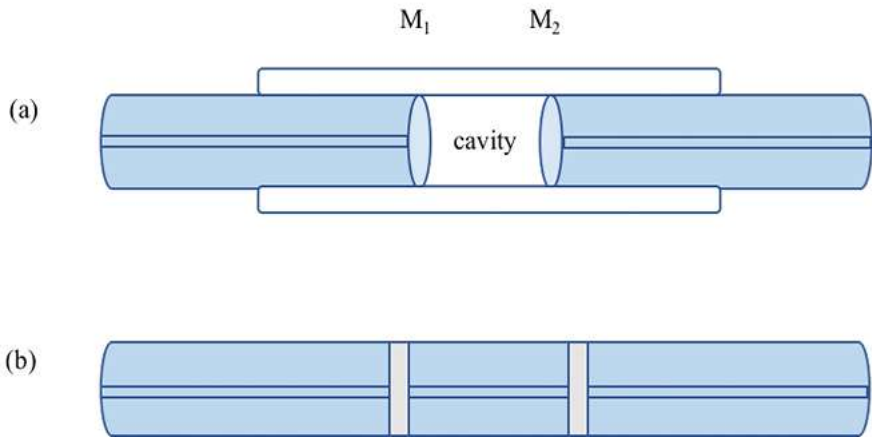

Figure 1-4 Types of Fabry-Perot Interferometer sensor: (a) extrinsic; (b) intrinsic. M_1, M_2: mirrors.

As a result of interfering the transmitted and reflected beams between the two reflectors, an interference pattern will occur, as shown in Fig. 1-5. When exposing the Fabry-Perot interferometer sensor to external perturbations, the optical path difference will change causing a shift in the phase of the interference pattern. The phase difference is expressed by the equation [22]:

$$\Delta\phi_{\mathrm{FPI}} = \frac{4\pi nL}{\lambda} \tag{1-1}$$

where n is the refractive index of the material forming the cavity, L is the cavity length, and λ is the wavelength of the light source.

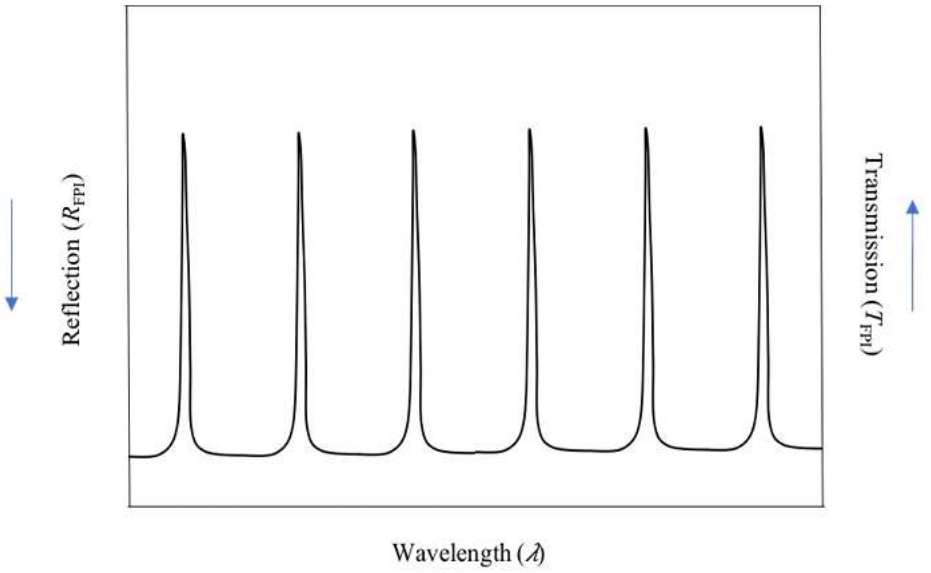

Figure 1-5 Transmission and reflection spectra of a Fabry-Perot interferometric sensor.

1.3.2 Mach-Zehnder Interferometer

Owing to its flexibility, the Mach-Zehnder interferometer has been applied extensively in various sensing applications. Figure 1-6 illustrates a typical Mach-Zehnder

interferometric sensor. It consists of two separated arms where one of them is exposed to the environmental perturbations and it is called the sensing arm. The other arm is isolated from the environmental effects and it is known as the reference arm. The sensing and reference arms are joined with two 3 dB couplers. The first coupler acts as a splitter of the light beam. It splits the beam from the light source into two equal beams where one of them travels through the sensing arm and its intensity is modulated due to the exposure to external changes. The other beam, which travels through the reference arm, will not experience a modulation due to its isolation from external changes. Then, the two beams are combined with the second coupler causing an interference pattern in the detected output signal, as shown in Fig. 1-7 [22].

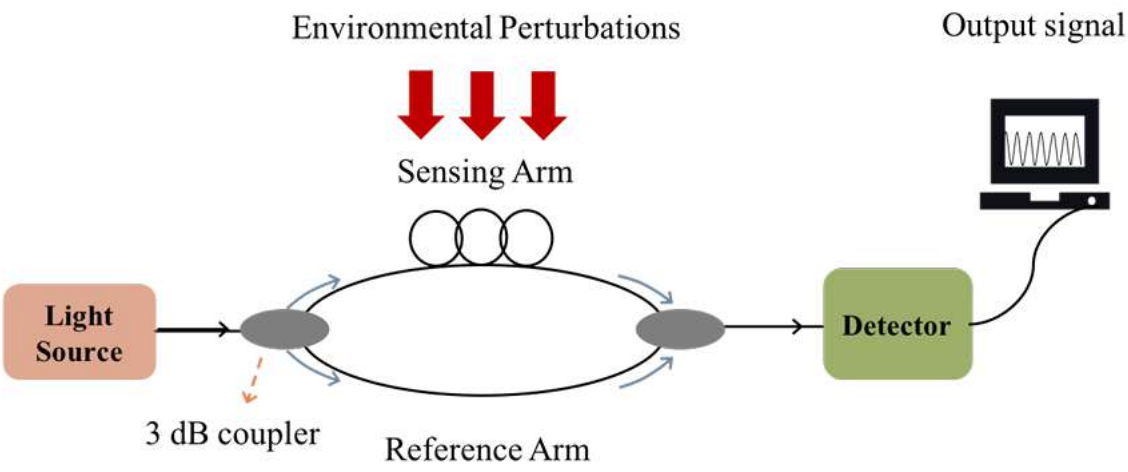

Figure 1-6 Illustration of a Mach-Zehnder interferometric sensor.

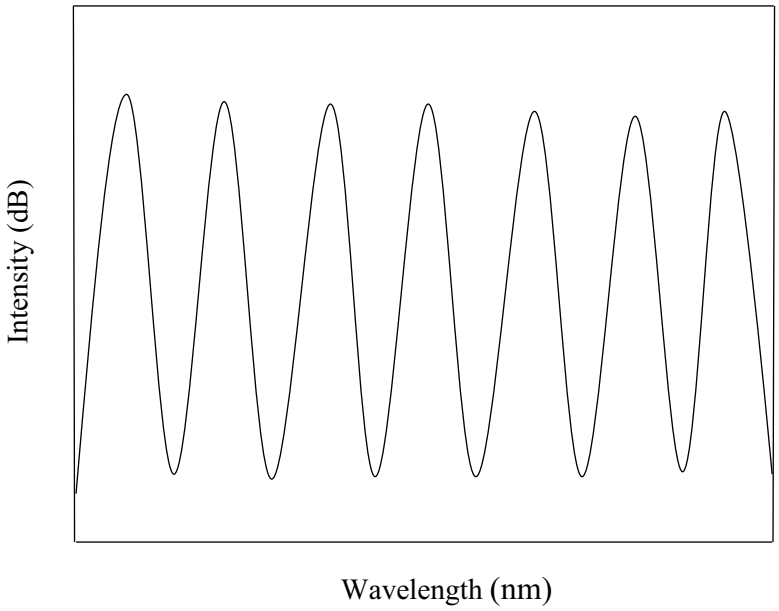

Figure 1-7 Interference pattern of a Mach-Zehnder interferometric sensor.

Since the discovery of LPGs, the typical structure of the fiber Mach-Zehnder interferometer has been replaced with an in-line Mach-Zehnder interferometer [22]. Also, a Mach-Zehnder interferometer can be formed using two pairs of tapers [25-28], double cladding fiber sandwiched between single-mode fibers [29, 30], core offset [31] and peanut-shape structure [32, 33]. It can also be designed by using two different configurations where a taper with a core offset and a multi-mode fiber with a peanut-shape structure are utilized to form the Mach-Zehnder interferometer, respectively [34, 35]. These examples are illustrated in Fig. 1-8.

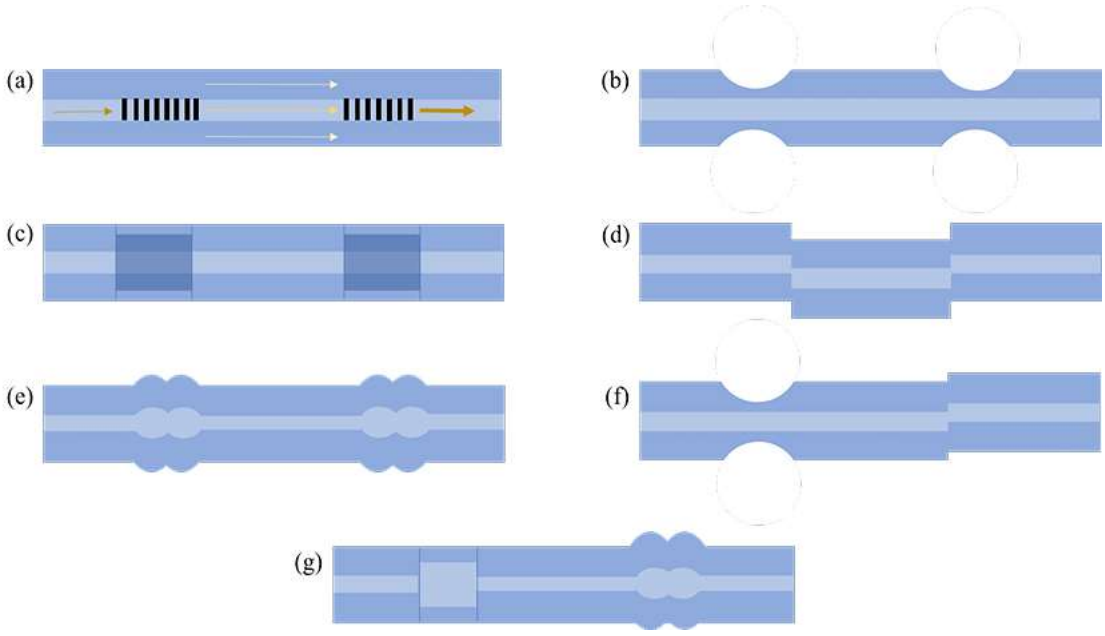

Figure 1-8 Some types of in-line fiber MZI sensors based on: (a) LPG; (b) tapers; (c) double cladding fiber; (d) core offset; (e) peanut shape structure; (f) taper and core offset; and (g) multi-mode fiber and peanut shape structure.

In in-line Mach-Zehnder interferometric sensors, the light propagating in the fiber splits into two modes through the first element (e.g., LPG, or a taper). Part of the light will remain propagating in the fundamental core mode while the other part will be excited into higher order cladding modes. The two beams then will be recombined by the other element and interfere with each other [22].

1.3.3 Michelson Interferometer

The conventional Michelson interferometer consists of a coupler and two arms that end up with reflectors, as shown in Fig. 1-9. It is very close to the Mach-Zehnder interferometer in terms of its fabrication techniques and principle [1]. Therefore, it can be

described as a folded Mach-Zehnder interferometer. As a result, the amount of the light loss and the form of the output signal in the Michelson and Mach-Zehnder interferometers are found to be identical [17]. One of the variations between these two structures is the requirement of mirrors at the end of the sensing and reference arms and the use of a single coupler to couple and recombine the light reflected from the mirrors at the end of Michelson interferometer legs. Moreover, the Michelson interferometer has a higher sensitivity than that of Mach-Zehnder interferometer since the light passes through the same paths twice causing a double in the phase shift per unit length of the fiber [36]. The conventional structure of Michelson interferometer can be replaced by the in-line structure to reduce its size in which light travels only inside one fiber with one reflector at the end. Light from a light source splits into fundamental and cladding modes through a core-cladding splitter such as long period gratings (Fig. 1-10). Then, both modes will be reflected by the mirror, travel back through the same paths and recombined by the long period grating resulting in an interference pattern [1].

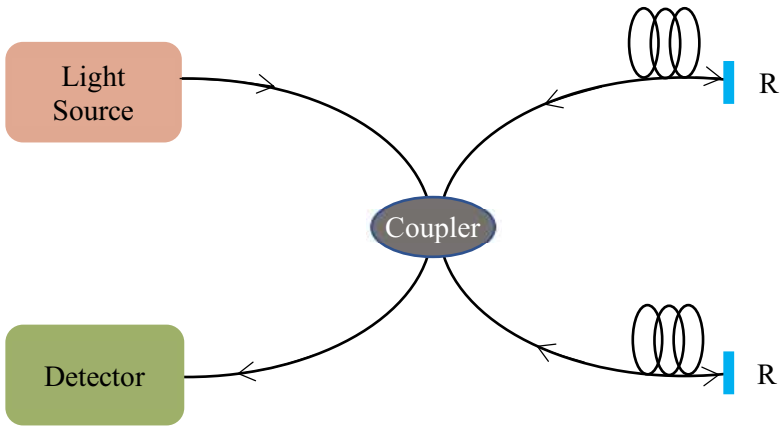

Figure 1-9 Illustration of a conventional Michelson interferometric sensor. R_1, R_2: reflectors (mirrors).

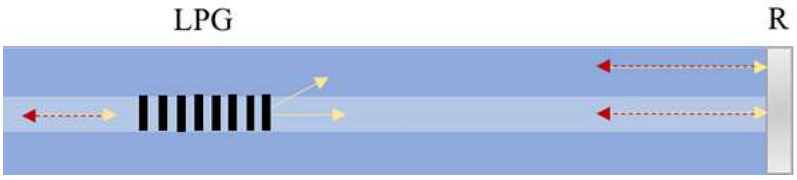

Figure 1-10 An in-line Michelson interferometric sensor based on LPG as a beam splitter.

1.3.4 Sagnac Interferometer

In 1913, the physicist Monsieur Sagnac presented the first Sagnac interferometer that was a powerful tool for gyroscopic and rotation measurement. The applications of this device were then expanded to sensing purposes. Its principle is based on splitting the beam propagating from a light source into two beams by utilizing a beam splitter where the two beams propagate in opposite directions. The counter beams are reflected by several reflectors to interfere with each other causing an interference pattern in the output signal. However, after the invention of lasers at the beginning of the 60s, the ring laser was used for the measurement of rotation [37]. Later, for the replacement purpose of the ring laser and mechanical gyros, the fiber-optic Sagnac interferometer was developed where the need of utilizing the laser as a light source was replaced by the incoherence one [23, 38]. This is due to the fact that fiber-optic Sagnac interferometer has a unique feature in comparison with the other sensors which is the ability of providing the two opposite beams in the same physical path [38]. Commercially, this type of fiber sensors is expressed as one of the most effective tools for different applications specially for optical fiber gyroscopes up to now [1].

Fiber Sagnac interferometer can be used for the measurement of time-varying and slowly-varying parameters such as acoustics and strain. It can be also employed to measure twist, temperature, and pressure [23]. While it is true that the Sagnac interferometric sensor is simple and easy to fabricate, it has the problem of temperature-pressure cross sensitivity. This drawback can be solved by the utilization of polarization-maintaining fibers or highly birefringent fibers as the sensing element [1]. Due to their ability to be used as sensing fibers in maximizing the polarization dependence of the signal within the Sagnac interferometer, polarization-maintaining fibers or highly birefringent fibers are used. A schematic illustration of the Sagnac interferometer is shown in Fig. 1-11. The 3 dB coupler functions as a beam splitter and combiner whereas the polarization controller works to control the polarization of the input signal. The phase emerged as a result of interfering the two adverse beams is given by the equation [1]:

$$\Delta\phi_{\mathrm{SI}} = \frac{2\pi BL}{\lambda} \tag{1-2}$$

where B is the birefringent coefficient of the fiber, L is the length of the fiber, and λ is the wavelength of the light source.

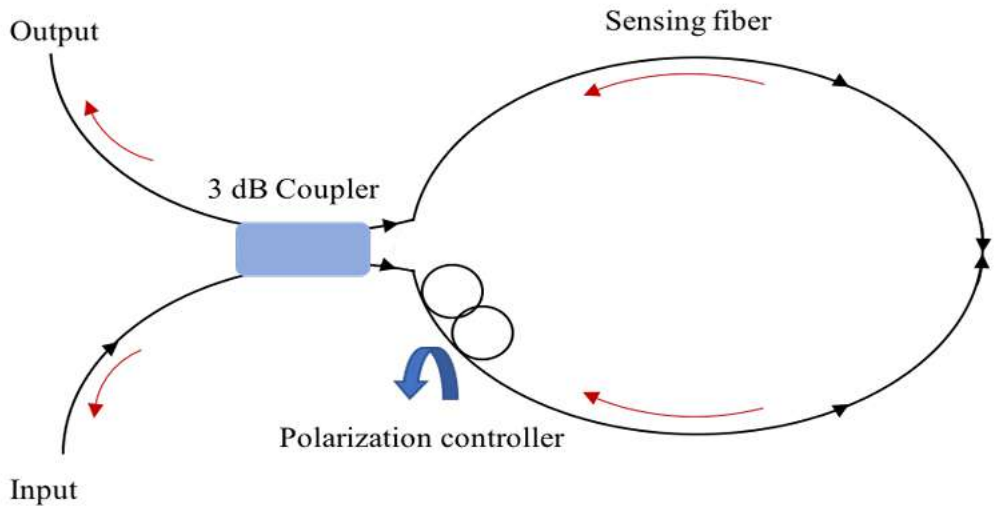

Figure 1-11 Schematic illustration of an optical fiber Sagnac interferometer.

1.4 Optical Fiber Sensors Based on Nanostructured Coatings

Improving the sensitivity of optical fiber sensors toward certain physical or chemical effects can be realized by coating them with nanoparticles or patterns at nanoscale level [39]. Different nanomaterials can be deposited on optical fibers such as nanowires, nanotubes, graphene oxide and nanoparticles.

For instance, Lokman *et al*. presented an in-line Mach-Zehnder interferometer with a dumbbell shape structure which was coated with ZnO nanowires [40]. The sol-gel dip-coating technique was used to coat the nanowires on the optical fiber and the fiber was used for the detection of humidity when it was varied between 35% and 60%. The response of the sensor was investigated through the detection of the reflected transmission spectrum. The results showed that the resonance wavelengths red-shift with increasing the humidity.

Furthermore, the sensitivity of the sensor was enhanced from 0.0002 nm/%RH (before coating ZnO nanowires) to 0.020 nm/%RH (after coating ZnO nanowires).

Moreover, Shivananju *et al*. coated a film based on multi-walled carbon nanotubes on the surface of fiber Bragg gratings using chemical vapour deposition technique [41]. Prior to the film deposition the phase mask technique was used to inscribe gratings of periodicity ~ 532 nm in the core of a single-mode fiber. The fiber was then dipped into a hydrofluoric acid solution in order to etch the cladding. The diameter of the fiber after etching was ~ 4.5 μm. The sensor before the film fabrication was exposed to relative humidity in the range of 20% and 90% at room temperature. The results showed that the Bragg wavelength for the bare sensor remained unchanged with increasing the humidity. However, after the carbon nanotubes coating, the Bragg wavelength shifts linearly with increasing the humidity. The sensor showed a high sensitivity of 31 pm/%RH and limit of detection of 0.03 RH.

Dissanayake *et al.* coated graphene oxide on a long period fiber Bragg grating sensor using dip-coating technique [42]. The fiber was functionalized with 3-(trimethoxysilyl) propyl methacrylate and was then immersed into a solution of graphene oxide. The thickness of the coating was ~ 1.5 μm. The sensor response to the change in humidity, temperature, and external refractive index was examined. It was found that the resonance band intensity increased linearly with increasing the humidity from 60% to 95% at the room temperature. Over this range, the sensitivity of the device is found to be 0.15 dB/%RH. Furthermore, when the humidity was fixed at 45% and the temperature changed from 25 to 70 ºC, the resonance wavelength blue-shifted linearly with increasing the temperature. The sensitivity was found to be 0.32 nm/ºC. Moreover, a nonlinear

increase was observed in the resonance band intensity when the external refractive index increased. The sensitivities of the sensor achieved in two regions of different refractive index were 17 dB/RIU and 55 dB/RIU, respectively. Chiu *et al*. also fabricated a sensor for humidity monitoring using graphene dioxide as a coating. However, here the graphene oxide was coated on the surface of a tilted fiber Bragg grating [43]. The fiber was etched before coating with five different diameters in order to study the effect of the diameter on the sensitivity. These diameters were 20, 35, 50, 55, and 60 μm. The graphene oxide was coated on the gratings by piezoelectric inkjet technology with coating thickness of 1 μm. The samples were then exposed to humidity ranging between 20% and 80%. It was found that increasing the humidity led to a reduction in the refractive index of the coating. As a result, the resonance wavelength shiftes to the shorter wavelength region. The sensor of 20 μm diameter showed the highest sensitivity which was 0.01 nm/%RH.

Nanoparticles were widely adopted in diversity of applications due to their unique features [44]. They have special physical, chemical and electronic properties that differentiate them from the bulk materials as a result of their small size. Also, it is possible to utilize these particles to build and improve different sensing tools, particularly, biological and electrochemical sensors [44]. In terms of the biosensors, nanoparticles can be employed for immobilization and labeling of biomolecules. They are suitable for biomolecules immobilization owing to the high free energy of their surfaces and large specific surface area. Furthermore, due to the fact that they are charged, nanoparticles have the ability to adsorb biomolecules with opposite charges by the electrostatic force. Also, nanoparticles can maintain the bioactivity of the biomolecules when they are adsorbed onto their surfaces.

Unlikely, when they are adsorbed onto the surface of bulk materials, the biomolecules will probably lose their bioactivity [44].

Liu *et al*. fabricated a s-tapered optical fiber sensor which was coated with SiO_2 nanoparticles for humidity monitoring [45]. The nanoparticles were simply coated on the fiber by immersing the fiber into a solution containing SiO_2 nanoparticles for two minutes following that with drying. The sensor was exposed to relative humidity ranging between 26.5% and 95.2%. It was found that increasing the humidity led the transmission peaks to shift to the longer wavelength region. The response was obvious when the relative humidity was ranging between 83.8% and 95.2% which made the device to be potentially applicable in high humidity and harsh electromagnetic environments.

Different techniques can be applied to fabricate nanostructured coatings on optical fibers such as sol-gel dip-coating, chemical or physical vapour deposition, spin coating, Langmuir-Blodgett and layer-by-layer techniques. The disadvantages of the sol-gel technique are its requirement of using specific chemical compounds and its inability to provide a precise thickness control. On the other hand, volatile or toxic chemicals are used in the chemical vapour deposition technique as well as costly equipment. Furthermore, the physical vapour deposition technique is usually used to coat materials on planar surfaces. As a result, fabricating uniform coatings on the cylindrical structure of an optical fiber requires an additional work. Similarly, the spin-coating technique requires a treatment of the fiber to make its surface flat like the D-shaped fiber [39].

The Langmuir-Blodgett approach relies upon the building of organic monolayer films on a sub-phase. Those layers are then transferred one by one onto a hard substrate by passing it vertically through them [46-48]. This technique provides uniform and

homogenous coatings on optical fibers. However, limited species of chemicals can be used to form the coatings. Furthermore, only a few layers can be fabricated using this technique because of the defects in the resulted structure. Moreover, it requires special equipment [39]

The layer-by-layer technique is based upon the formation of multilayered films by the electrostatic interaction between cationic and anionic materials, in which a solid substrate is dipped alternatively into these two materials to form the film [46,49]. Similar to the Langmuir-Blodgett technique, the layer-by-layer electrostatic self-assembly technique can be used to form thin and homogeneous coatings on optical fibers. However, unlike the Langmuir-Blodgett technique the layer-by-layer electrostatic self-assembly does not require special equipment so it can be carried out at room conditions [39]. For instance, Zhen used the layer-by-layer electrostatic self-assembly technique to fabricate a nano-structured coating on a long period fiber grating for moisture sensing [40]. Two nanofilms were deposited on the optical fiber. The first nanofilm was based on polyallylamine hydrochloride (PAH^+) and polyacrylic acid (PAA^-). However, the second nanofilm was based on aluminium oxide ($Al_2O_3^+$) and poly (sodium 4-styrenesulfonate) (PSS^-). Initially, the PAH^+/PAA^- film was coated on the fiber to enhance the sensitivity of the sensor. The $Al_2O_3^+/PSS^-$ film was then coated on the PAH^+/PAA^- to increase the selectivity of the sensor. The sensor was exposed to relative humidity in the range between 20% and 90%. The sensor showed total wavelength and intensity shifts of -3.6 nm and 7.0 dBm, respectively which were higher than the shifts obtained for the bare long period fiber grating.

1.5 Layer-By-Layer Electrostatic Self-Assembly

The layer-by-layer electrostatic self-assembly was presented initially by Decher and Hong in the early 90s. Films with monolayers or multilayers can be created using this method. It offers many merits like the low-cost, simplicity and rapidness. In addition, substrates with diverse types, shapes and sizes can be used to form ultrathin coatings with desired properties. Furthermore, many kinds of materials can be utilised for carrying out the layer-by-layer electrostatic self-assembly technique. Organic or inorganic charged polyelectrolytes and charged nanoparticles are some types of those materials. The layer-by-layer technique can be applied in three different ways to form thin films which are dipping, spin-assisted and spray-assisted [50].

The dipping layer-by-layer method involves dipping a charged substrate in a colloidal solution that has an opposite charge to form a single layer on the surface. As a result, the surface charge changes and then the substrate is dipped in another solution with an opposite charge than the one of the surface forming a bilayer. After the adsorption of each layer, the substrate is dipped in water to get rid of unbounded molecules and dried if needed. To form a film with multilayers, the substrate is immersed alternatively between the two colloidal solutions. This method does not need any activation steps to adhere the materials because the electrostatic attraction between the oppositely charged components leads the interlayers to adhere strongly [50].

The spin-assisted layer-by-layer method requires the use of a spin coater, in which a substrate with the required quantity of colloidal solution is placed in the machine and rotated very fast. A monolayer is formed on the whole surface of the substrate due to the

centrifugal force caused by the fast spinning. In this approach, the monolayer is developed within seconds. Then, droplets of another solution are placed on the substrate and spin-coated to form a bilayer. When an alternate spin-coating of the two solutions is performed a multilayered film can be obtained. Washing and drying the substrate between deposition steps is required. The advantages of this approach are the fast film formation and smooth coatings. Also, the thickness of the film using this approach grows linearly in contrast to the case of dipping layer-by-layer, in which exponential growth is commonly observed [51]. On the other hand, the disadvantages of such approach are formed in the limitation of the surfaces that can be used to perform the spin-assisted technique where only flat surfaces are allowed. Moreover, it is found to be difficult to fabricate thin and uniform films on large surfaces. Particularly, by the use of aqueous solutions [52].

In the spraying-assisted layer-by-layer, a charged substrate is sprayed alternatively with positive and negative colloidal solutions for thin films formation. The washing process is performed by spraying the substrate with water after each deposition cycle. This technique is fast as a bilayer can be formed within seconds and applicable on substrates with different shapes and sizes [50]. By tuning the parameters of these processes such as the (immersion, spinning and spraying) time, components, concentrations and PH, films with different properties can be fabricated [50].

In the case of optical fiber sensors, the dipping layer-by-layer approach is commonly used. For example, Korposh *et al*. fabricated a chemical sensor based on PDDA/SiO_2 nanoparticles [53]. The film was coated on the surface of a long period fiber grating with 30 mm length and 100 μm periodicty. Ten layers of PDDA/SiO_2 NPs were coated on the long period gratings region. The results showed that the sensitivity of the

sensor enhanced after the deposition of the film. Also, the spectrum shifted towards the shorter wavelength region and the change increased with increasing the number of layers after the deposition of the film. The thickness of one layer was 46±3 nm. The sensor was then exposed to tetrakis-(4-sulfophenyl) porphine solution of different concentrations which causes the refractive index of the film to change. As a result, blue-shifts were observed at the resonance band $LP_{0,20}$. Karposh *et al*. also fabricated a long period fiber grating refractive index sensor based on SiO_2 NPs with a slight modification. This time the PDDA was replaced with the PAH polymer [54]. The instruments, LPG characteristics and layers thickness were same as those reported in the literature [53]. The sensor was exposed to three different solutions (ethanol, glucose, and sucrose) of different concentrations. Different number of layers 5, 10, and 15 were deposited on the optical fiber to study the effect of film thickness variation on the optical spectrum. The results showed that the highest refractive index sensitivity was obtained when the number of layers was 10 nm. However, the ethanol, glucose, and sucrose solutions led to the equivalent wavelength shifts when the same solutions concentrations were used. Therefore, the sensor was found to be sensitive to the change in the refractive index and not to the chemical itself. Furthermore, in order to make the sensor stable and enhance its performance three bilayers of PDDA/PSS polymer were deposited on the surface of the $(PAH/SiO_2\ NPs)_{10}$ film. The results showed that the PDDA/PSS film deposition increased the stability of the sensor and its sensitivity to the external refractive index. This sensor can be utilized in medical applications and harsh environments.

Tian *et al.* fabricated a LPG sensor for refractive index detection and proved that the sensitivity of the sensor can be enhanced by modifying it with gold nanoparticles [55].

The gold nanoparticles were negatively charged and were deposited on the positive polymer PAH. To examine the ability of the sensor to detect changes in the refractive index, the sensor was exposed to water, alcohol and 40% glycerin. The sensitivity of the sensor was ~ 460 nm/RIU before the film deposition while it raised to 759 nm/RIU after the film deposition due to the alteration of the effective refractive indices of the core and the cladding.

Socorro *et al.* presented a tapered optical fiber sensor that can be used to detect PH ranging between 40% and 60% based on the generation of lossy mode resonances utilizing a polymeric thin film based on PAH/PDDA [56]. An optical fiber sensor based on lossy mode resonance supporting film was presented by Zamarreno *et al.* for relative humidity monitoring [57]. The film was formed by the deposition of titanium dioxide (TiO_2) and PSS alternatively on the core of the fiber. The sensitive region was exposed to relative humidity ranging between 20% and 90%. It was shown that changing the relative humidity leads to changes in the refractive index of the film and as a result shifting the resonance bands to the longer wavelength region.

Lopez-Torres *et al.* presented for the first time an interferometric optical photonic crystal fiber sensor based on the layer-by-layer technique for humidity measurement [58]. For the interferometer formation, a 1 cm length photonic crystal fiber was spliced between two single-mode fibers. The photonic crystal fiber was coated with multilayered PAH/PAA nanofilm. Two approaches were used for relative humidity characterization which were the wavelength shift and the fast Fourier transform. The sensor ability to detect relative humidity in the range of 20% to 95% was proved. Rivero *et al.* fabricated a relative humidity sensor based on PAH/PAA polymeric film that was loaded with silver

nanoparticles [59]. This type of sensors was presented for the first time based on two types of resonances which were the localized surface plasmon resonance and the lossy mode resonance. The sensor showed a sensitivity of 0.943/RH% to humidity changes.

The structure of long period fiber gratings was presented by Li *et al.* for the purpose of refractive index measurement [60]. Two different polyelectrolyte films were deposited on the structure for the aim of comparison which were PAH/PSS and PDDA/PSS. The effect of coating the films on the transmission spectrum of the long period fiber grating was carried out by exposing the sensor to different organic solvents. Moreover, the detected sensitivities for solvents in the case of the long period grating deposited with PDDA/PSS were higher than those obtained by the one deposited with PAH/PSS film because they have a higher swelling degree when they are immersed in the organic solvents. A long period fiber grating sensor for the measurement of the refractive index of sucrose was introduced by Li *et al.* [61]. The sensor was based on the PAH/PSS polymeric coating and the sensing mechanism was based on the detection of the shift in the wavelength resonance. The effect of the number of layers on the sensitivity of the sensor to the surrounding medium refractive index was examined theoretically and experimentally. The experimental results showed that different film thicknesses resulted in different wavelength shifts. For example, when the long period fiber grating was coated with 100 bilayers, it showed a wavelength shift higher than the one obtained by coating 115 bilayers.

1.6 Motivation

Since there is a demand in the biological and medical fields to detect proteins and antibody-antigen dynamic responses for easy, quick, and reliable diseases diagnosis [62], this thesis focuses on the fabrication of tapered fiber Mach-Zehnder interferometer coated with thin films for the purpose of biosensing and detection of streptavidin which is a homo-tetramer protein found to have a high bonding affinity for biotin. The approach that is used for achieving this goal is the dipping layer-by-layer technique. The film surface was functionalized with biotin (vitamin B) that has a strong binding constant with streptavidin [63].

Marques *et al.* fabricated a biosensor based on biotin/streptavidin interactions [62]. Long period gratings were fabricated using the point-by-point technique in a boron-germanium co-doped optical fiber. It was coated with three bilayers of PAH/SiO_2:Au NPs. The PAH was used as a cationic material while the nanoparticles with the silica core and gold nanoshells were utilized as an anionic material. Two diameters of SiO_2:Au NPs were synthesized to test the effect of the diameter of the nanoparticles on the performance of the sensor. The core diameters were 80 and 300 nm while those of the gold shells were between 2 and 5 nm. The sensor was exposed to biotin and then to streptavidin of different concentrations. The sensitivity of the sensor with 80 nm nanoparticles was 2.27 nm/(ng/mm^2) while the one of the 300 nm nanoparticles was 6.9 nm/(ng/mm^2). It was found that the sensor with 300 nm nanoparticles had a sensitivity higher three times than the one recorded by the sensor with 80 nm nanoparticles.

Another research was done by Wang *et al*. to fabricate a biosensor based on a special kind of long period grating which is the turnaround point long period grating [63]. A PAH/poly {1-[4-(3-carboxy-4-hydroxyphenylazo)-benzensulfonamido]-1, 2-ethanediyl, sodium salt} (PCBS) alternate layers were deposited on the turnaround point long period fiber grating to form a thin film on its surface using the ionic self-assembled multilayers technique. The number of bilayers that were deposited on the sensor was 1.5 (PAH/PCBS/PAH). Those layers were followed by the deposition of biotin. The fiber was then exposed to streptavidin for detection of specific bending. The sensor showed a high sensitivity toward low streptavidin concentrations. In a different approach Wang *et al*. also used the ionic self-assembled multilayers technique to deposit 20 bilayers of PAH/PCBS film on a long period fiber grating surface [64]. The purpose of the study was to investigate the film properties dependency on the change of PH levels of both PAH and PCBS. First, the experiments were done on a substrate with PH levels ranging from 6-9 for PAH solution and from 6-8 for PCBS solution. It was noticed that when the PH levels of the PAH were kept constant and those of the PCBS were increased, the total film thickness and refractive index declined. On the other hand, fixing the PH levels of the PCBS and increasing those of the PAH caused an increment in the total thickness of the deposited film and a decrease in its refractive index. The experiments then were repeated using LPG fiber with 5 cm length and 116 μm periodicity. The PH levels of PAH were in the range between 7.5 and 9 whereas those of the PCBS solution were in the range between 6 and 8. After every 5 bilayers deposition, the transmission spectrum was measured and the results showed that the increment of layers number resulted in resonance shifts.

Lin *et al*. fabricated a fiber tip biosensor based on localized surface plasmon resonance for streptavidin sensing in 2010 [65]. The fabrication technique was based on the deposition of gold nanodots on a single-mode fiber end using vacuum sputtering method followed by dipping the tip in an electron beam resist. After that, a two-dimensional nanoparticles array shape was formed on the resist material using the electron beam lithography method. The fiber tip was dipped into a developer and washed. Using the reactive-ion etching with argon ions the nanoparticles array shape was transferred to Au monolayer. A single layer of biotin was coated on the fiber tip by the functionalization of Au nanodots with biotinylated polyethylene glycol alkane thiol. The tip then was immersed in streptavidin solutions with concentrations varying from 10^{-13} to 10^{-6} M and the shift in the wavelength of the localized surface plasmon resonance was monitored after each immersion process. The sensor showed red-shifts after the biotin deposition as well as after the streptavidin binding. Also, with increasing the streptavidin concentration the localized surface plasmon resonance shift increased until it reached the saturation for concentrations that were higher than 10^{-8} M.

A year later, the same sensor was used for the detection of streptavidin but this time the sensing mechanism was based on monitoring the changes in the reflected spectra [66]. In this case, the sensor was exposed to 10^{-7} M of streptavidin and after the deposition of biotin, the wavelength shift obtained was 15 nm which was the same shift obtained for the streptavidin concentration when the transmission spectrum was monitored. Bare long period grating sensors have a low sensitivity to biochemical aqueous solutions which make them unfavorable devices.

Hence, Pilla *et al*. focused on presenting a fabrication method of a long period fiber grating biochemical sensor as a promising technology for label-free detection and that functions in the transition mode [67]. The fabrication of the sensor was based on the formation of a polystyrene overlay film using the dip coating approach that had a refractive index higher than that of the cladding. The polystyrene was used as a substrate for the immobilization of biotinylated bovine serum albumin on the long period grating. It is worth noting that bovine serum albumin interacts hydrophobically with polystyrene which makes it possible to adhere strongly with polystyrene. Next, the sensor was exposed to streptavidin. The dynamic of bovine serum albumin adsorption was studied as well as the dynamic of streptavidin binding.

The self-assembly monolayer technique was adopted by Cheng *et al*. for the fabrication of a chemical and biochemical optical fiber localized surface plasmon resonance sensor based on gold colloids [68]. This technique was applied on the core of a multi-mode fiber and by monitoring the changes in the attenuated total reflection, the sensitivity of the device was detected. The core was immersed into 3-(mercaptopropyl)-trimethoxysilane (MPTMS) solution and after washing into Au colloids so that a monolayer of Au colloids was formed on the surface of the core. 33% was the measured average coverage of surface. For chemical sensing, the device coated with an Au monolayer was exposed to sucrose of bulk refractive index in the range between 1.33 and 1.41. It was found that increasing the refractive index resulted in reducing the attenuated total reflection. For biochemical sensing, the Au monolayer was modified with cystamin and then functionalized with biotin for label-free detection of streptavidin. The response of the sensor towards streptavidin concentrations in the range between 0.5 and 3.0 nm was linear. The spectrum reached

saturation for a concentration larger than 30 nM. The sensor had a limit of detection of 9.8×10^{-11} M which was less by two orders than the one obtained using the mechanism of detecting the transmission spectrum.

The same approach for the fabrication of the Au self-assembly monolayer was used by Tang *et al*. on the core of a long period fiber grating [69]. The sensitivity of the device was tested for sucrose of bulk refractive index in the range between 1.33 and 1.39 by monitoring the changes in the transmission loss and wavelength peaks. The sensitivities of a bare long period fiber grating were 37.31 dB/RIU and -17.93 nm/RIU. After the Au monolayer was deposited on the long period grating, the sensitivities enhanced to become 59.3 dB/RIU and -23.45 dB/RIU. The model based on antibody-antigen was used as the binding mechanism for biochemical sensing. The Au colloids were modified by dinitrophenyl to detect anti-dinitrophenyl with concentrations ranging from 1×10^{-6} to 3×10^{-5} g/mol. It was shown that increasing the anti- dinitrophenyl concentrations led to a decrease in the transmission signal. However, the sensor had a limit of detection of 9.5×10^{-10} M.

Gu *et al.* constructed an interferometric optical fiber PH biochemical sensor by sandwiching a thin core fiber between two standard single-mode fibers using the layer-by-layer method [70]. The interferometer was coated with 23 bilayers of PAH/PAA for the formation of a nanostructured film. The sensor response to PH variations was examined using acid and alkali solutions showing sensitivities of 0.32 nm/PH unit for acid and 0.45 nm/PH unit for alkali solutions. Shao *et al.* built a PH fiber sensor using the tilted fiber Bragg grating structure which was coated with multilayers of PDDA/PAA [71]. It was

found that exposing the sensor to different PH solutions led the deposited film to swell. This effect changed with increasing the PH as a result of the ionization of the carboxyl groups. Also, the refractive index of the film reduced with increasing the PH causing a change in the transmission spectrum.

1.7 Outline of Thesis

This thesis is divided into four chapters which are organized in the following fashion:

Chapter 2 presents experimental results of the fabrication of fiber optics based on a single-taper by the fusion splicing technique and a study of the elements that impact the taper properties such as arc current, duration, and strain. Moreover, it involves the fabrication technique of symmetrical and asymmetrical tapered fiber MZI and a study of the effect of separation distance between tapers, waist size, propagation direction, and coating removal on the properties of the MZI such as the free spectral range and/or the extinction ratio of the transmission spectrum.

Chapter 3 reports a focused study on the symmetrical tapered fiber MZI as a biosensor for streptavidin detection which is performed to reveal the effect of the deposition of multiple layers of the films on the sensitivity of the fiber. Chapter 4 draws a conclusion of this study.

Chapter 2

Fabrication of Tapered Optical Fibers

Introduction

Tapering is the process of stretching and heating an optical fiber to reduce its radius so that its waist becomes smaller than otherwise un-tapered region [72, 73]. It is an efficient approach for coupling a large amount of light energy from the core mode to higher order cladding modes [72]. Tapers can be categorized into adiabatic and non-adiabatic depending on the tapering angle [72, 74-76]. If the tapering angle is small, most of the light energy propagating in the fiber will be directed to the core (the fundamental mode) without being coupled to higher order modes when it passes through the taper. In this case, the taper is

described as adiabatic [77]. In contrast, if the tapering angle is large, some of the power that propagates along the core will be coupled into the cladding. The taper in this situation is described as non-adiabatic [72]. In some occasions, adiabatic tapers are more favorable due to their ability to minimize the insertion loss in comparison with non-adiabatic tapers [78]. Furthermore, their working principle depends on detecting the shift in the power. However, the insertion loss of non-adiabatic tapers does not impact their sensing performance. In fact, they are preferred because their sensing principle relies on the interference between both the fundamental core mode and the cladding modes leading to a shift in the wavelength. The monitoring of this shift is more convenient than the one based on power attenuation [79]. The coating of the fiber causes the power that is coupled into the cladding to be attenuated for the non-adiabatic tapers. Without removing the coating, light propagates in the cladding for a few centimeters. Therefore, removing the coating will make the cladding a lossless medium [78].

Two types of tapered fiber sensors are preferred when it comes to talking about biosensing applications [72, 80]. The first kind is based on tapered tips that can be formed by reducing the fiber diameter gradually until a small tip at the end of the fiber is achieved. The tip serves as the sensing element of the sensor. The second type is fiber sensors based on continuous tapers, in which the tapered region is divided to three parts. The first region refers to the down-taper where the diameter of the fiber is reduced gradually. At the taper length region, the reduced diameter becomes constant and uniform. The diameter of the fiber then increases gradually in the third region (up-taper) [72, 80], as shown in Fig. 2-1. Various techniques were used for fabricating tapered fibers such as flame heating [81-84], CO_2 laser [85, 86] and fusion splicing [87-94]. Compared with other techniques, the fusion

splicing technique is repeatable, safe, convenient and controllable [95]. Hence, it is adopted in this chapter for the fabrication of single and double tapered optical fibers.

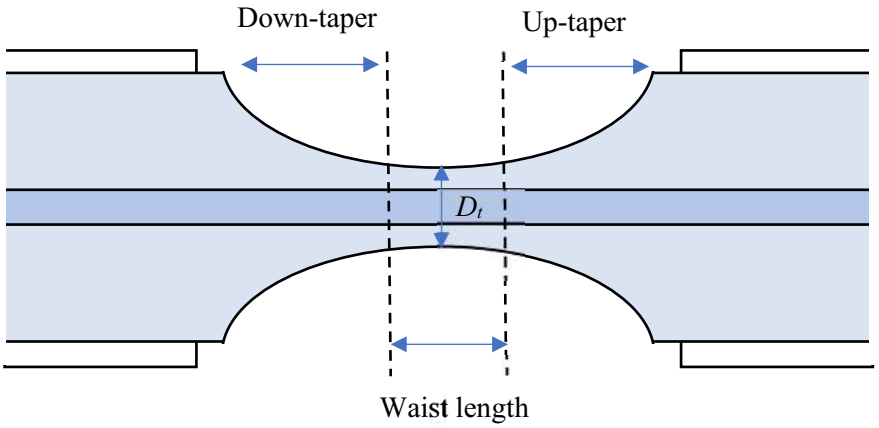

Figure 2-1 Schematic diagram of a single-mode tapered fiber.

When light propagates along an optical fiber, part of it will be coupled in the core while the other part will decline exponentially in the cladding based on the waveguide theory. In the case of an un-tapered optical fiber where the diameter is uniform, it is impossible for the evanescent field to interact with the external medium that surrounds the optical fiber [96]. This is because of the small penetration depth of the evanescent field in comparison with the cladding thickness [97]. The penetration depth can be defined by [98]:

$$d_p = \frac{\lambda}{2\pi\sqrt{n_{\text{core}}^2\, sin^2\theta_{\text{inc}} - n_{\text{clad}}^2}} \tag{2-1}$$

where λ is the wavelength of the light source, n_{core} is the refractive index of the core, n_{clad} is the refractive index of the cladding, and θ_{inc} is the angle of incidence at the normal of the core/cladding interface.

But the evanescent field interaction with the external environment is required for sensing applications and to overcome this problem reducing the diameter of the fiber by tapering is a feasible way to make this interaction possible [85]. When it comes to non-adiabatic tapers, light propagates in the core mode LP_{01}^{core} of a SMF will be excited to higher cladding modes LP_{0m}^{clad} by the down-taper area. The two modes will be coupled back by the upper-taper area to the core resulting in an interferometric pattern in the transmission signal [85]. The output intensity of the light passing through a tapered fiber is [99]:

$$I_{\text{out}} = I_{\text{core}} + I_{\text{clad}} + 2\sqrt{I_{\text{core}} I_{\text{clad}}} \cos(\Delta\phi) \tag{2-2}$$

where I_{core} and I_{clad} are the intensities of the light propagating in the core and the cladding and $\Delta\phi$ is the phase difference between LP_{01}^{core} and LP_{0m}^{clad}. The phase difference is defined by [99]:

$$\Delta\phi = \frac{2\pi\, \Delta n_{\text{eff}} L}{\lambda} \tag{2-3}$$

and:

$$\Delta n_{\text{eff}} = n_{\text{eff,core}} - n_{\text{eff,clad}} \tag{2-4}$$

where Δn_{eff} is the difference between the effective refractive indices of the core and the cladding and L is the length of the taper.

The principle of non-adiabatic tapered fiber is the same principle applied in the MZI [99]. However, in adiabatic tapers 99.5% of the light propagates in the core and the rest of it that penetrates in the cladding is negligible [85].

When two tapers are fabricated with a distance in between, a MZI is formed. The first taper functions as a beam splitter that excites the light from the core to higher cladding

modes. On the other hand, the second taper functions as a combiner of the beams. In the case of a MZI, L in equation (2-3) represents the length between the two tapers. Also, the peak wavelength can be defined as [25]:

$$\lambda_m = \frac{2\Delta n_{\text{eff}} L}{2m+1} \tag{2-5}$$

and the difference between neighboring peak wavelengths is [25]:

$$\Delta\lambda_m = \lambda_{m-1} - \lambda_m = \frac{4\Delta n_{\text{eff}} L}{(2m-1)(2m+1)} \tag{2-6}$$

It is worth noting that if the external refractive index surrounding the tapered fiber MZI increases, a change in the phase shift and hence an increase in the effective refractive index of the cladding by a magnitude of δn_{eff} will result. The effective refractive index of the core will remain unchanged. This causes the difference between the effective refractive indices of the core and the cladding to decline by δn_{eff}. Therefore, the peak wavelength of the interference will experience a blue-shift by $\delta\lambda_m$ so that [25]:

$$\delta\lambda_m = \frac{2(\Delta n_{\text{eff,core}} - \delta n_{\text{eff,clad}})L}{2m+1} = -\frac{2\delta n_{\text{eff,clad}} L}{2m+1} \tag{2-7}$$

2.1 Single-Tapered Optical Fibers

The fusion splicing technique is used to reduce the diameter of the fiber and form a single taper in this study. The fusion splicer used in the experiments is FITEL S182A. It consists of two movable stages ZL and ZR with V-grooves where the fiber can be positioned and two electrodes that generate an electric current which is used to melt the fiber, as shown in Fig. 2-2(a). First, a standard telecommunication SMF of a 0.5 m length is prepared for the tapering process. The coating of a 5.0 cm segment in the middle is removed using a stripping tool and the area is cleaned by alcohol. Figure 2-2(b) shows the SMF before the coating is removed. Second, the two stages of the fusion splicer are moved forward and aligned in order to achieve a uniform taper. The fiber is then placed in the V-grooves, stretched for a certain distance and heated by applying an arc current. After these steps, a tapered fiber with reduced waist D and total taper length L_t can be obtained (Fig. 2-2(c)).

By changing the fusion splicer settings such as the arc current, arc duration and the stages forward and backward movement, one can obtain tapers with different diameters and lengths. The effect of each of these factors on the taper properties will be studied in the following section.

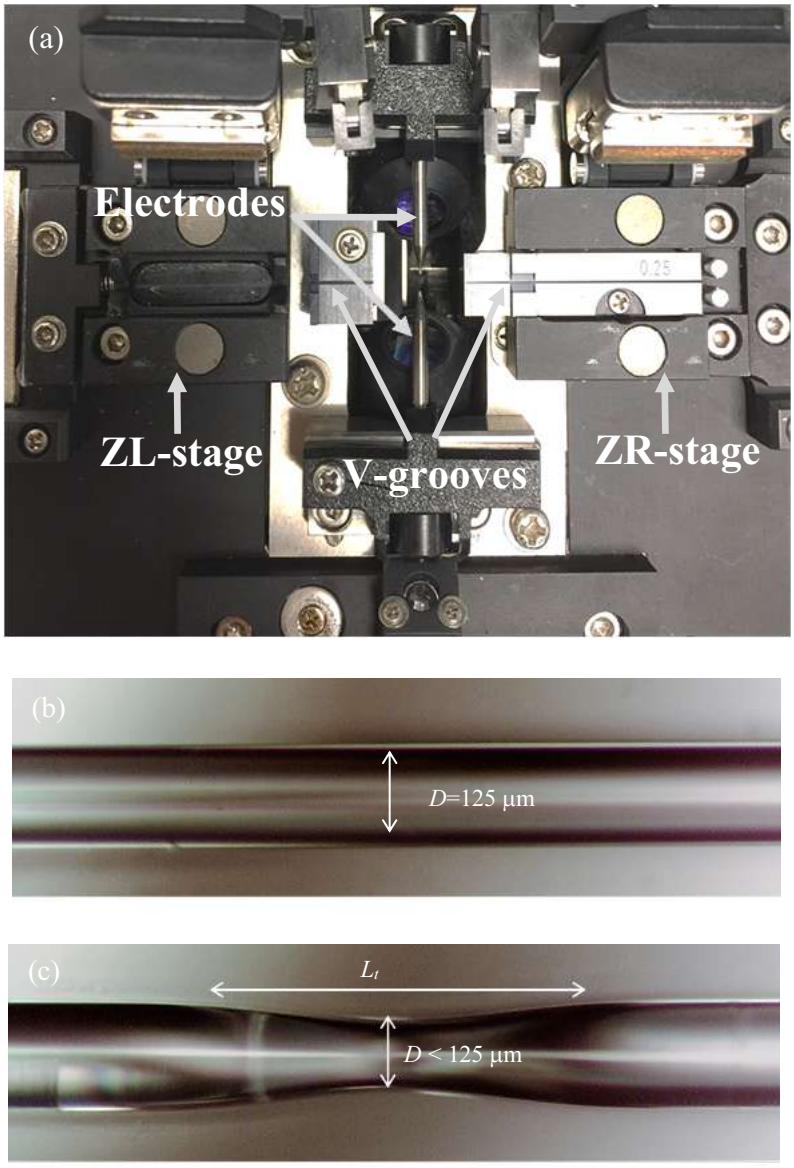

Figure 2-2 Fabrication of a tapered fiber with a fusion splicer: (a) components of the fusion splicer; (b) a standard SMF before tapering with a waist D of 125 μm; and (c) a tapered fiber with a waist diameter less than 125 μm and a taper length of L_t fabricated by the fusion splicer.

2.2 Influence of Fusion Splicer Settings on the Characteristics of Tapers

2.2.1 Effect of Arc Current

To study the arc current effect of the fusion splicer on the taper specifications it must be adjusted while all other conditions such as arc duration and the stages movement remain unchanged. The arc duration is set at 750.0 ms. The ZL and ZR stages are moved forward by 500.0 μm. The fiber is placed in the V-grooves and stretched when the stages are moved backward by 65.0 μm. An arc current is applied to form the taper.

Three fiber samples have been prepared for three different arc currents. The first applied current is 14.365 mA. After the taper is formed, the tapered region is fixed on a glass substrate so that the specifications of the taper can be measured under an optical microscope. The arc current results in a reduction of the diameter of the fiber by 33.3 μm when the waist diameter decreases from 125.0 to 91.7 μm. The measured length of the taper is 344.4 μm (Fig. 2-3(a)). When the arc current is increased to 15.541 mA, a thinner waist and a longer length of the tapered region are obtained which are 82.6 and 376.4 μm, respectively (Fig. 2-3(b)). The third sample is exposed to an arc current of 16.718 mA for which the diameter of the fiber is reduced by 46.5 μm to give a taper of a waist diameter of 78.5 μm. When decreasing the waist diameter of the fiber, the length of the taper increases to 395.1 μm, as shown in Fig. 2-3(c).

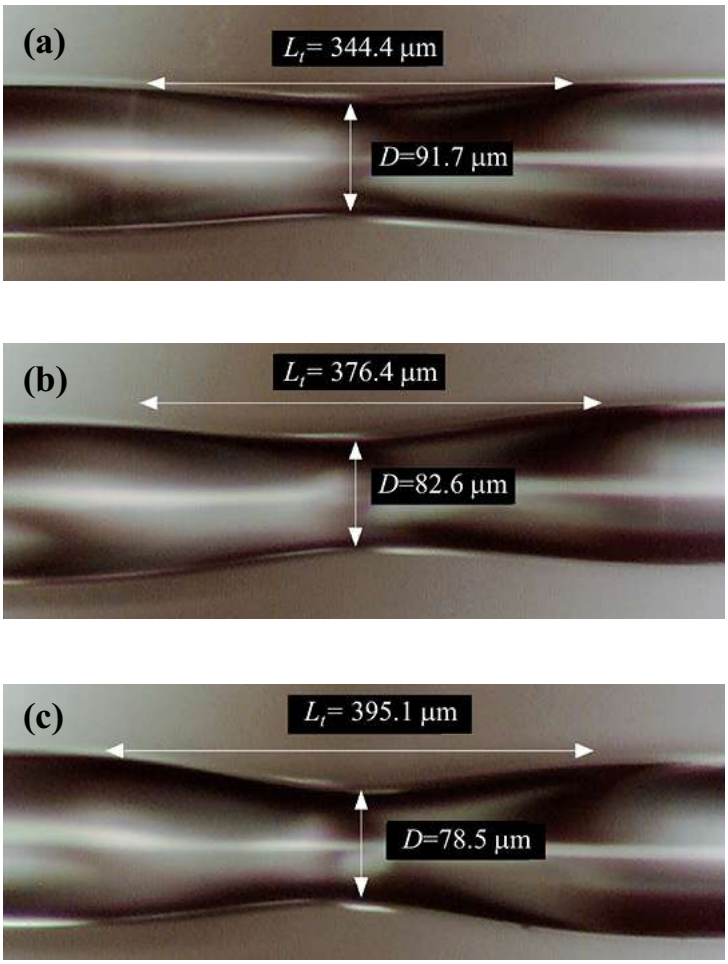

Figure 2-3 Microscopic images of three samples of SMFs tapered by using different arc currents which are: (a) 14.365; (b) 15.541; and (c) 16.718 mA.

Figure 2-4 shows the effect of the arc current variations on the taper waist and length. It can be concluded that increasing the arc current leads to a decrease in the taper waist. Moreover, as the taper waist decreases, its length increases.

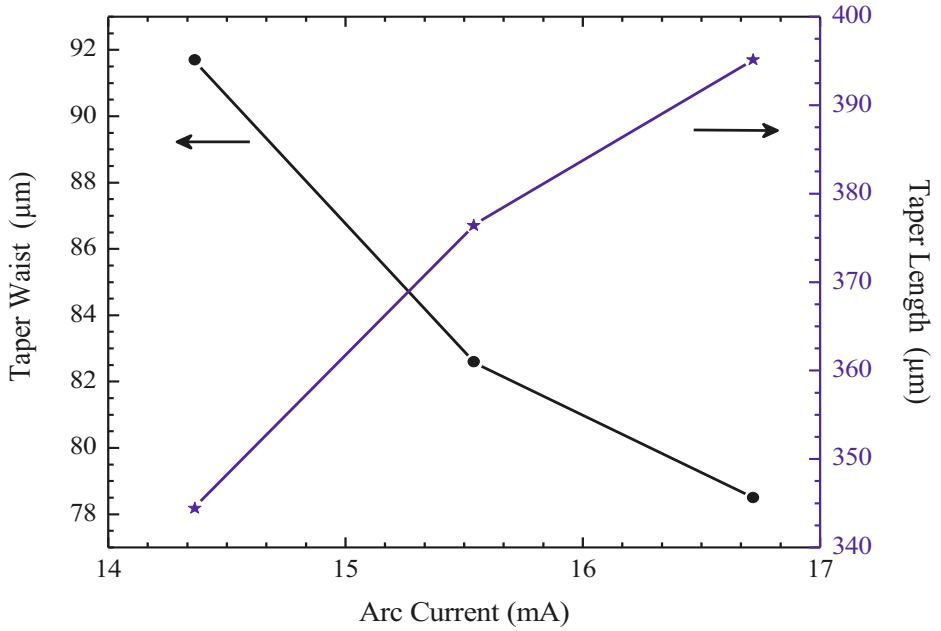

Figure 2-4 Effect of arc current variations on the taper waist and length.

2.2.2 Effect of Arc Duration

The aim of this experiment is to study the effect caused by the variations of arc duration on the taper specifications. The arc current is fixed at 15.706 mA and the ZL and ZR stages are moved forward by 500.0 μm. The fiber was stretched when the stages are moved backward by 65.0 μm.

Two short duration sets are applied on different SMFs which are 350.0 and 450.0 ms. When the duration is set at 350.0 ms, the resultant taper has a waist diameter of 86.8 μm and a length of 382.7 μm (Fig. 2-5(a)). The microscopic image in Fig. 2-5(b) is the fiber taper fabricated with duration of 450.0 ms. A decrement in the waist of 80.6 μm is realized. However, the length L_t is found to be 388.9 μm. It can be noticed that the waist

diameter of the taper decreases when the duration increases from 350.0 to 450.0 ms. Moreover, an increment in the length of the taper is observed with the reduction of the waist diameter.

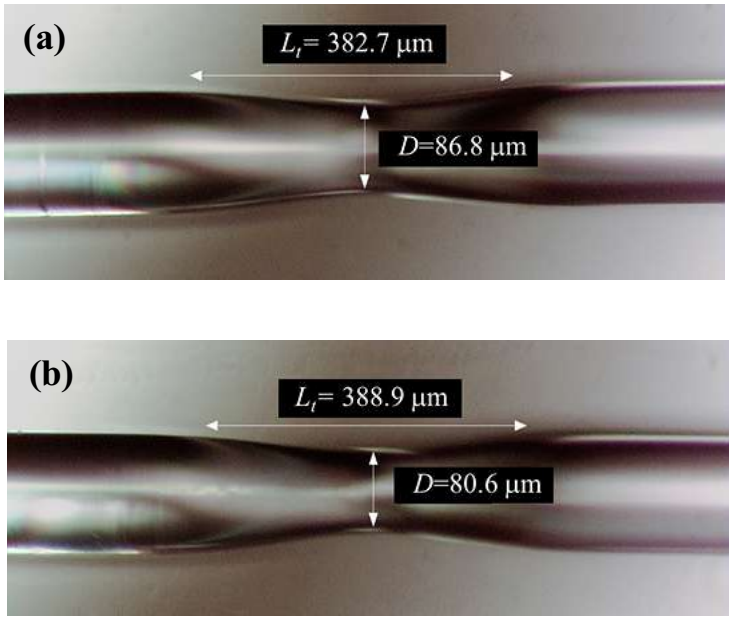

Figure 2-5 Microscopic images of two samples of SMFs tapered by changing the arc duration of the fusion splicer. Two small durations: (a) 350.0 and (b) 450.0 ms are used.

To examine the effect on tapering optical fibers with longer durations, three different sets of 2050.0, 3050.0 and 4050.0 ms are selected. The first sample is tapered when the duration is set at 2050.0 ms. As can be seen in Fig. 2-6(a), the resultant taper has specifications of D = 79.9 μm and L_t = 422.9 μm. The duration at 3050.0 ms causes the waist diameter to shrink to 78.5 μm. The length of the taper is found to be 426.1 μm (Fig. 2-6(b)). However, the longest duration (4050.0 ms) results in a taper of a waist diameter and length of 75.7 and 440.3 μm, respectively (Fig. 2-6(c)).

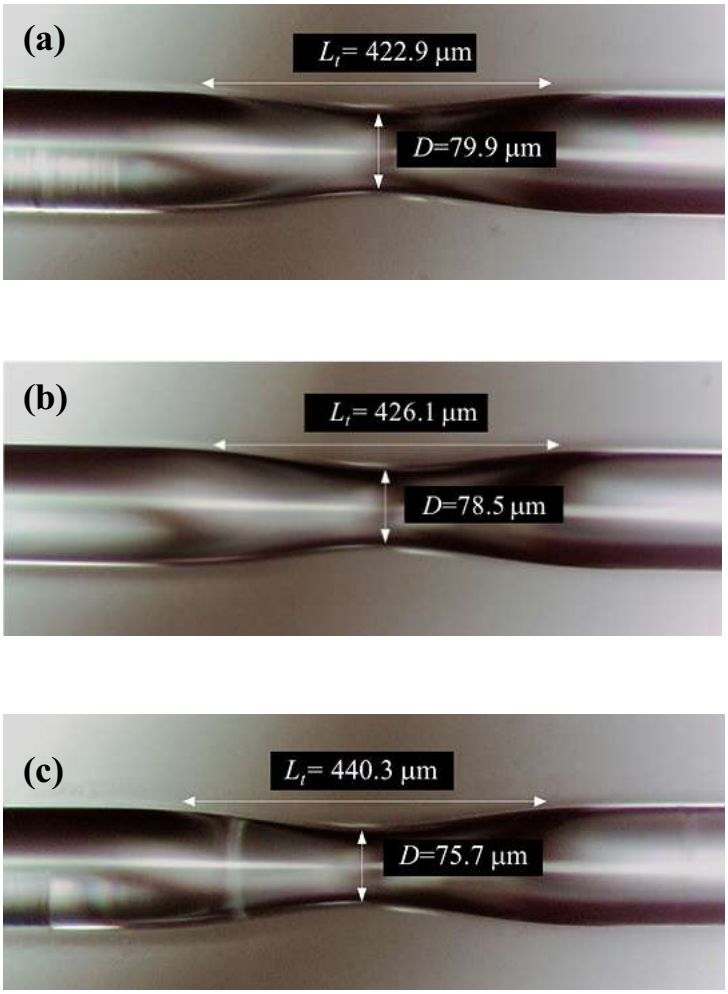

Figure 2-6 Microscopic images of different SMF tapers made by changing the arc duration of the fusion splicer. Three long durations: (a) 2050.0; (b) 3050.0; and (c) 4050.0 ms are adopted to study the effect on the waist diameter and length of the tapers.

Figure 2-7 shows the effect of various long arc durations on the waist diameter and length of tapers. It can be noticed that the longer the arc duration on the fiber, the thinner and longer the tapers are.

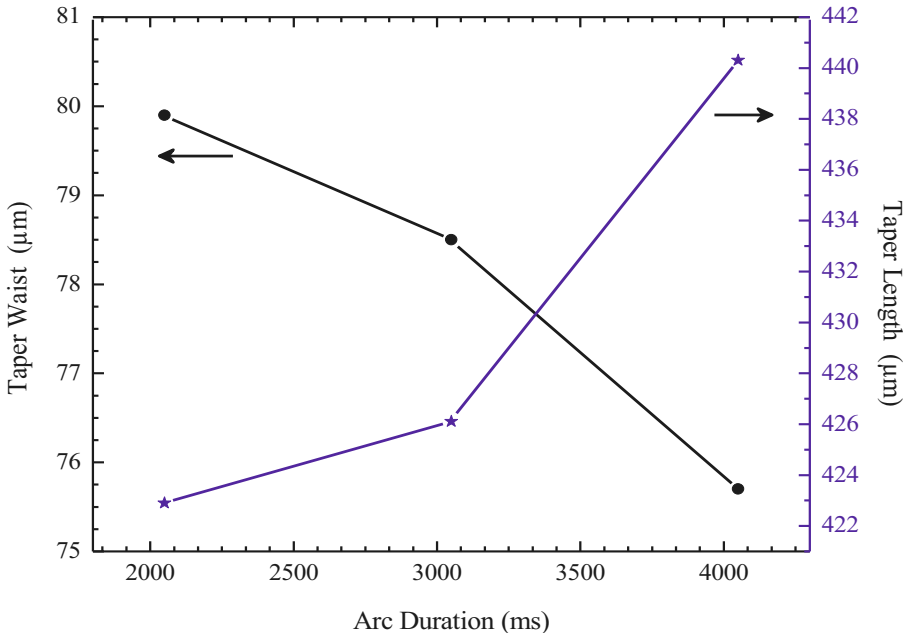

Figure 2-7 Effect of long arc duration variation on the waist and length of tapers.

2.2.3 Effect of Applied Strain

To study the effects of applied strain on the specifications of tapers، both arc current and duration of the fusion splicer are kept constant. However, their backward movement is changed so that different stretching forces are applied on the fiber. When the stages are moved inversely by 75.0 μm and an electric current is applied, the SMF waist decreases noticeably by 63.3 μm so that D and L_t are 61.7 and 505.8 μm, respectively (Fig. 2-8(a)). The two stages then are reset and moved forward by 500.0 μm in order to prepare the

second sample. To ensure constant forward motions of the stages in all fabricated tapered fibers, this step is conducted before every new tapering process. After the fiber is placed in the V-grooves of the stages, a strain is applied by moving the stages backward by 85.0 μm. The increment of the applied strain creates further reduction of the radius of the fiber. The waist diameter of this sample after tapering becomes 52.9 μm while the taper length is 522.0 μm (Fig. 2-8(b)). The third fiber sample is stretched when the stages are moved backward by 95.0 μm. The applied strain leads to a taper of a waist and length of 43.2 and 553.5 μm, respectively (Fig. 2-8(c)). Finally, a single-mode fiber is exposed to a higher strain when the stages are moved backward by 105.0 μm. Because of increasing the strain on the uncoated region, a taper of a very thin waist and long length is formed when applying the electric current. The waist diameter of the obtained taper is 23.4 μm while its length is 562.5 μm (Fig. 2-8(d)). It can be concluded from the obtained results that applying strain on the taper has a very noticeable impact on reducing the size of the fiber radius (~ 10 μm). This effect is much significant than the one caused by changing the arc current or the arc duration. Moreover, as the applied strain increases, the waist diameter of the taper reduces resulting in the observation of thinner tapers. The length of the tapered region becomes longer with the shrinkage of the waist. However, if the applied strain is very high, the fiber may break when an arc current is applied.

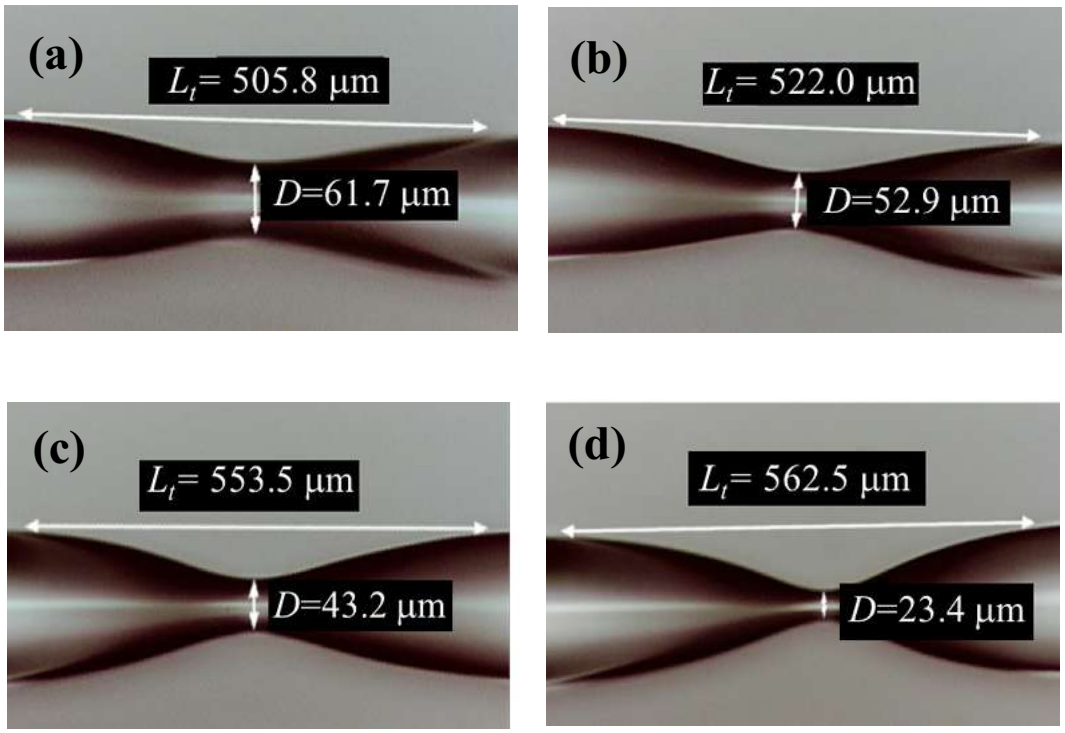

Figure 2-8 Optical microscopic images of different tapered SMFs formed by applying different strain powers before fusion splicing. Different tapers waists and lengths are observed by moving the stages of the fusion splicer inversely by: (a) 75.0; (b) 85.0; (c) 95.0; and (d) 105.0 μm.

Figure 2-9 illustrates the effect of the applied strain on the waist diameter and length of the tapers. When the pulling distance is changed between 75.0 and 105.0 μm, the taper waist decreases gradually while the length of the taper keeps increase.

The measurements of tapers' waists and lengths are repeatable when using the same fabrication parameters of the arc current, arc duration, and applied strain, which were summarized in Table 2-1.

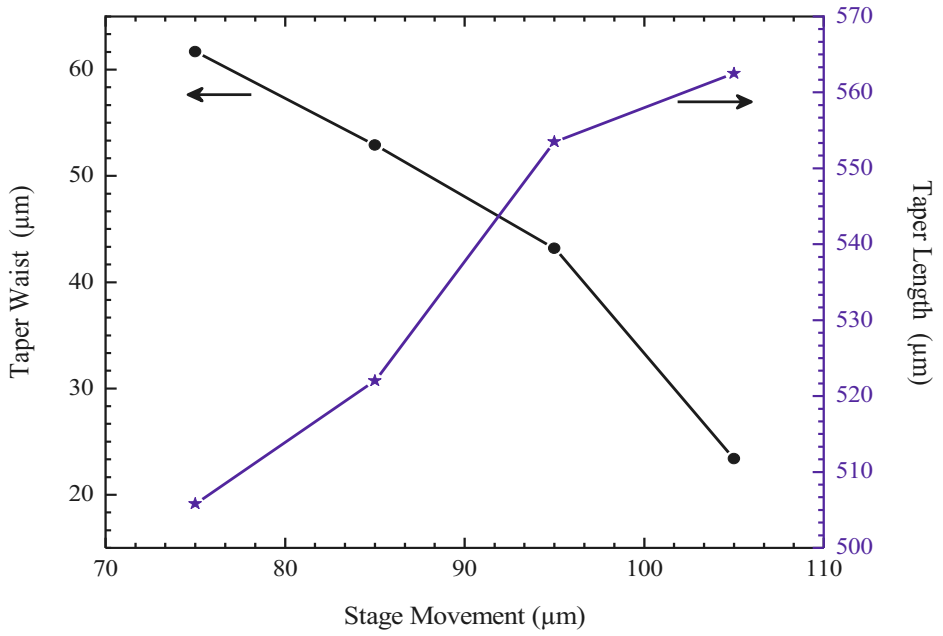

Figure 2-9 Effect of applied strain on the taper waist and length.

Table 2-1 Summary of the characteristics of the tapers obtained by changing the settings of the fusion splicer.

Parameter		Value	Taper Waist (µm)	Taper Length (µm)
Arc Current (mA)		14.365	91.7	344.4
		15.541	82.6	376.4
		16.718	78.5	395.1
Arc Duration (ms)	Low	350.0	86.8	382.7
		450.0	80.6	388.9
	High	2050.0	79.9	422.9
		3050.0	78.5	426.1
		4050.0	75.7	440.3
Applied Strain		$1.5x10^{-03}$	61.7	505.8
		$1.7x10^{-03}$	52.9	522.0
		$1.9x10^{-03}$	43.2	553.5
		$2.1x10^{-03}$	23.4	562.5

2.3 Fabrication of Tapered Fiber Mach-Zehnder Interferometer

The formation of an optical fiber Mach-Zehnder interferometer (MZI) depends on the fabrication of two elements that function to excite the light propagating in the fundamental mode to the cladding modes in the optical fiber. It is classified as symmetric or asymmetric based on the type of its excitation elements. In the case of symmetrical fiber MZI, identical excitation elements are utilized such as a pair of tapers [25-28] or a pair of LPGs [100, 101]. While, the coupling components in the asymmetrical fiber MZI are not identical. For example, using a taper and a core-offset for splitting and combining the light to and from the cladding modes [31].

2.3.1 Symmetrical Tapered Fiber Mach-Zehnder Interferometer

A SMF with a length of 1.0 m is prepared for the fabrication of two symmetrical tapers using the fusion splicing technique. First, the coating of the fiber over a segment of 1.0 cm is removed in the middle section and cleaned. The fiber is then placed straightly in the V-grooves, stretched and heated to get a taper with a waist diameter and length ~ 70.1 and 445.8 μm. A second taper with almost the same features is fabricated a few centimetres away from the first one using the same arc current, duration and stages forward and backward movement. The transmission spectrum of a light wave emitted from an Er^{3+} Dual-Band Broadband Source is detected when travelling through an un-tapered fiber using Ando AQ-6315E optical spectrum analyzer. Next, the spectrum of a SMF with a single-taper written on it is detected. A comparison between the transmission spectra of the fiber before and after writing a single-taper on the fiber indicates that the transmission loss

increases due to leaking of the light propagating in the core mode to the cladding (Fig. 2-10). A further change in the signal power is also observed after fabricating a second taper a few centimetres away from the first one. The interference pattern of the Mach-Zehnder interferometer structure is influenced by some parameters such as the waist diameter, the length of the tapers and the separation distance L_s between them. The waist diameter of the tapers significantly influences the extinction ratio. The extinction ratio can be determined by the ratio between two intensity levels. It is defined as the ratio of the maximum and minimum optical output intensity [103]. On the other hand, the periodicity or the free spectral range is determined by the wavelength difference between two maximum or minimum intensities. In fact, L_s also affects the extinction ratio slightly [102]. These two factors as well as the effect of the propagation direction are examined experimentally in the following sections.

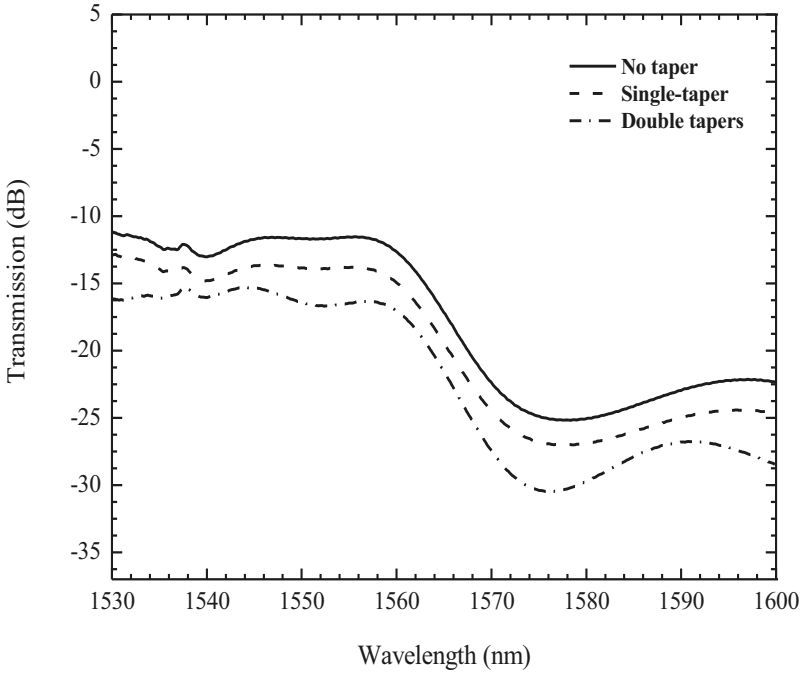

Figure 2-10 Transmission spectra of light when it passes through a pristine fiber, a single-tapered fiber and a tapered fiber MZI.

2.3.1.1 Effect of Separation Distance Between Tapers

In order to study the effect of the length (L_s) between the two tapers on the interference pattern, three fiber samples have been prepared with different separation distances between the tapers. The separation distance between the tapers of the first Mach-Zehnder interferometer is 2.0 cm. The waist diameters of the tapers (T1) and (T2) are 69.4 and 68.1 μm, respectively. In addition, the lengths of the tapers are 443.8 and 444.5 μm for (T1) and (T2), respectively. The separation distance between the tapers of the second Mach-Zehnder interferometer is 3.0 cm. The tapers (T1) and (T2) have waist diameters and lengths of $D1$ = 70.1, $D2$ = 68.8, $L1$ = 443.2 and $L2$ = 445.8 μm. The third fiber MZI is fabricated with a separation distance of 4.0 cm between the tapers. The waist diameters of the tapers of this sample are 71.9 and 70.8 μm. However, the lengths of the tapers are 445.8 and 446.9 μm, respectively.

Table 2-2 Characteristics of the three samples of the symmetrical tapered FMZI.

L_s (cm)	$D1$ (μm)	$D2$ (μm)	$L1$ (μm)	$L2$ (μm)
2.0	69.4	68.1	443.8	444.5
3.0	70.1	68.8	443.2	445.8
4.0	71.9	70.8	445.8	446.9

After the fabrication of the tapers, each sample is straightened and fixed on a glass substrate. The coating is stripped off from the ends of the fibers. They are cleaned, cleaved, and connected to the light source and the OSA. Figure 2-11 shows a schematic illustration of the experimental setup. Initially, the coating between the tapers is kept for the purpose

of comparison and the transmission spectrum is recorded in a wavelength ranging from 1530 to 1620 nm. Later, it is stripped off and the spectrum is recorded again.

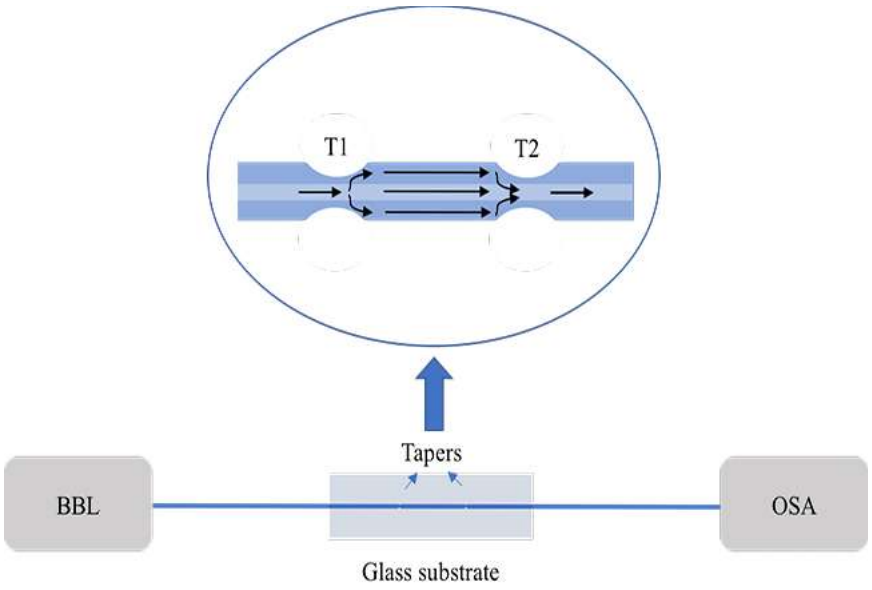

Figure 2-11 Schematic illustration of the experimental setup. BBL is a broadband light source.

As it is mentioned earlier, the coating surrounding the cladding has a higher refractive index in comparison with the refractive index of the cladding. As a result, the light propagating in the cladding mode will be strongly absorbed by the coating [69]. Hence, the extinction ratios of the first, second, and third fiber MZIs when the coating is kept between the tapers are smaller than those obtained after the coating is removed, as shown in Fig. 2-12. The extinction ratio before the removal of the coating is 5.03 dB for the 2.0 cm length MZI where the peak and valley intensities are -8.72 and -13.75 dB, respectively, in the wavelength range between 1587 and 1602 nm. The MZI with a separation distance of 3.0 cm has intensities of the peak and the valley before coating

removal with values of -20.14 and -27.58 dB, respectively. The resultant extinction ratio for those intensities locating in the wavelength range between 1589 and 1598.2 nm is 7.44 dB. The peak and valley intensities obtained by the MZI of 4.0 cm length are -16.78 and -27.15 dB, respectively, in the wavelength range between 1595 and 1601.2 nm. As a result, the extinction ratio for this sample is 10.37 dB. While, the calculated extinction ratios after the coating is removed are 5.89, 11.17, and 13.05 dB for each one of the 2.0, 3.0, and 4.0 cm MZIs, respectively. The peaks intensities for the three samples in this case are -8.47, -18.94 and -16.61 dB, respectively. Moreover, the valleys intensities are -14.36, -30.11 and -29.66 dB, respectively.

The relationship between the separation distance between the two tapers and the extinction ratio before and after the removal of the coating between the tapers is shown in Fig. 2-13. Therefore, we can conclude that the removal of coating decreases the loss and hence the extinction ratio of the transmitted signal increases. Nevertheless, the extinction ratio increases with increasing the separation distance between the symmetrical tapers of the MZI.

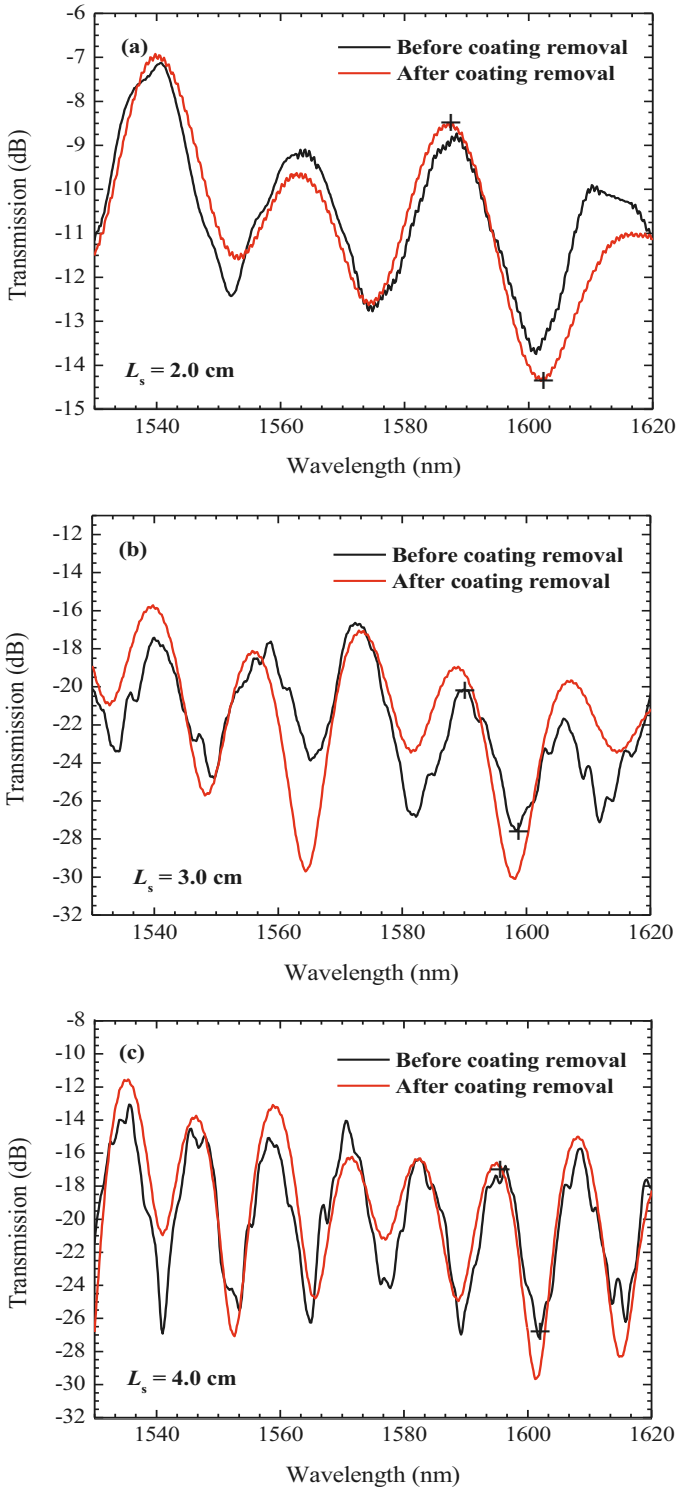

Figure 2-12 Transmission spectra of a symmetrical tapered fiber MZI with a separation distance between the tapers of: (a) 2.0; (b) 3.0; and (c) 4.0 cm before and after removing the coating between the tapers.

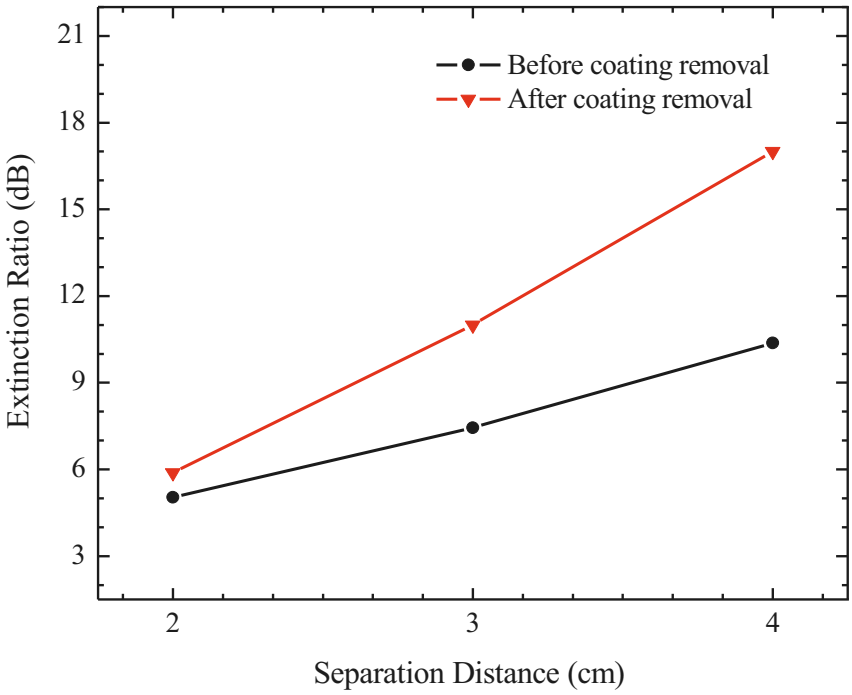

Figure 2-13 Dependence of the extinction ratio on the separation distance between the tapers before and after the removal of the coating between the tapers.

It can be noted that the free spectral range (FSR) of the fringes changes with the alternation of the spacing between the tapers. The effect of increasing the separation distance between the tapers on the FSR is examined through the detection of the output signal of the three samples of the MZIs which have separation distances of 2.0, 3.0, and 4.0 cm, respectively (Fig. 2-14). Curve (a) represents the transmission spectrum of the first sample where the calculated FSR is 28.0 nm. Curve (b) is the interference pattern obtained from coupling the light through the second MZI. The FSR for this sample reduces to 16.5 nm which is less than the corresponding value for the sample 1 by 11.5 nm. The MZI with 4.0 cm separation distance, which is represented by curve (c), shows a periodicity of 12.0 nm between the peaks. Thus, we can conclude that the longer the distance between the

tapers the smaller is the free spectral range, which is evident in Fig. 2-15 The results show a good agreement with the equation [102]:

$$\mathrm{FSR} = \frac{\lambda^2}{L_s \, \Delta n_{\mathrm{eff}}} \tag{2-8}$$

where λ is the wavelength, L_s is the length of the interferometer, and Δn_{eff} is the effective refractive index difference of the core and the cladding.

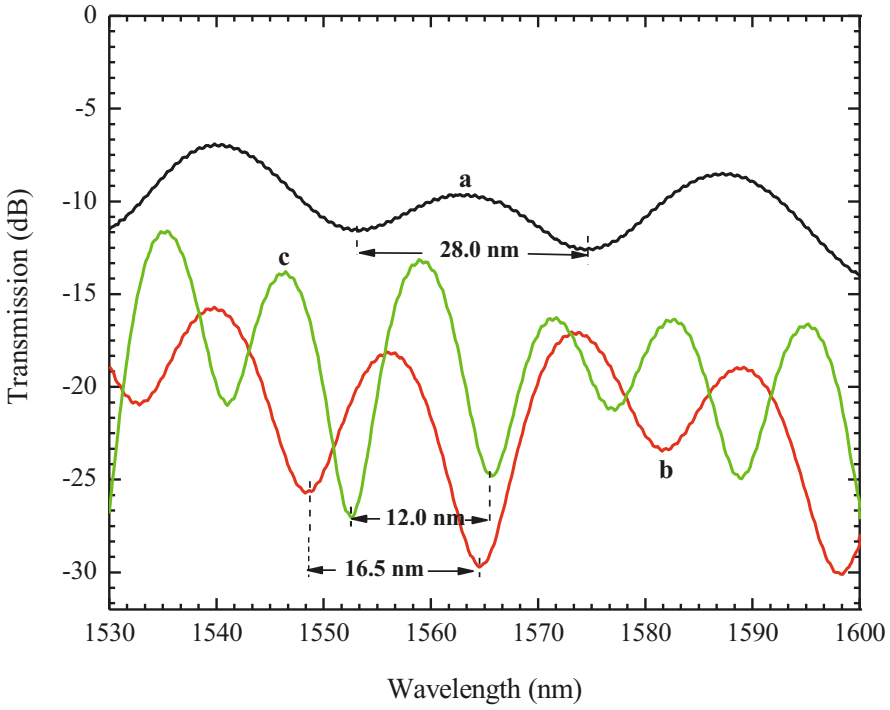

Figure 2-14 Free spectral range of symmetrical tapered FMZIs with separation distances between the tapers of: (a) 2.0; (b) 3.0; and (c) 4.0 cm.

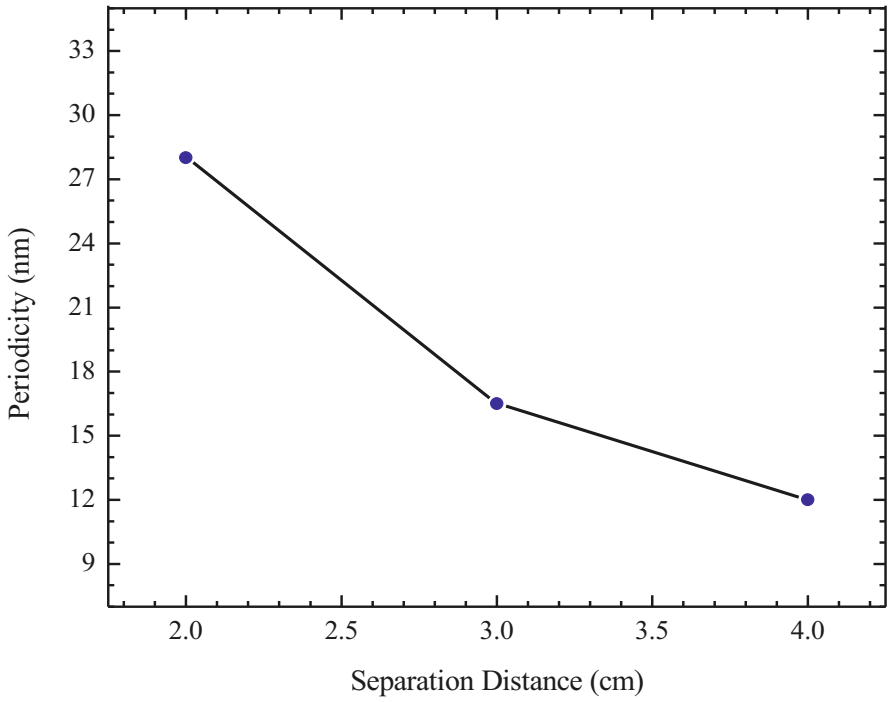

Figure 2-15 Dependence of the periodicity of the interferometric pattern on the separation distance between the tapers of symmetrical MZI.

2.3.1.2 Effect of Propagation Direction

The same samples with the characteristics shown in Table 2-2 are used to study the influence of the propagation direction on the interference pattern. However, in this experiment the ends of the fibers are switched so that the light is excited to cladding modes through the second taper (T2) and then recombined with the fundamental mode through the first taper (T1) to generate an interference. The propagation of the light through (T2) to (T1) will be referred to as reversed propagation in this section. A schematic diagram of the experimental setup is shown in Fig. 2-16.

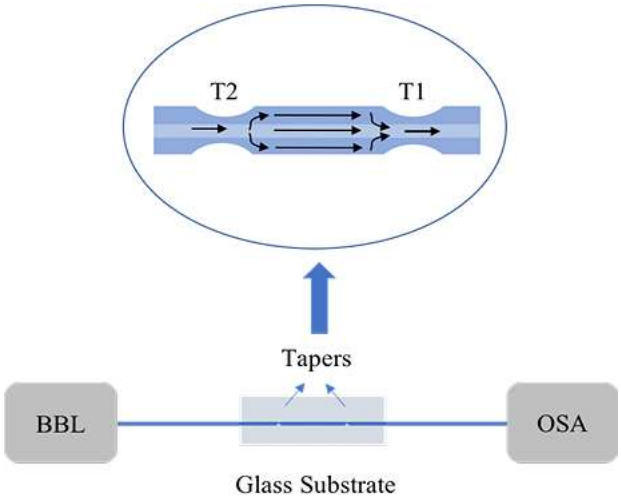

Figure 2-16 Schematic illustration of the experimental setup where light propagates through (T2) first and coupled by (T1).

A comparison between the forward propagation and the reversed propagation obtained by passing the light through the three samples indicates that the transmission spectra are slightly dependent on the direction of propagation (Fig. 2-17). As it is mentioned earlier in Section 2.3.1.1, the extinction ratios of the three MZIs in the case of the forward propagation are 5.89, 11.17, and 13.05 dB for the 2.0, 3.0, and 4.0 cm MZIs, which are calculated from the intensities of the peaks and valleys in the wavelength range between ~1587 and 1602 nm. However, in the case of the reversed propagation, the extinction ratios obtained from the intensities of the peaks and valleys in the same wavelength range are found to be 6.10, 9.88, and 8.62 dB for the 2.0, 3.0, and 4.0 cm MZIs, respectively. The dependence of the extinction ratios of the MZIs on the propagation direction can be linked to the small differences in the specifications of the two tapers of the MZI even though the tapers are fabricated under the same conditions. As a result, (T1) may excite certain cladding modes which are different from those excited by (T2) or they can distrubute the light power among the cladding modes differently.

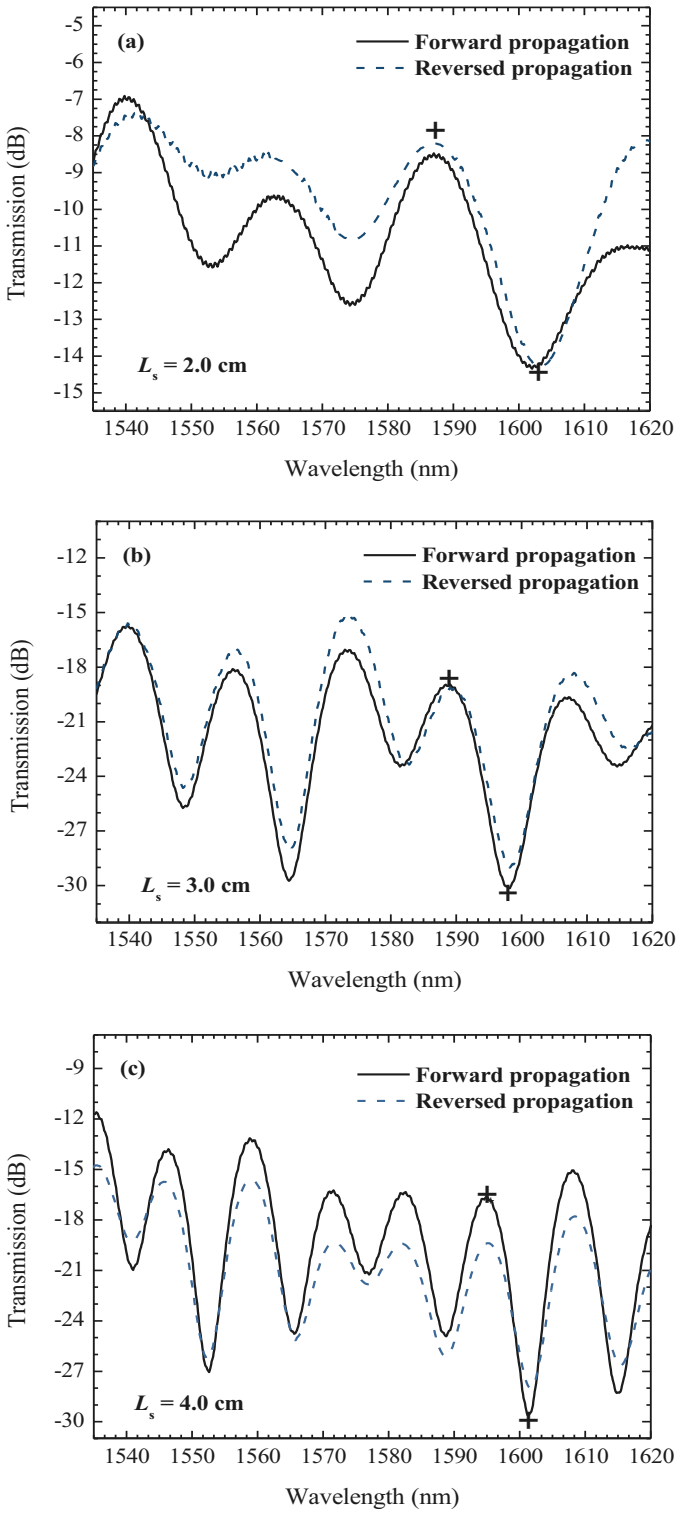

Figure 2-17 Transmission spectra of symmetrical TFMZIs when light propagates from (T1) to (T2) as well as it reverses propagation.

2.3.1.3 Effect of the Waist Size of Tapers

Another factor that influences the response of a tapered optical fiber is the waist diameter. By varying the diameter, different interferometric patterns can be observed due to the excitation of different cladding modes. In this section, three symmetrical tapered FMZIs have been fabricated. The forward and backward motions of the fusion splicer stages are fixed at 500.0 and 80.0 μm, respectively. The arc current and arc duration are fixed at 15.66 mA and 250.0 ms. The separation distance between the tapers is 3.0 cm.

For the fabrication of the first symmetrical tapered MZI, an arc current is applied through the electrodes to form a taper of a waist diameter and a length of 66.0 and 378.0 μm, respectively. Away from the first taper by 3.0 cm another taper with similar specifications is fabricated. The transmission spectrum of the sample is recorded and is denoted in Fig. 2-18 by Symmetrical MZI (1). In order to make thinner tapers, the arc current is applied more than once. By doing this, we can obtain tapers with thinner waist diameters but with almost the same taper lengths. For example, the arc current is applied three times for the fabrication of the second tapered MZI which results in tapers of a waist diameter ~ 62.5 μm. The transmission spectrum of the sample is presented in Fig. 2-18 and denoted by Symmetrical MZI (2). Furthermore, the last sample is fabricated with tapers of a waist diameter ~ 58.0 μm when the electrical current is applied five times. The curve denoted by Symmetrical MZI (3) in Fig. 2-18 shows the transmission spectrum for the sample.

The results show that MZI (1) has the smallest extinction ratio while the MZI (3) shows the largest extinction ratio. The symmetrical MZI (1) has an extinction ratio of 2.11

dB in the wavelength range between 1586 and 1598 nm. The intensities of the peak and the valley in this wavelength range are -3.32 and -5.43 dB, respectively. A larger extinction ratio of 3.17 dB is obtained by MZI (2) where the intensity of the peak is -4.10 dB and the intensity of the valley is -7.27 dB in the wavelength range between 1599.5 and 1608.3 nm. The intensities of MZI (3) are -1.03 dB for the peak and -5.04 dB for the valley which locate in the wavelength range between 1592.1 and 1602.5 nm. The resultant extinction ratio in this case is 4.01 dB which is the largest among those obtained by MZI (1) and MZI (2). Figure 2-19 illustrates the relationship between the waist diameter of the symmetrical tapered MZI and the extinction ratio. It can be concluded that the reduction of the waist diameter of the taper causes the extinction ratio of the signal to increase because more light leaks from the core to the cladding when the diameter decreases.

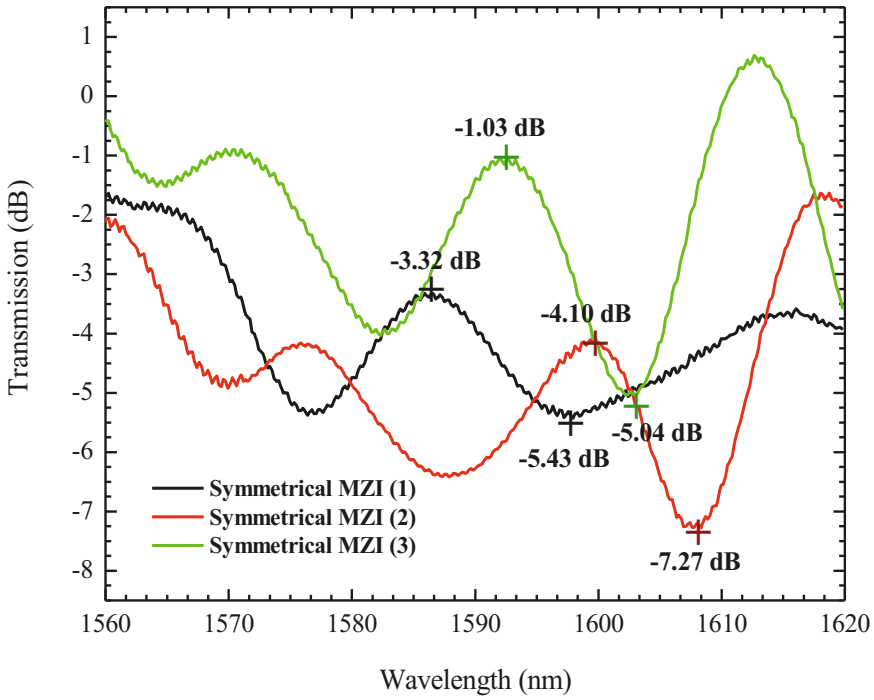

Figure 2-18 Transmission spectra of symmetrical tapered FMZIs with different waist diameters of 66.0, 62.5, and 58.0 μm, respectively.

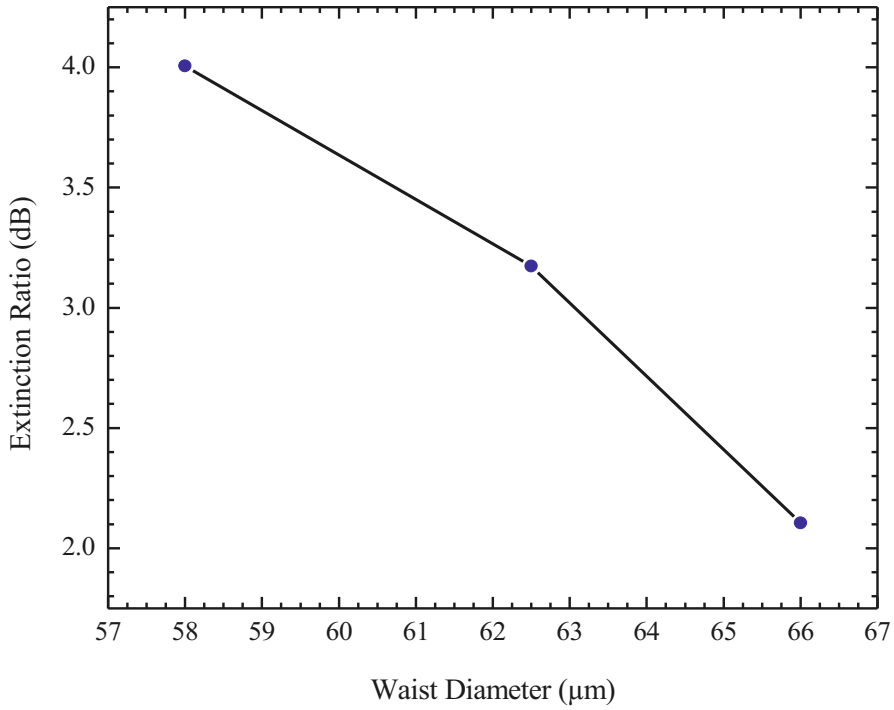

Figure 2-19 Effect of the waist diameter of symmetrical tapered FMZI on the extinction ratio of the fringes.

2.3.2 Asymmetrical Tapered Fiber Mach-Zehnder Interferometer

In this section, the fabrication method of the asymmetrical tapered fiber MZI will be discussed. The effect of the separation distance between the tapers, the propagation direction, and the waist diameter will be investigated.

2.3.2.1 Effect of Separation Distance Between Tapers

Similar to the fabrication of the symmetrical tapered fiber Mach-Zehnder interferometer, three samples have been prepared by the fusion splicing technique. However, in this experiment, the two tapers are structured to have different waist diameters

and lengths forming an asymmetrical MZI. The separation distances between the tapers are chosen as 2.0, 3.0, and 4.0 cm which are identical to those used in the symmetrical structure. The arc current and arc duration are fixed in all experiments. The forward movement of the stages is also fixed at 500.0 μm. On the other hand, their backward movement is changed to get tapers with different lengths and waist diameters.

For the fabrication of the first sample, the stages are moved reversely by 100.0 μm to obtain a taper (T1) of a waist diameter and a length of 66.7 and 420.7 μm, respectively. Away from (T1) by 2.0 cm, (T2) is fabricated when the fusion splicer stages are moved reversely by 80.0 μm so that the taper has a waist diameter and a length of 78.5 and 404.2 μm, respectively. Following the same steps, the second and third samples are fabricated with almost the same waist diameters and lengths of the tapers obtained by sample 1. However, the separation distance between the tapers is modified. The specifications of the second sample are $D1 = 66.7$, $D2 = 79.2$, $L1 = 419.4$, $L2 = 404.9$ μm, and $L_s = 3.0$ cm where $D1$ and $L1$ are the waist diameter and length of (T1), $D2$ and $L2$ are the waist diameter and length of (T2), and L_s is the separation distance between the tapers. Also, the specifications of the third sample are $D1 = 66.7$, $D2 = 77.8$, $L1 = 420.2$, $L2 = 407.0$ μm, and $L_s = 4.0$ cm.

Table 2-3 Characteristics of the three samples of the asymmetrical tapered FMZI.

L_s (cm)	$D1$ (μm)	$D2$ (μm)	$L1$ (μm)	$L2$ (μm)
2	66.7	78.5	420.7	404.2
3	66.7	79.2	419.4	404.9
4	66.7	77.8	420.2	407.0

Each sample is then connected to the light source and OSA and its transmission spectrum is detected before and after getting rid of the coating between the tapers. Figure 2-20 shows a schematic illustration of the experimental setup where (T1) (thin taper) excites the light propagating in the core to higher cladding modes and (T2) (thick taper) couples the light propagating in the cladding modes back to the core.

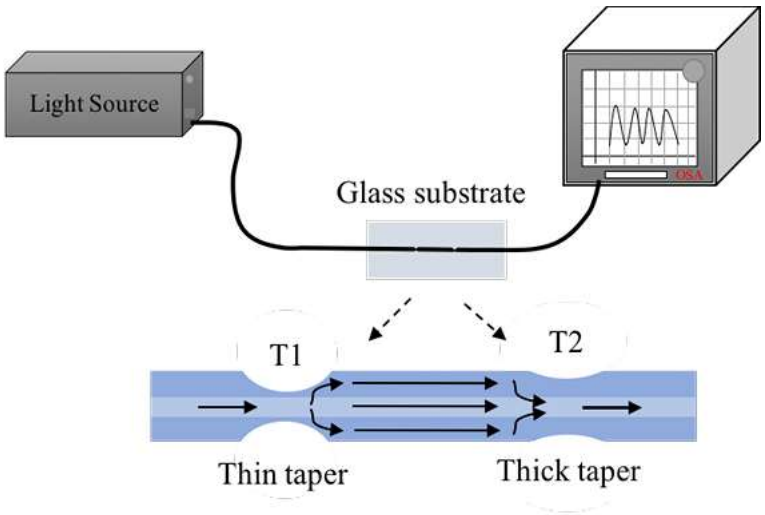

Figure 2-20 Schematic illustration of the experimental setup of an asymmetrical tapered FMZI when light passes from (T1) to (T2).

The interference patterns of the three samples before and after removal of the coating between the tapers when light in the fibers is excited from the fundamental mode to higher cladding modes by (T1) are shown in Fig. 2-21. It can be noticed that the interference patterns for the samples when the coating exists between the tapers are weak in comparison with those detected after removing the coating. The maximum extinction ratio for the AFMZI with a separation distance of 2.0 cm without coating is 9.02 dB when the intensities of the peak and the valley are -9.44 and -18.46 dB, respectively. The sample

with a separation distance of 3.0 cm shows a maximum extinction ratio of 10.52 dB after the removal of the coating, in which the peak and valley intensities are -1.81 and -12.33 dB, respectively. The interferometer with the largest separation distance of 4.0 cm shows a maximum extinction ratio of 6.44 dB (without coating) where the peak and valley intensities are -4.67 and -11.11 dB, respectively. It is found that the maximum extinction ratio for the asymmetrical fiber MZI with L_s = 3.0 cm is the highest among others with L_s values of 2.0 and 4.0 cm.

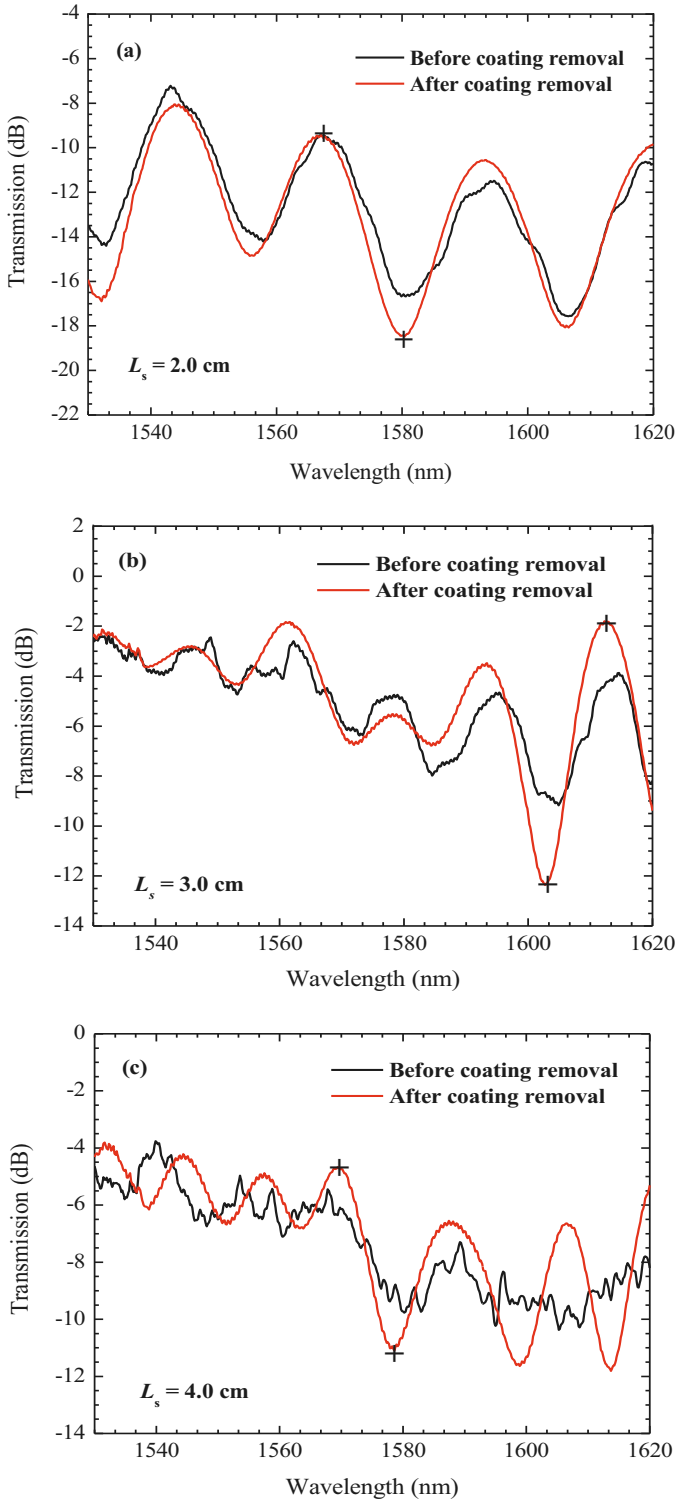

Figure 2-21 Transmission spectra of asymmetrical FMZIs with different lengths: (a) 2.0; (b) 3.0; and (c) 4.0 cm before and after removing the coating between the tapers.

The FSR of the asymmetrical tapered FMZIs changes with changing the separation distance between the tapers (Fig. 2-22). The periodicity between the interference peaks for the sample with L_s of 2.0 cm is 26.0 nm, as Curve (a) shows. It decreases to 18.36 nm when the separation distance becomes 3.0 cm (Curve (b)). Moreover, a periodicity of 14.76 nm is obtained for the sample with the L_s of 4.0 cm, as Curve (c) shows. It is found that the periodicity of the third asymmetrical FMZI is less than those obtained by the first and the second FMZIs. Figure 2-23 shows the relationship between the periodicity and the tapers separation distance. It can be concluded that the free spectral range in the case of asymmetrical tapered fiber MZIs decreases with increasing the separation distance between the two tapers.

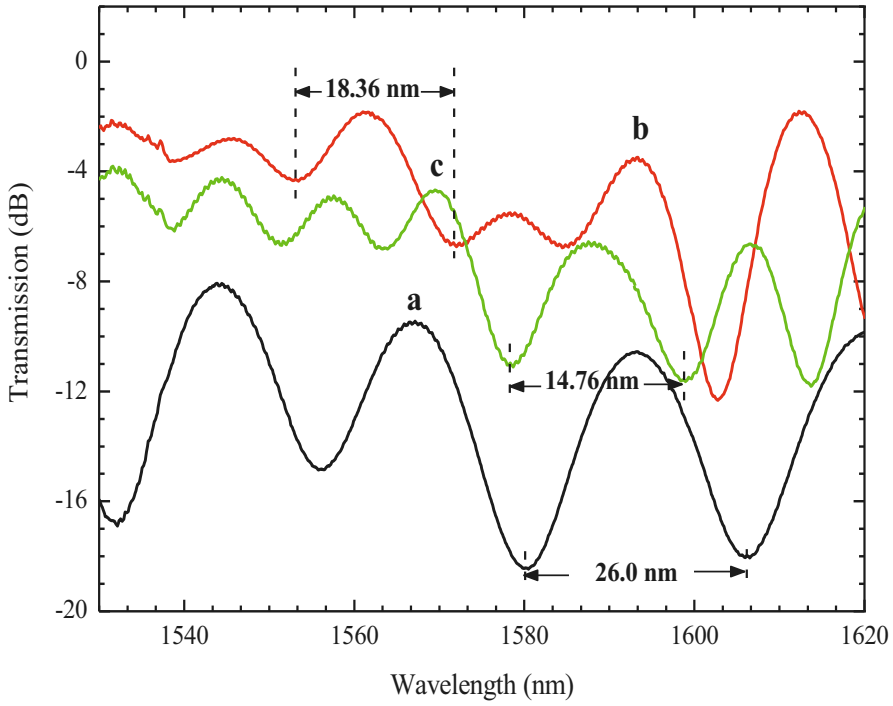

Figure 2-22 Free spectral range of asymmetrical tapered FMZIs with separation distances between the tapers of: (a) 2.0; (b) 3.0; and (c) 4.0 cm.

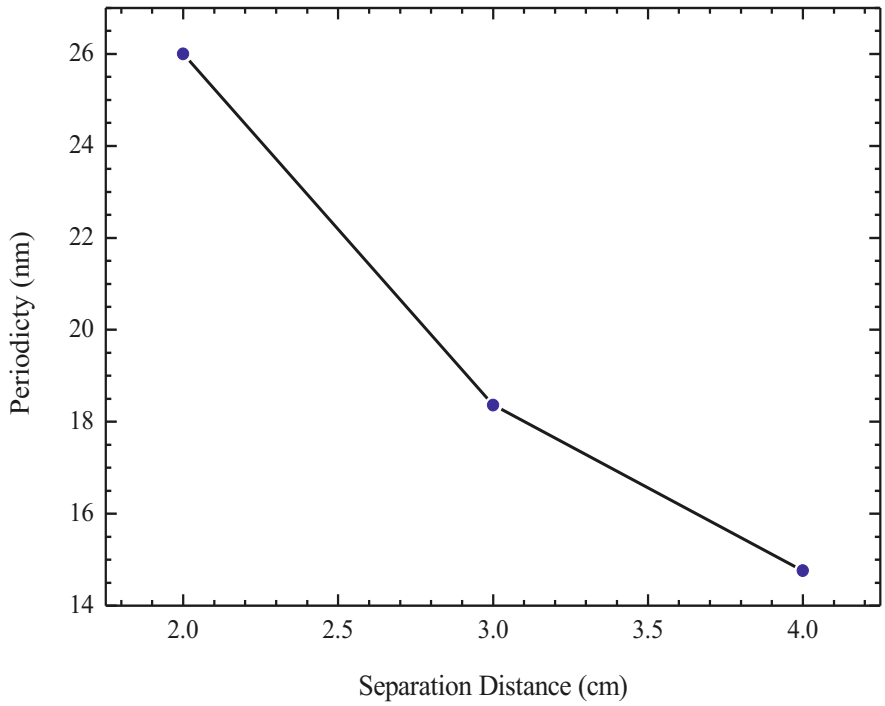

Figure 2-23 Effect of the separation distance between the tapers of asymmetrical tapered fiber MZIs on the periodicity of the fringes.

2.3.2.2 Effect of Propagation Direction

The same samples with the characteristics shown in Table 2-3 are used in order to study the effect of the propagation direction on the transmission spectra of the AFMZIs. In this experiment, the connections of the fibers with the light source and the optical spectrum analyzer are exchanged so that the electromagnetic waves split into two beams through the thick taper first (T2) and then recombine by the thin taper (T1) to form an interferometric pattern. A schematic diagram representing the experimental setup is shown in Fig. 2-24.

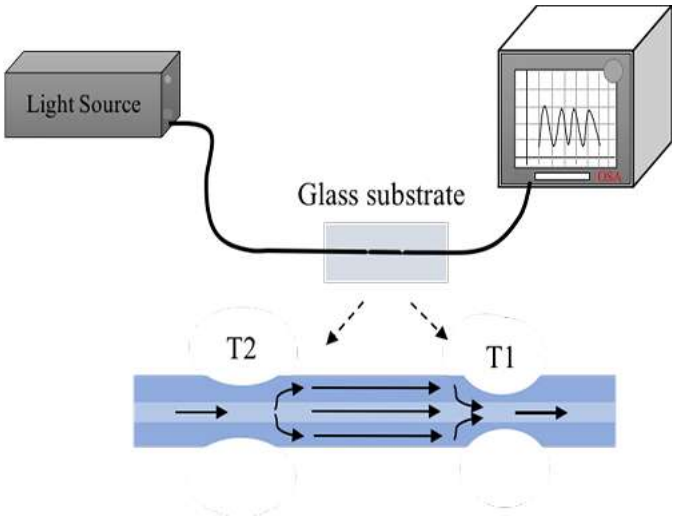

Figure 2-24 Schematic illustration of the experimental setup of an asymmetrical tapered FMZI when light passes from (T2) to (T1).

The reversed propagations which is obtained when light passes through the samples are compared with the forward propagations, as shown in Fig. 2-25(a-c). The sample with L_s of 2.0 cm has a maximum extinction ratio of 8.79 dB in the wavelength range between 1566.36 and 1579.86 nm. This ratio is 0.23 dB lower than the one obtained when light is excited through (T1) first. However, the interferometric sensor of the 3.0 cm separation distance shows a higher extinction ratio of 9.75 dB in the wavelength range between 1603.08 and 1612.62 nm, which is 0.77 dB lower than the one observed with light excitation through (T1). The maximum extinction ratio of the AFMZI with L_s of 4.0 cm, in the wavelength range between 1569.78 and 1578.42 nm, is 5.68 dB. This value is 0.76 dB lower than that obtained from the forward propagation of the light.

It can be concluded that in the case of asymmetrical tapered fiber Mach-Zehnder interferometer, switching the propagation direction has an influence on the maximum extinction ratio. The value of the maximum extinction ratio decreases when the propagation direction reverses.

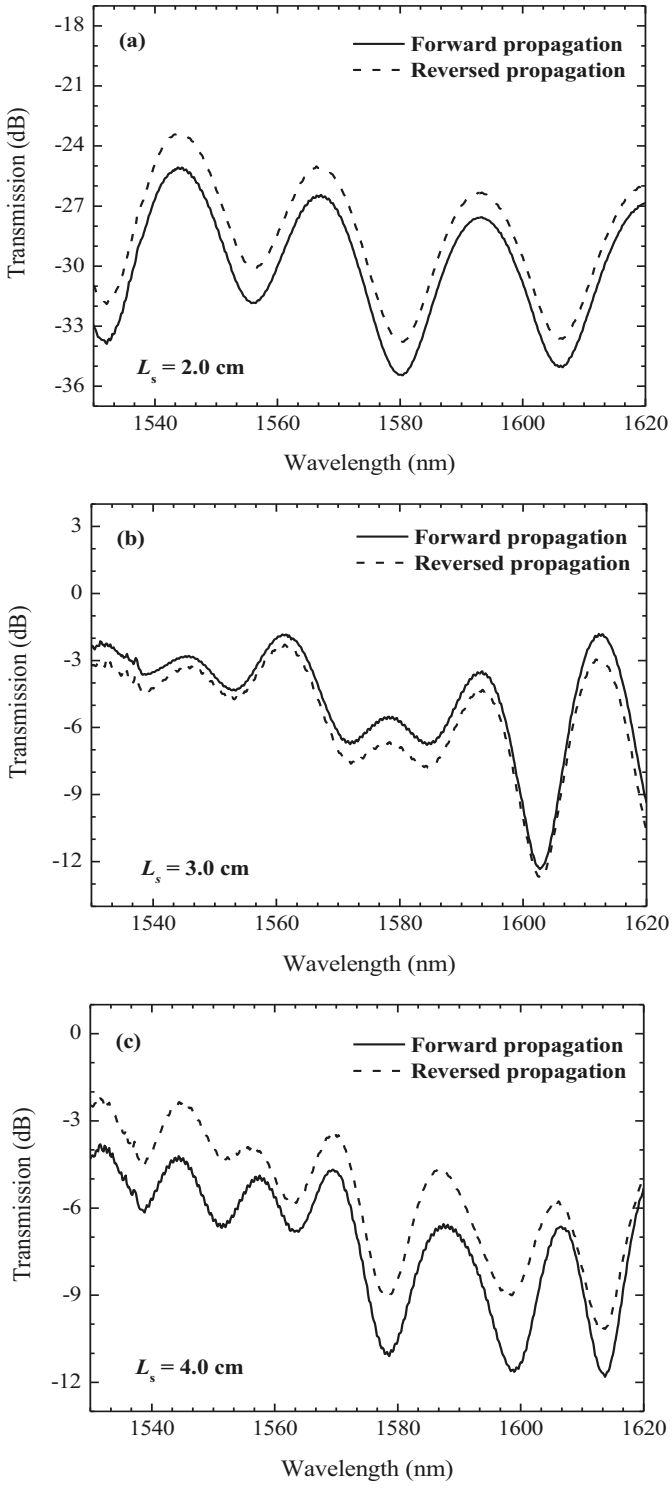

Figure 2-25 Transmission spectra of asymmetrical TFMZIs with different tapers separations: (a) 2.0; (b) 3.0; and (c) 4.0 cm when light propagates from (T1) to (T2) as well as it reverses propagation.

2.3.2.3 Effect of the Waist Size of Taper

As mentioned earlier, the waist diameter of a tapered fiber MZI controls its extinction ratio. To study the influence of this factor in the case of asymmetrical tapered FMZI, three samples with different waist diameters have been fabricated by the fusion splicing technique. The forward movement of the stages of the fusion splicer are set at a fixed distance of 500.0 μm. In the formation of (T1), the backward movement is set at 100.0 μm. However, it is set at 80.0 μm for the fabrication of (T2).

By applying an arc current only once, the waist of the fiber shrinks to 66.7 μm (T1) with a taper length of 419.4 μm. Because of the different applied strain, (T2) has a waist and a length of 79.2 and 404.9 μm, respectively, when applying the same arc current. Furthermore, when exposing the taper three times to the arc current, the waist diameters of the tapers reduce to 54.2 and 72.2 μm for (T1) and (T2), respectively. The waist diameters of the third sample are sharpened to 47.2 and 66.7 μm by applying the arc current five times.

Figure 2-26 represents the transmission spectra of the samples when the light propagates from (T1) to (T2). The extinction ratio of the transmission spectrum of each sample is calculated in the wavelength range between 1593 and 1604 nm. The first AFMZI , which is denoted as Asymmetrical MZI (1), shows an extinction ratio of 8.85 dB where the intensities of the peak and the valley are -3.48 and -12.33 dB, respectively. A lower extinction ratio of 3.04 dB is observed from Asymmetrical MZI (2) where the peak and the valley intensities are -6.38 and -9.42 dB, respectively. The extinction ratio obtained from light propagation through the tapers of the Asymmetrical MZI (3) is 7.38 dB. The

intensities for each of the peak and the valley for this sample are -5.26 and -12.64 dB, respectively.

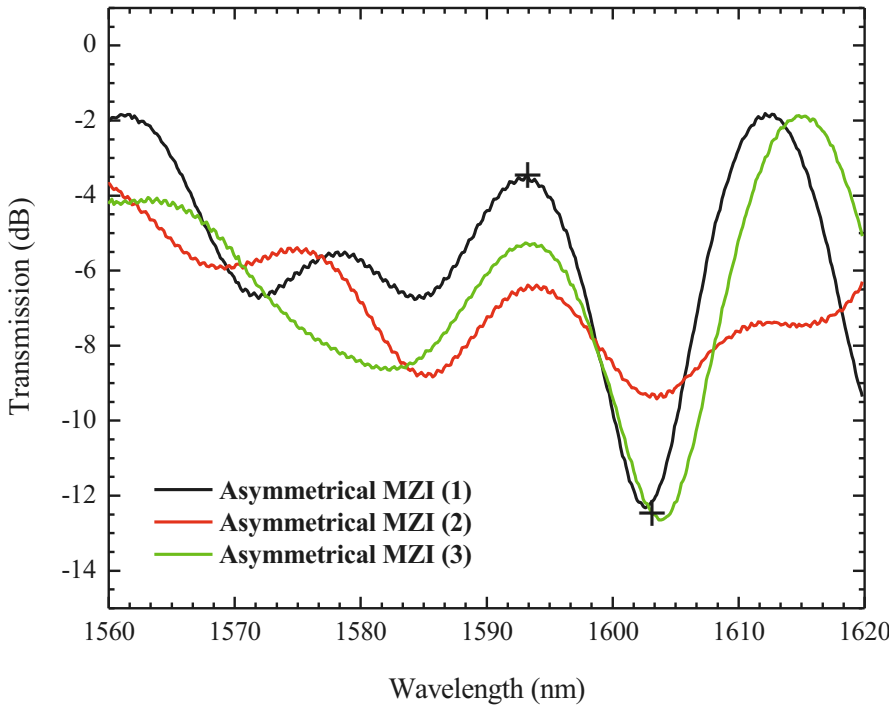

Figure 2-26 Interferometric patterns for three asymmetrical tapered FMZIs of different waist diameters with light propagation from (T1) to (T2): (a) 66.7 - 79.2 μm; (b) 54.2 - 72.2 μm; and (c) 47.2 - 66.7 μm.

Figure 2-27 demonstrates the interferometric patterns obtained from having the light propagate inside the samples inversely. The extinction ratio of the Asymmetrical MZI (1) is 8.39 dB which is lower than the one obtained from exciting the light through (T1) by 0.46 dB. The second sample, Asymmetrical MZI (2), shows an extinction ratio of 2.66 dB which is lower than the one obtained from the reversed propagation by 0.38 dB. The extinction ratio of the Asymmetrical MZI (3) is found to be 8.20 dB.

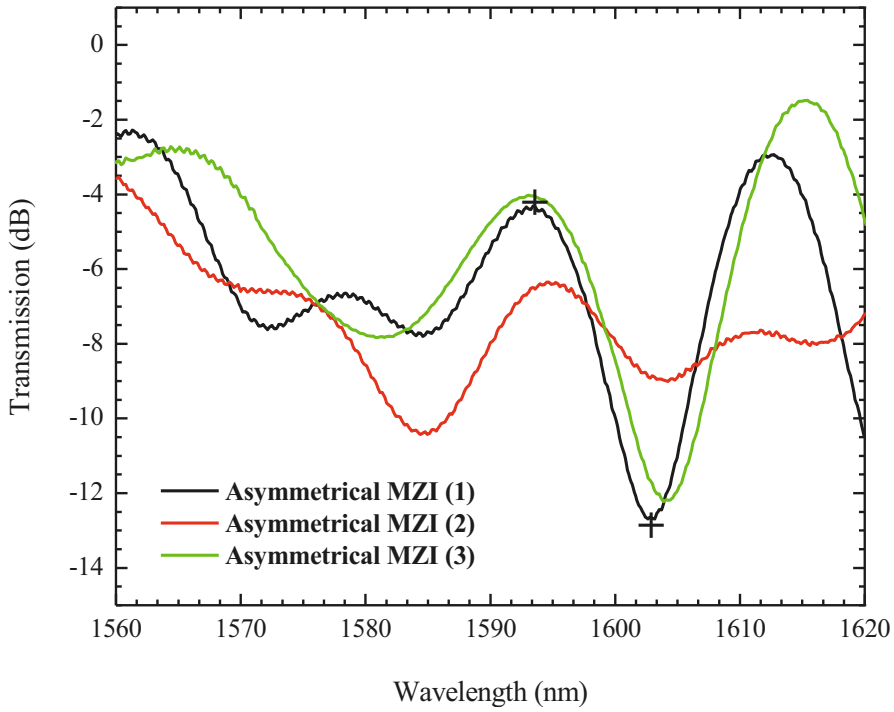

Figure 2-27 Interferometric patterns for three asymmetrical tapered FMZIs of different waist diameters with light propagation from (T2) to (T1): (a) 79.2 - 66.7 μm; (b) 72.2 - 54.2 μm; and (c) 66.7 - 47.2 μm.

Chapter 3

Symmetrical Tapered Fiber Biosensor Based on Nanostructured Coatings

Introduction

In order to fabricate sensing devices of optimal performance in terms of their sensitivity, cross-sensitivity, working range or time response, different aspects need to be taken into consideration. For example, the unique geometry of an optical fiber demands the capability to deposit the nanostructured films on a conical or cylindrical substrate [104]. Physical vapor deposition and spin-coating are two powerful techniques that were used for depositing films on flat substrates. However, these techniques are not feasible to produce uniform coatings on complex structures like optical fibers.

Successful deposition of uniform films onto the cylindrical structure of the optical fiber as well as the conical one was obtained using three different coating methods which

are the layer-by-layer method (LBL), Langmuir-Blodgett method (LB), and the dip coating method (DC) [104]. The first two techniques are useful for nanostructured coating deposition unlike the dip coating technique which is suitable for films deposition on cylindrical structures but not on the nano-scale. The Langmuir-Blodgett technique requires the molecules consisting of lipophilic part combined with hydrophilic one. On the other hand, the self-assembly technique is sufficient for using different species like polymers, DNA strands, antibodies, enzymes and many other examples [104].

Historically, the LBL method did not attract significant attention after its first discovery in the 1960s by R. Iler [104]. It was regenerated later on by G. Decher and was extended from using the oppositely charged colloids to polyelectrolytes, nanoparticles and other diverse structures. Different names appeared referring to this technique such as the electrostatic self-assembly (ESA) and the ionic self-assembly monolayer/or multilayer technique (ISAM). The technique relies on the electrostatic force between positive and negative charge polyelectrolytes. The technique requires several steps. First, cleaning and treating the substrate to be used in order to charge its surface [104]. In our case the substrate is the tapered fiber MZI. Second, exposing the charged substrate to a polyinion solution which has a charge that is opposite to the one of the optical fiber for a few minutes [104]. When the polyinions are adsorbed by the surface of the substrate, a monolayer is obtained. For the creation of multilayered nanostructured coatings, the substrate is dipped alternatively into polyinions and polycations. The oppositely charged monolayers combined together are referred to as one bilayer, for which the thickness can be changed by adjusting the deposition parameters [104].

The LBL technique is simple, which can be applied to various types of charged nanoparticles and polymers. On the other hand, it is affected significantly by the environmental conditions such as humidity. Moreover, the monolayers that form a bilayer interfere with each other causing the inner boundary of the film to become fuzzy [105]. This technique was utilized for sensing different physical and chemical parameters such as humidity [106-108], RI [109, 54], PH [110], or ammonia [111]. However, biological parameters like anti-IgG [112] and streptavidin [113, 114] can be detected using the same technique.

In this chapter, the LBL technique is used to fabricate a biosensor based on thin films deposited on a symmetrical tapered fiber MZI for the detection of a type of proteins called streptavidin (SV) which was introduced earlier in this thesis. The symmetrical structure is used in this study to make the discussion about the biosensor simple since it is convenient to control the properties of the symmetrical MZI in comparison with the asymmetrical structure.

The films fabricated here are based on the deposition of PAH with either of the two different anionic materials, i.e., gold nano-shells or poly (sodium 4-styrenesulfonate) (PSS). The films are fabricated on the tapered region of the symmetrical FMZI. The tapers have waist diameters, and lengths of 58.0 and 378.0 μm, respectively. Moreover, the selected separation distance between the tapers is 4.0 cm. The interference pattern shown in Fig. 3-1 is observed in the light transmission through a MZI in the wavelength range from 1530 to 1620 nm. The OSA resolution is 0.05 nm.

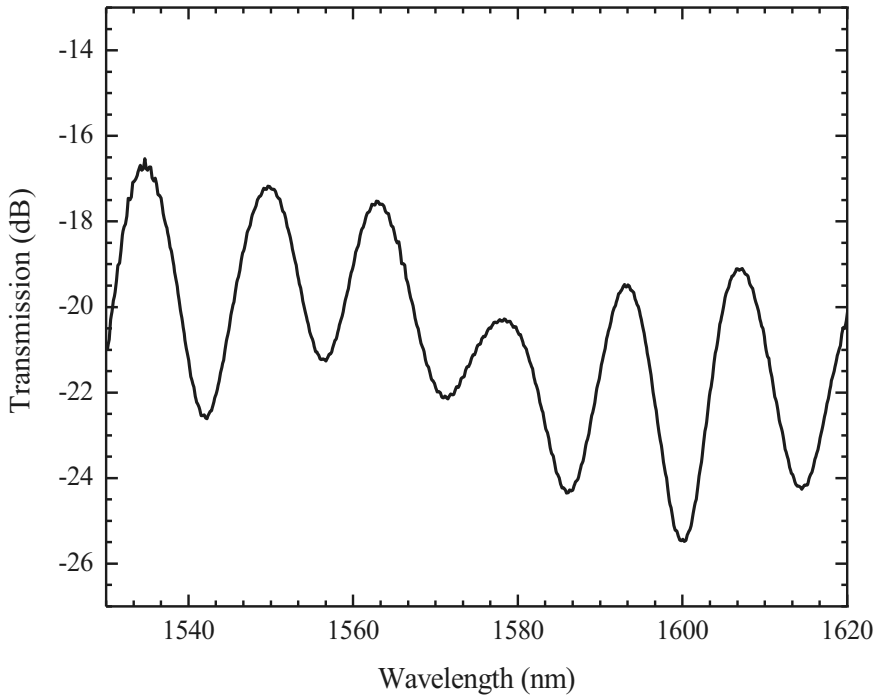

Figure 3-1 Transmission spectrum of a symmetrical tapered fiber MZI with a waist diameter of 58.0 μm and a separation distance of 4.0 cm between the tapers.

3.1 Materials

Ethanol (99%) and KOH were available locally in the university chemical store. Poly (allylamine hydrochloride) (PAH) (M_w ~ 17,500 Da), biotin (M_w ~ 240 Da), streptavidin from bacterium streptomyces avidinii (M_w ~ 60,000 Da), and poly (sodium 4-styrenesulfonate) (PSS) (M_w ~ 70.000 Da) were purchased from Sigma-Aldrich Corp. Negatively charged gold nano-shells with a concentration of 0.05 mg/mL, total diameter of 241 ± 14 nm, and surface functionalization by lipoic acid were purchased from the nanoComposix, Inc. (Product Number: GSPN980-25 M). Distilled water and dimethyl sulfoxide (DMSO) were solvents supplied locally.

3.2 Tapered Fiber MZI Based on (PAH/SiO_2:Au NPs) Film

The use of SiO_2:Au NPs in the fabrication of thin films provides several merits. It is possible to control the properties of both silica and gold nanoparticles for the fabrication of a sensing device with an optimal sensitivity [62]. Silica nanoparticles affect the thickness of the film. Therefore, by optimizing their specifications such as the diameter, the evanescent field propagating in the optical fiber interacts with the film effectively. Also, the diameter of the silica nanoparticles affects the porosity of the film. The optimization of the diameter makes the fabrication of highly porous films possible [62]. On the other hand, the advantage of gold nanoparticles is found in their ability to provide highly selective devices when their surfaces are functionalized with diverse types of materials. The existence of the molecules of the material under investigation can be connected to the surface plasmon resonance property of the gold nanoshells. Moreover, when they are combined with the silica nanoparticles, they enhance the stability of the sensor [62].

As mentioned previously, two symmetrical tapers of waist diameters and lengths of 58.0 and 378.0 μm are inscribed on a single-mode fiber for MZI fabrication. This sample is prepared for biosensing applications by coating a multilayered nano-film on its surface. Figures 3-2 and 3-3 show the fabrication process of the film which involves the treatment of the tapered FMZI with 1 wt% of ethanolic KOH solution (99% ethanol: water) = (3:2, v/v) for 15 minutes. The importance of this step lies in negatively charging the surface of the fiber so that the PAH monolayer can be attached to it. Later, the sample is dipped into

0.5 wt% of the cationic polymer PAH and then into the negatively charged SiO_2:Au NPs each for 15 minutes forming one bilayer of (PAH/SiO_2:Au NPs). The fiber is dipped back and forth between the PAH and SiO_2:Au NPs to obtain the desired number of bilayers. After each one of the previous steps, the fiber is washed to get rid of unbounded molecules and dried in air for 15 minutes. The surface of the NPs is then functionalized with 7.0 mM of biotin for 30 minutes. Biotin is dissolved in (DMSO: water) = (3:3, v/v). The MZI then is used to detect different concentrations of streptavidin. The chemical structure of PAH and biotin are shown in Fig. 3-4.

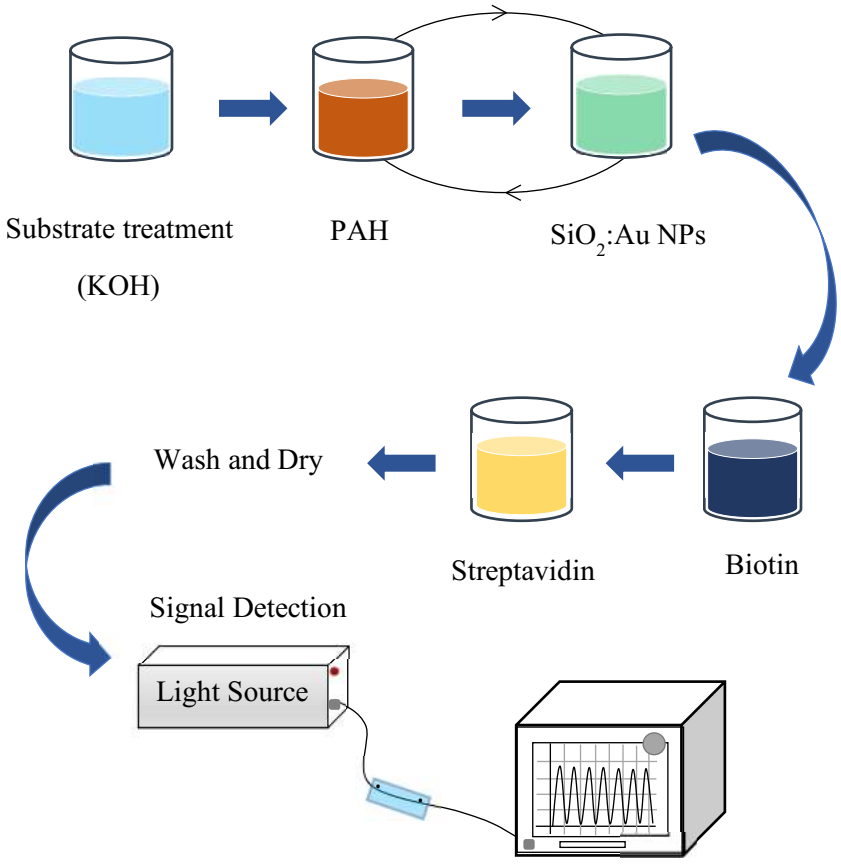

Figure 3-2 Schematic illustration of the steps of the layer-by-layer technique in this study.

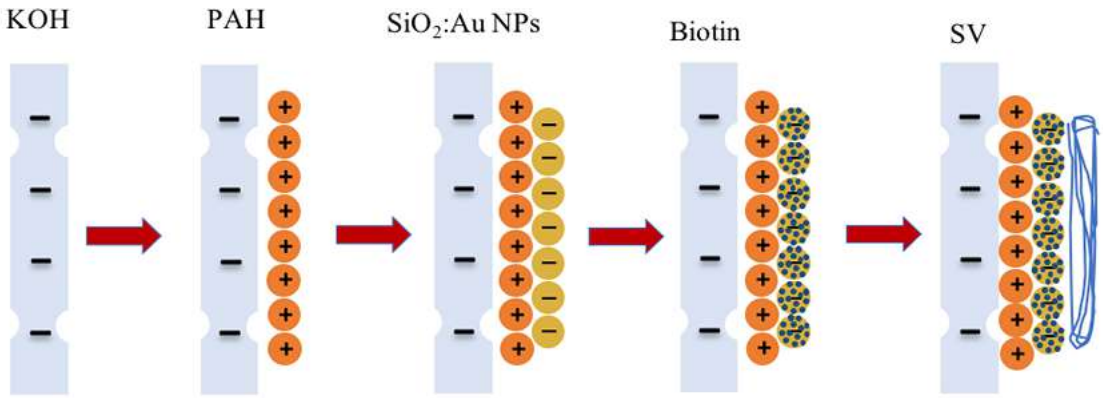

Figure 3-3 Schematic illustration of the deposition of a (PAH/SiO_2:Au NPs) film onto a symmetrical tapered fiber MZI using the layer-by-layer technique.

(a) (b)

Figure 3-4 Chemical structures of: (a) PAH and (b) biotin.

3.2.1 Detection of Streptavidin

After the selection of the optimal tapers characteristics, we come to the last step which is to examine the efficiency of the newly created sensor towards our selected biomaterial which is streptavidin. In this experiment, three bilayers of PAH/SiO_2:Au NPs are coated on the surface of a symmetrical tapered fiber MZI with functionalization of the film with biotin. First, the optical spectrum is detected in water for bare fiber MZI. Second, three bilayers of PAH/SiO_2:Au NPs are coated on the surface of the tapered area of the MZI and functionalized with biotin. Third, the spectrum of the MZI after coating the film and the functionalization with biotin is also detected in water. The transmission spectrum of the bare fiber MZI in water is detected in the wavelength range between 1530 and 1580 nm, as shown in Fig. 3-5. The peak at a wavelength of 1553.22 nm is selected. On the other hand, the curve denoted by (PAH/SiO_2:Au NPs)$_3$/biotin) shows the transmission spectrum of the MZI after the film fabrication and the functionalization with biotin. The Peak at 1553.22 nm in this case shifts towards the shorter wavelength region (blue-shift) and its position becomes at a wavelength of 1553.04 nm. The wavelength shift between the two spectra is 0.18 nm. Fourth, the fiber is immersed in an aqueous solution of streptavidin with a concentration of 83 nM. The transmission spectrum is detected and the curve is denoted by (83 nM-SV) in Fig. 3-5. It is found that the peak shifts from 1553.04 nm to a shorter wavelength of 1552.86 nm resulting in a shift of 0.18 nm. When the fiber is immersed in streptavidin of concentrations of 0.3 and 1.3 μM, the peak wavelength shifts to 1552.77 nm leading to a wavelength shift of 0.27 nm. A further blue-shift is obtained when the sample is immersed in a 0.8 μM solution of streptavidin where the peak wavelength shifts to

1552.68 nm. In this case, the wavelength shift is calculated to be 0.36 nm which is the maximum wavelength shift obtained and it can be used to calculate the sensitivity of the device.

The sensitivity of a sensor that detects biomolecules is usually given by the equation [62]:

$$S = \frac{\Delta\lambda_{\max}}{\sigma} \tag{3-1}$$

where $\Delta\lambda_{\max}$ is the maximum wavelength shift observed after the exposure to streptavidin concentrations and σ is the surface density of the detected biomaterial which is described by the equation [115]:

$$\sigma = \frac{M_{\mathrm{mw}}}{N_A \times P^2} \tag{3-2}$$

where M_{mw} is the molecular weight of streptavidin ($M_{\mathrm{mw}} = 60.000$ Da), N_A is Avogadro's number, and P is the average length of streptavidin which is 4.0 nm [116, 117]. As a result, σ = 6.23 ng/mm^2 [116] and hence the sensitivity of the sensor is 0.06 nm/(ng/mm^2). Figure 3-6 shows the peak at 1553.22 nm after coating (PAH/SiO_2:Au NPs)$_3$/biotin, and after the streptavidin binding.

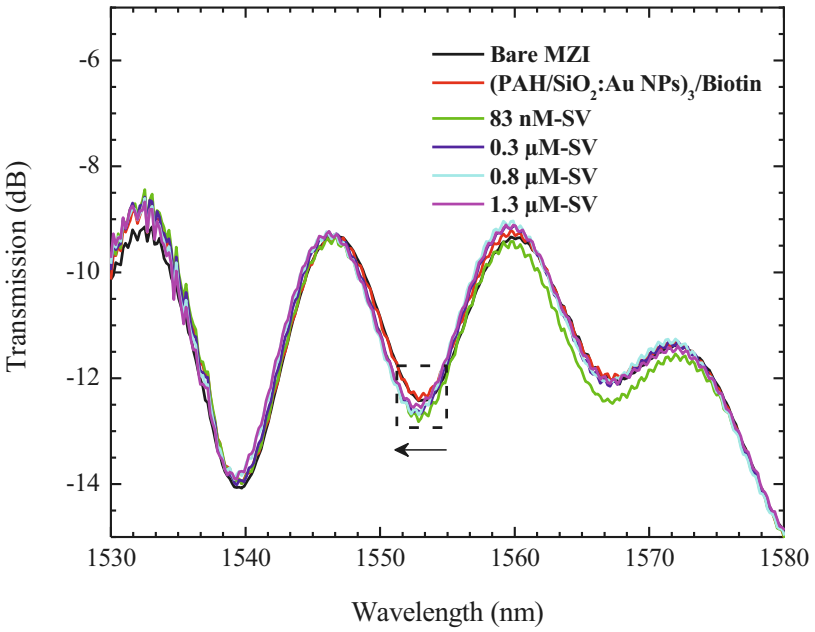

Figure 3-5 Transmission spectra of tapered MZI (1) before coating, after coating (PAH/SiO_2:Au NPs)$_3$/biotin film, and after streptavidin binding.

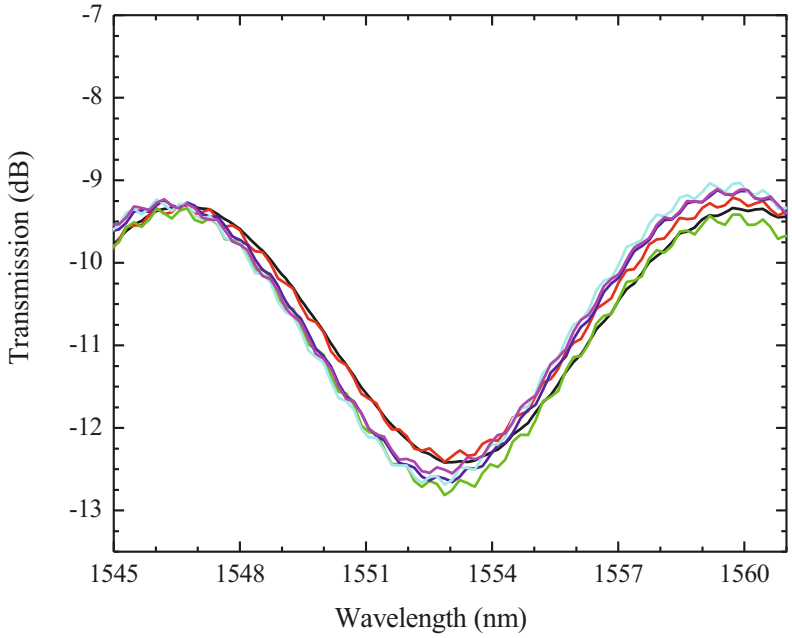

Figure 3-6 Transmission spectra of tapered MZI (1) before coating, after coating (PAH/SiO_2:Au NPs)$_3$/biotin film, and after streptavidin binding at λ = 1553.22 nm.

The wavelength shift of the peak at 1553.04 nm as a function of the streptavidin concentration is evaluated in Fig.3-7. It can be noticed that the wavelength shift for the lowest concentration of streptavidin has the minimum value. This value increases with increasing SV concentration and reaches a maximum at 0.8 μM. This response is attributed to increasing the effective refractive index of the cladding with increasing the streptavidin concentration which results in reducing the difference between the effective refractive indices of the core and the cladding and shifting the wavelength to the shorter wavelength region. The decrease in the wavelength shift which is caused by immersing the sample in the 1.3 μM streptavidin solution can possibly be related to the fact that the surface of the gold nanoshells is already functionalized with lipoic acid which limits further adhesion of biotin. As a result, the biotin is possibly attached weakly to the nanoparticles and hence might be washed away during the washing process.

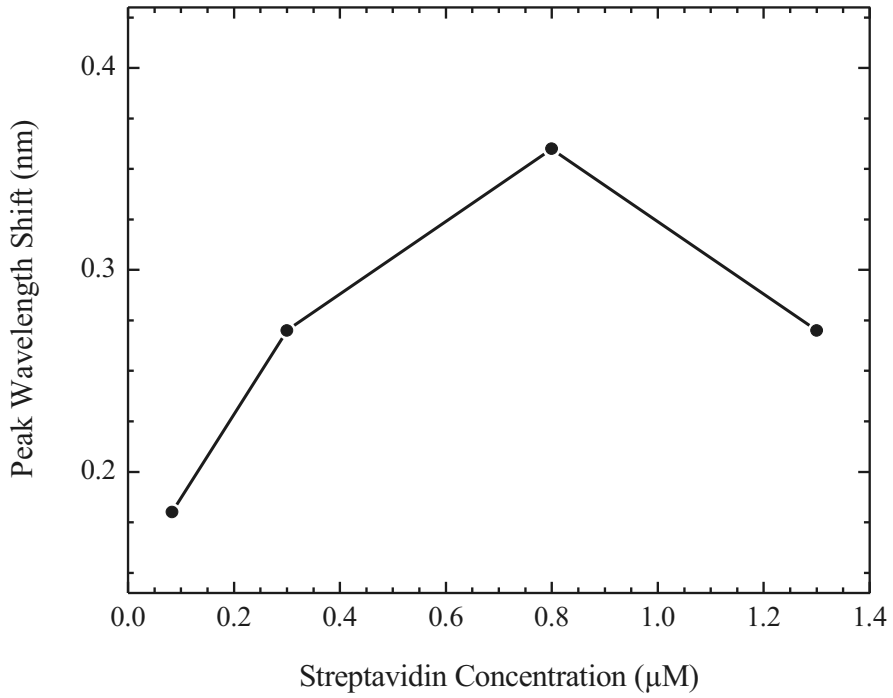

Figure 3-7 Wavelength shift at 1553.04 nm as a function of streptavidin concentration.

Another sample is prepared with the same materials but this time the number of bilayers is increased and the (PAH/SiO_2:Au NPs) film is exposed directly to aqueous solutions of streptavidin without functionalizing the film with biotin. In this expermient, five bilayers of PAH/SiO_2:Au NPs are coated on MZI (2) for the purpose of studying the effect of increasing the number of layers on the sensitivity of the sensor. The transmission spectrum of the bare fiber MZI (2) is presented in Fig. 3-8. The selected peak locates at 1547.28 nm. However, after the fabrication of the five (PAH/SiO_2:Au NPs) bilayers, the peak wavelength shifts twards a shorter wavelength of 1547.19 nm. The wavelength shift of the peak is found to be 0.09 nm. The curve denoted by (83 nM-SV) represents the transmission spectrum after depositing streptavidin of 83 nM concentration on the film. The transmission spectrum experiences a blue-shift. As a result, the wavelength of the peak at 1547.19 nm changes to 1546.92 nm. The resultant wavelength shift after exposing the device to the lowest concentration of streptavidin is 0.27 nm. On the other hand, streptavidin concentrations of 0.3 and 1.3 μM cause the peak wavelength to shift by 0.36 nm where the position of the peak changes from 1547.19 nm before the exposure to streptavidin solutions to 1546.83 nm after the exposure. A maximum wavelength shift of 0.45 nm is observed when the MZI is exposed to a streptavidin solution of 0.8 μM. This concentration makes the peak wavelength shifts to λ = 1546.74 nm. Finally, the sensitivity of the sensor is found to be 0.07 nm/(ng/mm^2). Figure 3-9 shows the peak at 1547.28 nm after coating the film and its response to different streptavidin concentrations.

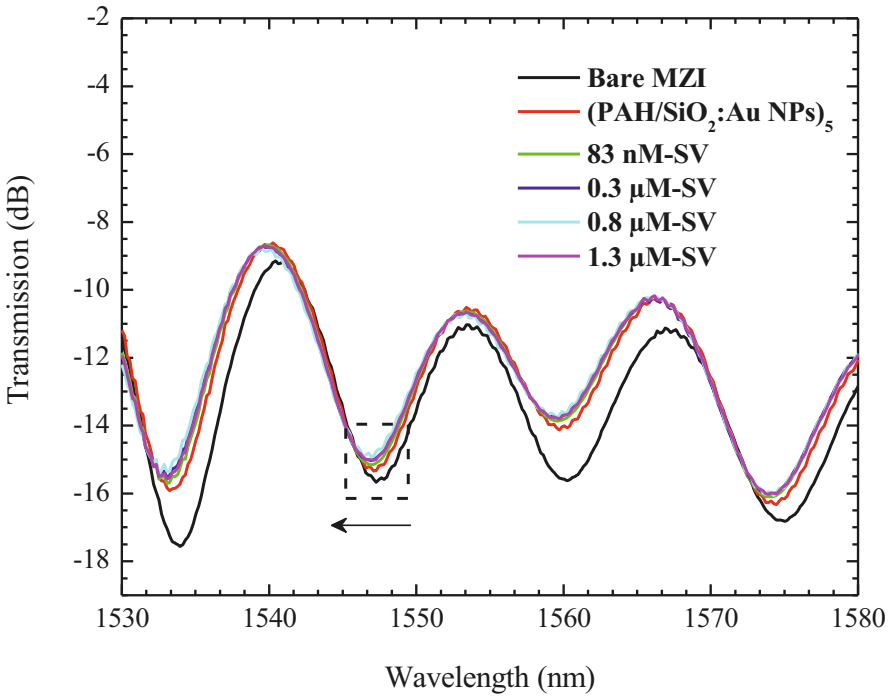

Figure 3-8 Transmission spectra of tapered MZI (2) before and after coating $(PAH/SiO_2:Au\ NPs)_5$ as well as their exposure to different streptavidin concentrations.

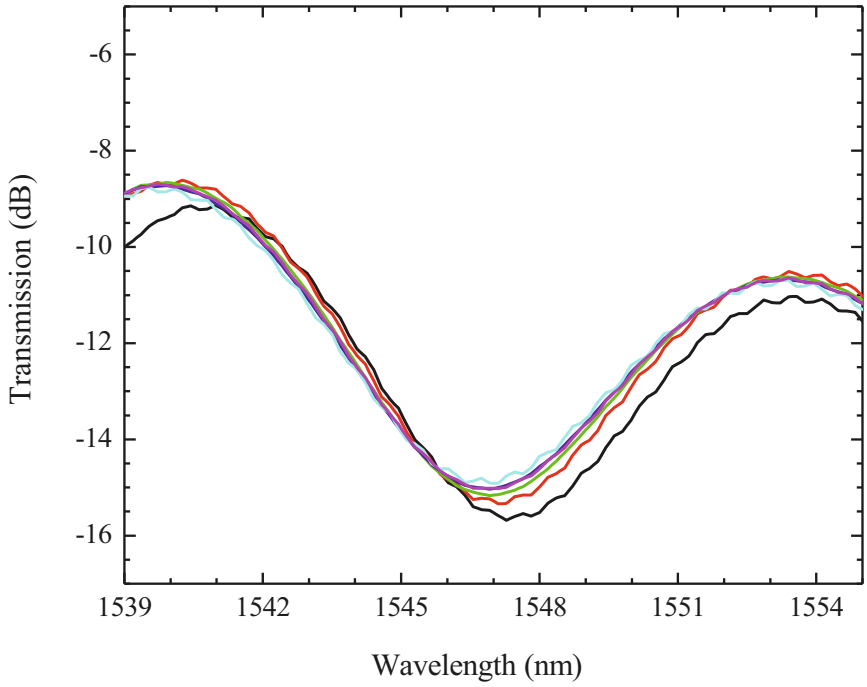

Figure 3-9 Transmission spectra of tapered MZI (2) after coating $(PAH/SiO_2:Au\ NPs)_5$ as well as their exposure to different streptavidin concentrations at λ = 1547.28 nm.

The relationship between the peak wavelength shift and the streptavidin concentration is shown in Fig. 3-10. The wavelength shift increases with increasing the concentration of streptavidin for the concentrations between 0.083 and 0.8 μM. A decline in the wavelength shift curve is observed at a streptavidin concentration of 1.3 μM. The reason behind this response can be linked to the fact that the nanoparticles we use here are functionalized with lipoic acid as received. Usually, the functionalization of the nanoparticles is performed after the film formation, in which only the final layer of the film (the nanoparticles) will be functionalized. Since nanocomposix, Inc. is the sole supplier of the gold nanoshells with functionalized gold nanoparticles with lipoic acid, the bonds between the bilayers of the film might be weak and some nanoparticles might be lost during the washing process. Another reason might be the number of binding sites of lipoic acid that are occupied with streptavidin. The wavelength shift will possibly increase and reach a maximum if the binding sites are fully occupied with streptavidin.

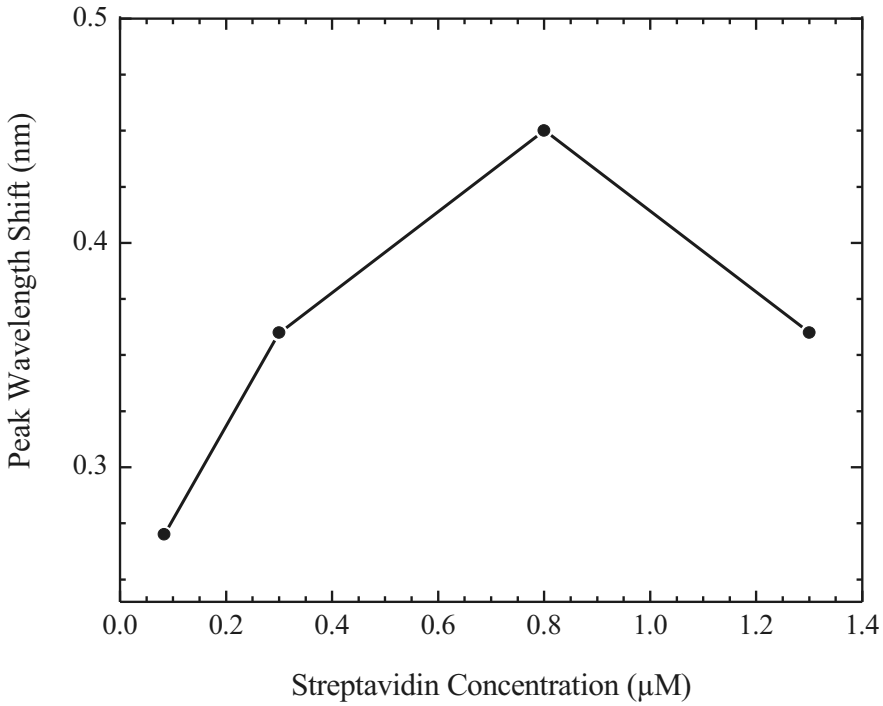

Figure 3-10 Wavelength shift of the peak at 1547.19 nm as a function of streptavidin concentration.

Another sample is prepared for coating seven bilayers of PAH/SiO_2:Au NPs on MZI (3). Figure 3-11 shows the transmission spectra of MZI (3) before and after coating the $(PAH/SiO_2:Au\ NPs)_7$ film as well as after binding of streptavidin. The peak locates at a wavelength of 1549.62 nm when the transmission spectrum of the bare MZI (3) is detected in water. After the tapered area is coated with the film, the transmission spectrum blue-shifts and the peak wavelength changes to 1549.53 nm. The wavelength shift caused by the film deposition is 0.09 nm. When the sample is exposed to an aqueous streptavidin solution of 83 nM concentration, the peak wavelength becomes at λ = 1549.44 nm, which results in a wavelength shift of 0.09 nm. The higher streptavidin concentration of 0.3 μM causes the peak wavelength to shift to the shorter wavelength region by 0.18 nm where its position changes from 1549.53 to 1549.35 nm. The biggest wavelength shift is obtained by the last

two streptavidin solutions of concentrations of 0.8 and 1.3 μM and its value is 0.27 nm where the peak wavelength locates at 1549.26 nm. Considering $\Delta\lambda_{max}$ = 0.27 nm, the sensitivity of the sensor is 0.04 nm/(ng/mm^2) calculated using Equation 3-1.

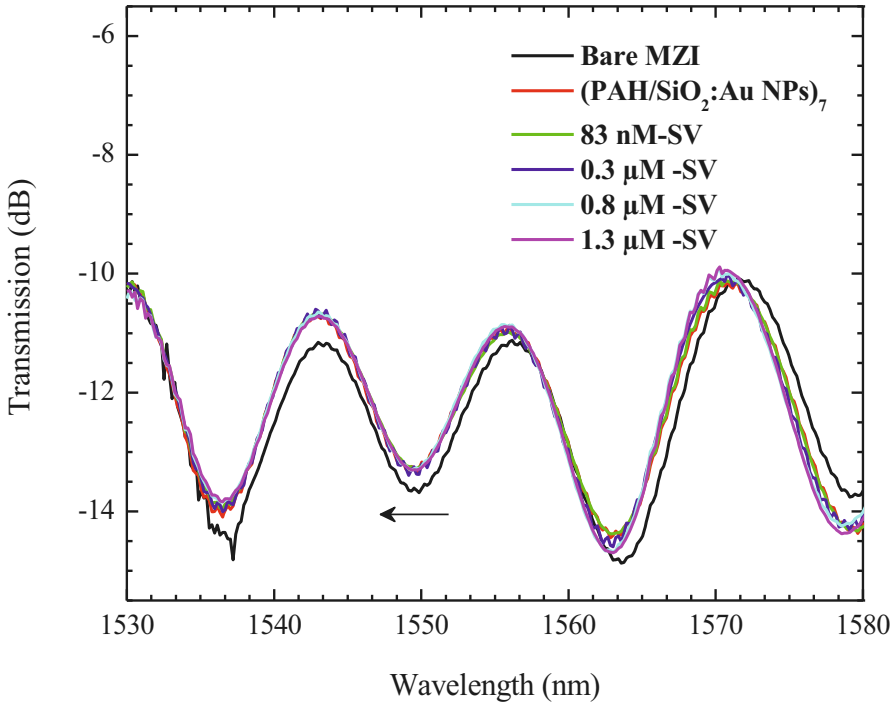

Figure 3-11 Transmission spectra of tapered MZI (3) before and after coating (PAH/SiO_2:Au NPs)$_7$ film as well as their exposure to different streptavidin concentrations.

The relationship between the wavelength shift of the peak locates at 1549.53 nm and streptavidin concentrations is shown in Fig. 3-12. It can be obtained that the peak wavelength shift increases with increasing the streptavidin concentration and reaches a saturation in the region between 0.8 and 1.3 μM.

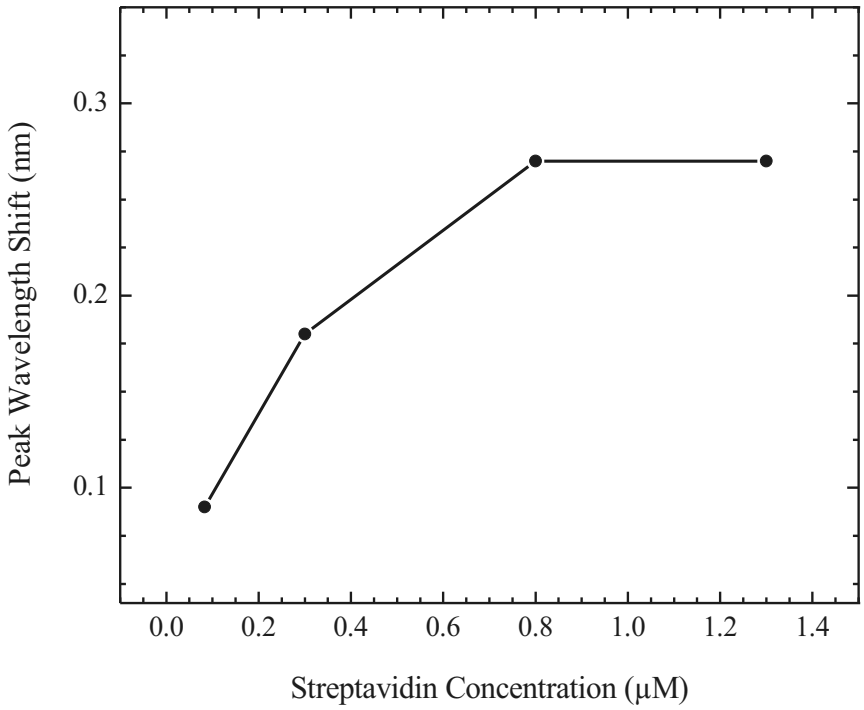

Figure 3-12 Wavelength shift of the peak at 1549.53 nm as a function of streptavidin concentration.

Form the obtained results, it can be concluded that the sensitivity of the sensor without the film functionalization with biotin decreases with increasing the number of layers. A possible reason is that increasing the number of layers makes the interaction between the evanescent field and the target material (streptavidin) limited. When the number of layers reduces, the streptavidin will interact more effectively with the evanescent field.

3.3 Tapered Fiber MZI Based on (PAH/PSS) Film

For the fabrication of a multilayered (PAH/PSS) film on the surface of a tapered symmetrical fiber MZI, the same steps explained in Section 3.2 are followed. Instead of depositing negatively charged gold nanoshells on the PAH monolayer, PSS is used while the materials (i.e. KOH, PAH, biotin, and streptavidin) concentrations and immersion and drying times are the same. The PSS concentration is 0.5 wt% dissolved in distilled water. The molecular structure of the PSS polymer is shown in Fig. 3-13.

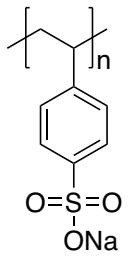

Figure 3-13 Molecular structure of PSS polymer.

3.3.1 Detection of Streptavidin

The layer-by-layer technique is also applied on the symmetrical tapered fiber MZI to create a multilayered structure. However, in this Section, PSS polymer is used as the anionic material and is attached to the PAH. First, three bilayers of PAH/PSS film are coated on a MZI (labeled as MZI (4)). Figure 3-14 shows the transmission spectra of the sample detected in water before coating the $(PAH/PSS)_3$ film, after coating and functionalizing the film with biotin, and after the binding of streptavidin. The transmission spectrum of the bare MZI is detected in the wavelength range between 1530 and 1580 nm.

In this case. For the peak at λ = 1550.07 nm, the transmission spectrum exihibits a blue-shift after the fabrication of the three bilyers film and the functionalization of the film by biotin. Due to the resultant shift, the wavelength moves to 1549.26 nm and hence the calculated peak wavelength shift is 0.81 nm. When the sample is immersed in an aqueous solution of streptavidin of 83 nM, the transmission spectrum shifts to the shorter wavelength region as a result of binding streptavidin with biotin. The peak wavelength moves from 1549.26 to 1548.54 nm and the resultant wavelength shift is 0.72 nm. When the sample is immersed in a streptavidin solution of 0.3 μM, the peak wavelength shifts to λ = 1548.45 nm causing a wavelength shift of 0.81 nm. However, the aqueous streptavidin solution of 0.8 μM creates a change in the wavelength of the peak which appears at 1547.82 nm so that the wavelength shift caused by this concentration is 1.44 nm. The wavelength shift caused by immersing the sample in an aqueous solution of streptavidin of 1.3 μM is 1.8 nm where the peak wavelength blue-shifts to 1547.46 nm.

Figure 3-15 shows the dependency of the wavelength shift of the peak at 1549.26 nm on streptavidin concentrations. The wavelength shift value increases with increasing the concentration of streptavidin as a result of increasing the effective refractive index of the cladding and hence decreasing the difference between the effective refractive indices of the core and the cladding. The wavelength shift reaches a maximum of 1.8 nm when the concentration of streptavidin is 1.3 μM. By considering $\Delta\lambda_{\max}$ = 1.8 nm, the sensitivity of MZI (4) is found to be 0.29 nm/(ng/mm^2) using Equation 3-1.

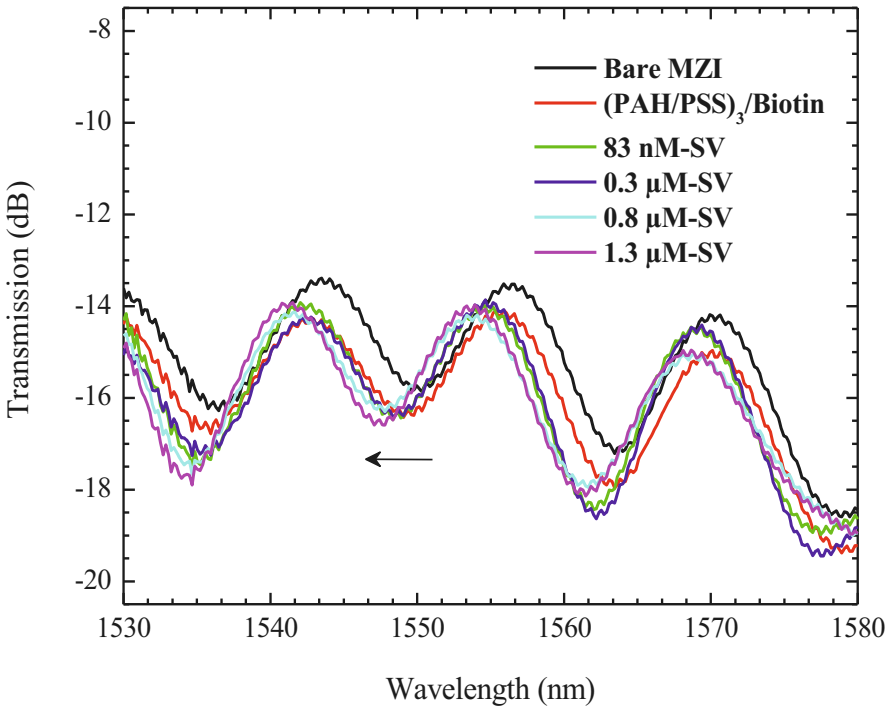

Figure 3-14 Transmission spectra of tapered MZI (4) before and after coating $(PAH/PSS)_3$/Biotin as well as their exposure to streptavidin solutions of different concentrations.

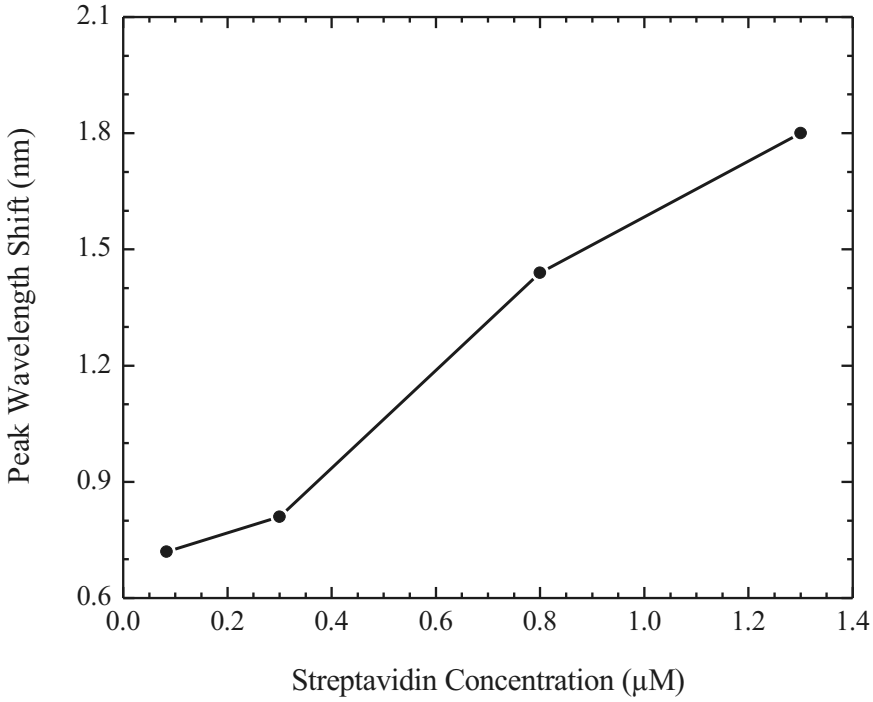

Figure 3-15 Wavelength shift of the peak at 1549.26 nm as a function of streptavidin concentration.

Furthermore, five bilayers of PAH/PSS film are deposited on a MZI (labeled as MZI (5)). The transmission spectrum before coating the film is rcorded in water and denoted in Fig. 3-16 as (Bare MZI). The selected peak locates at a wavelength of 1540.26 nm. Its position changes to λ = 1540.17 nm after the deposition of the $(PAH/PSS)_5$ film and the functionalization with biotin. The wavelength shift is found to be 0.09 nm. However, when the sample is immersed in an aqueous solution of steptavidin of 83 nM, the peak wavelength blue-shifts from 1540.17 to 1539.72 nm. The calculated wavelength shift in this case is 0.45 nm. The wavelength shift obtained by immersing the sample in a streptavidin solution of 0.3 μM is 0.54 nm where the peak wavelength shifts to λ = 1539.63 nm. The wavelength shifts obtained by the other two concentrations of streptavidin (0.8 and 1.3 μM) are 0.63 and 0.72 nm, respectively. These shifts are resulted from moving the peak wavelengths to λ = 1539.54 and 1539.45 nm.

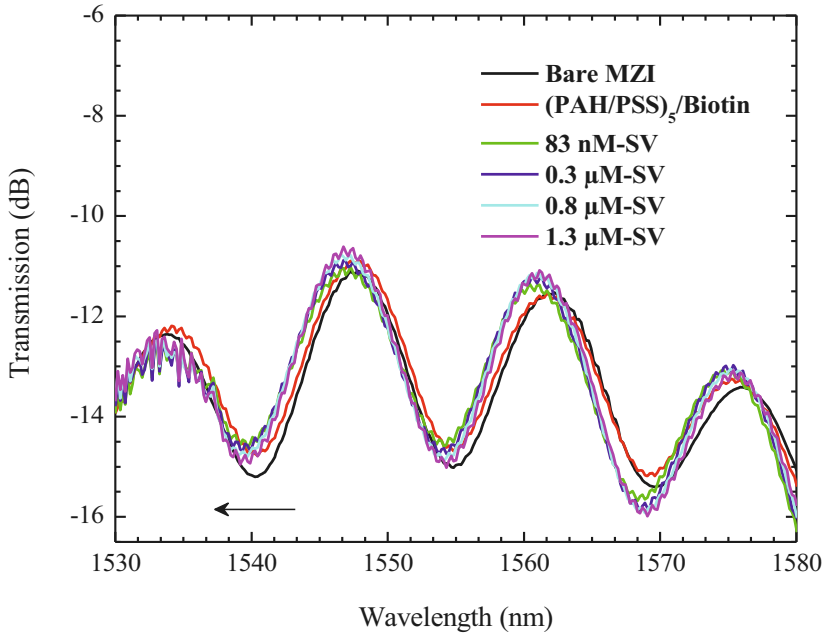

Figure 3-16 Transmission spectra of tapered MZI (5) before and after coating $(PAH/PSS)_5$/Biotin as well as their exposure to streptavidin solutions of different concentrations.

Figure 3-17 shows the wavelength shift of the peak at 1540.17 nm as a function of the concentration of streptavidin. The peak wavelength shift reaches a maximum value of 0.72 nm for streptavidin concentrations of 1.3 μM. The curve shows an increase in the wavelength shift when the concentration of streptavidin increases. Since $\Delta\lambda_{max}$ = 0.72 nm, the sensitivity of MZI (5) is found to be 0.12 nm/(ng/mm^2) using Equation 3-1.

It can be concluded that increasing the number of layers limits the interaction of the evanescent field with the streptavidin, so the sensitivity of the device coated with five bilayers of PAH/PSS is less than that one of the three bilayers of the PAH/PSS.

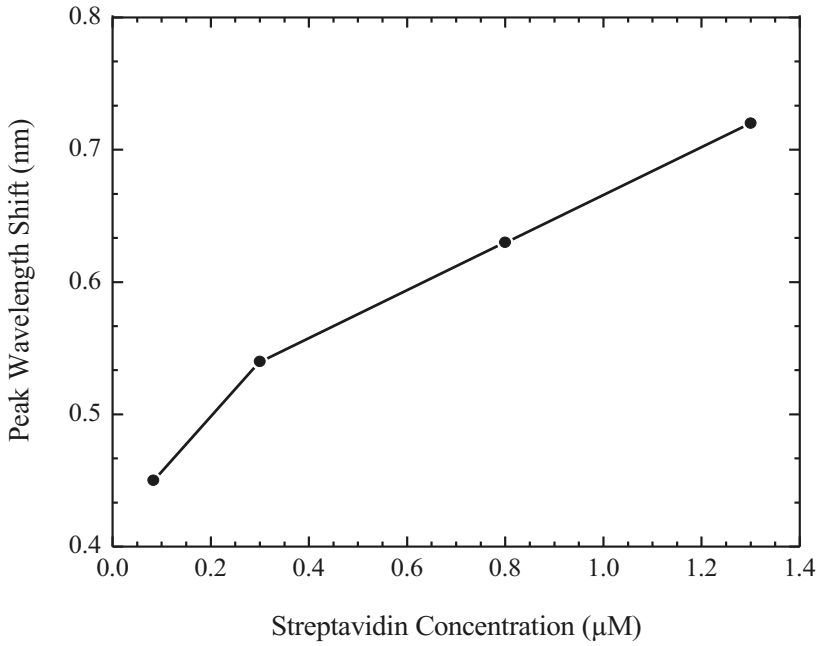

Figure 3-17 Wavelength shift of the peak at 1540.17 nm as a function of streptavidin concentration.

Chapter 4

Conclusion

Due to their unique advantages, optical fiber sensors have been applied in diverse applications for measuring physical, chemical, and biological parameters. Among optical fiber sensor devices, tapered fiber Mach-Zehnder interferometer sensor has the advantages of easy fabrication and high repeatability, among many merits.

In this thesis, the fusion splicing technique is applied for the fabrication of tapered fibers. The effect of changing the arc current, duration, and strain of the fusion splicer on the characteristics of the resultant tapers is studied. The results show that the taper waist decreases with the increment of each one of those settings. Moreover, strain is a significant factor that affects the specifications of the tapers.

The fabrication technique of two types of tapered fiber Mach-Zehnder interferometer, either symmetrical or asymmetrical, is reported in this thesis. Effects of different parameters on the fabrication of the interferometers are studied, which include the separation distance between the two tapers, the propagation direction, and the taper waist size. It is revealed that the separation distance between the two tapers significantly influences the free spectral range of the interference fringes. However, its impact on the extinction ratio is not pronounced.

Three symmetrical tapered fiber MZIs prepared in this study with taper separation distances of 2.0, 3.0, and 4.0 cm exhibit fringe periodicities of 28.0, 16.5, and 12.0 nm, which indicates that the free spectral range decrease with the increasing separation distance between tapers. Meanwhile, the extinction ratios for the fringes of the samples with values of 5.89, 11.17, and 13.05 dB for these three corresponding symmetrical tapered fiber MZIs increase with the increase in the separation distance between tapers. In the case of asymmetrical tapered fiber MZI, the periodicities obtained by the samples with different separation distances between tapers are 26.0, 18.36, and 14.76 nm. It has been found that the free spectral range increases with decreasing separation distance between tapers regardless symmetrical or asymmetrical tapers adopted in the fiber MZI. The maximum extinction ratios of the asymmetrical tapered fiber MZIs are 9.02, 10.5, and 6.44 dB for taper separation distances of 2.0, 3.0, and 4.0 cm, respectively. The highest extinction ratio of 10.5 dB is obtained by the MZI of L_s = 3 cm.

Experiments have also been carried out to investigate the effects of the waist size on the extinction ratios of the fringes for the symmetrical and asymmetrical tapered fiber MZIs. The separation between the tapers in both types of MZI has been fixed at 3.0 cm.

For a symmetrical tapered fiber MZI, three samples prepared in this study with taper waists of 66.0, 62.5, and 58.0 μm manifests corresponding extinction ratios of 2.11, 3.17, and 4.01 dB in the wavelength range from 1586 nm to 1608 nm, indicating the extinction ratio increases with decreasing waist diameter of the symmetrical tapers.

For asymmetrical tapered MZIs prepared in this study with waist diameters of $D1$ = 66.7 and $D2$ = 79.2 μm for MZI 1, $D1$ = 54.2 and $D2$ = 72.2 μm for MZI 2, and $D1$ = 47.2 and $D2$ = 66.7 μm for MZI 3, as well as the tapers lengths $L1$ and $L2$ fixed at ~ 419.0 and 404.9 μm in all three samples, the corresponding extinction ratios for the peak and valley have been observed as 8.85, 3.04, and 7.38 dB in the wavelength range of 1593 nm to 1604 nm when the light propagating from (T1) to (T2). The results obtained in the case of reversed propagation of light are slightly different, showing extinction ratios of 8.39, 2.66, and 8.20 dB, respectively.

Furthermore, symmetrical tapered fiber MZI with a waist diameter of 58.0 μm and taper separation of 4.0 cm is prepared for the purpose of biosensing with an example of streptavidin detection. The layer-by-layer technique has been utilized to achieve multilayered structures based on PAH polymer and SiO_2:Au NPs nanoparticles or PAH and PSS polymers on the surface of the fiber MZI. First, the response of the sensor to streptavidin is studied when three bilayers of (PAH/SiO_2:Au NPs) film are formed and functionalized with biotin. The selected peak in a wavelength ranging from 1546 nm to 1560 nm shows a maximum wavelength shift of 0.36 nm to the shorter wavelength region. The sensor's sensitivity of streptavidin detection is 0.06 nm/(ng/mm^2). On the other hand, when the number of bilayers increased to five and the film is not functionalized with biotin,

the sensitivity increases to 0.07 nm/(ng/mm^2), in which the maximum wavelength shift is 0.45 nm. This can be attributed to the fact that the surface of the gold nanoshells has already been functionalized with lipoic acid so that when the sensor is exposed to biotin, the biotin is weakly attached to their surface. Also, when 7 bilayers are adopted in the devices, a sensitivity of 0.04 nm/(ng/mm^2) has been achieved. On the other hand, the sensors based on PAH/PSS film show sensitivities of 0.29 nm/(ng/mm^2) for three bilayers and 0.12 nm/(ng/mm^2) for five bilayers.

The results show that the highest sensitivity of a particular structure of the sensor can be achieved at certain numbers of the bilayers, i.e. 5 bilayers for (PAH/SiO_2:Au NPs) and 3 bilayers for (PAH/PSS). The sensitivity decreases for either increase or decrease of the numbers of the bilayers.

The results obtained in this study successfully demonstrate the feasibility of streptavidin detection with the symmetrical tapered fiber MZIs developed here. Through this study, the property-structure relationship of these MZIs has been revealed. By optimizing the materials adopted in the multilayered structures or judiciously selecting specifications of multilayers, the sensing performance can be further enhanced. Furthermore, the techniques developed in this study can be explored to detect other biomaterials or to reveal various physical and chemical processes involved in the interactions of light with different functional materials.

Bibliography

[1] G. Rajan, "*Optical fiber sensors: advanced techniques and applications*," New York: Taylor & Francis Group, 2015.

[2] A. Yablon, "*Optical fiber fusion splicing*," Berlin: Springer, 2005.

[3] A. Glass, "Fiber optics," *American Institute of Physics* **46**, 34 (1993).

[4] L. López-Higuera, "*Handbook of optical fibre sensing technology*," New York: Wiley, 2002.

[5] Z. Fang, K. Chin, R. Qu, and H. Cai, "*Fundamentals of optical fiber sensors*," New Jersey: Wiley, 2012.

[6] K. Fidanboylu, and H. Efendioglu, "Fiber optic sensors and their applications," *5th International Advanced Technologies Symposium (IATS'09)* **6**, 1 (2009).

[7] M. Yasin, S. Harun, and H. Arof, "*Fiber optic sensors*," Rijeka: InTech, 2012.

[8] N. Sabri, S. Aljunid, M. Salim, R. Ahmad, and R. Kamaruddin, "Toward optical sensors: review and applications," *Journal of Physics: Conference Series* **423**, 012064 (2013).

[9] X. Dong, H. Tam, and P. Shum, "Temperature-insensitive strain sensor with polarization-maintaining photonic crystal fiber based Sagnac interferometer," *Applied Physics Letters* **90**, 151113 (2007).

[10] Y. Liu, W. Peng, Y. Liang, X. Zhang, X. Zhou, and L. Pan, "Fiber-optic Mach–Zehnder interferometric sensor for high-sensitivity high temperature measurement," *Optics Communications* **300**, 194 (2013).

[11] H. Choi, K. Park, S. Park, U. Paek, B. Lee, and E. Choi, "Miniature fiber-optic high temperature sensor based on a hybrid structured Fabry–Perot interferometer," *Optics Letters* **33**, 2455 (2008).

[12] Y. Ge, J. Zhou, and X. Mao, "Miniature fiber pressure sensor based on fiber etching," *Optik-International Journal for Light and Electron Optics* **124**, 4 (2013).

[13] J. Antonio, J. Sanchez-Mondragon, P. Likamwa, and A. May-Arrioja, "Fiber-optic sensor for liquid level measurement," *Optics Letters* **36**, 3425 (2011).

[14] D. Wu, T. Zhu, M. Deng, D. Duan, L. Shi, J. Yao, and Y. Rao, "Refractive index sensing based on Mach–Zehnder interferometer formed by three cascaded single-mode fiber tapers," *Applied Optics* **50**, 1548 (2011).

[15] V. Bhardwaj and V. Singh, "Fabrication and characterization of cascaded tapered Mach-Zehnder interferometer for refractive index sensing," *Sensors and Actuators A: Physical* **244**, 30 (2016).

[16] Y. Zhu, H. Wang, and Y. Hsu, "The measurement of sucrose concentration by two-tapered all-fiber Mach–Zehnder interferometer employing different coupling structures and manufacture processes," *Optical Review* **23**, 662 (2016).

[17] B. Gholamzadeh, and H. Nabovati, "Fiber optic sensors," *World Academy of Science, Engineering and Technology* **2**, 1107 (2008).

[18] K. Lau, K. Wong, and S. Yeung, "Fiber optic sensors: their principles and fabrication," *Jounral of Chemical Education* **70**, 336 (1993).

[19] P. Tracey, "Intrinsic fiber-optic sensors," *IEEE Transactions on Industry Applications* **27**, 96 (1991).

[20] S. Ghetia, R. Gajjar, and P. Trivedi, "Classification of fiber optical sensors," *International Journal of Electronics Communication and Computer Technology (IJECCT)* **3**, 442 (2013).

[21] H. Li, D. Li, and G. Song, "Recent applications of fiber optic sensors to health monitoring in civil engineering," *Engineering Structures* **26**, 1647 (2012).

[22] B. Lee, Y. Kim, K. Park, J. Eom, M. Kim, B. Rho, and H. Choi, "Interferometric fiber optic sensors," *Sensors* **12**, 2467 (2012).

[23] F. Yu, and S. Yin, "*Fiber optic sensors*," New York, Basel: Marcel Dekker, Inc, 2002.

[24] T. Zhu, D. Wu, M. Liu, and D. Duan, "In-line fiber optic interferometric sensors in single-mode fibers," *Sensors* **12**, 10430 (2012).

[25] P. Lu, L. Men, K. Sooley, and Q. Chen, "Tapered fiber Mach–Zehnder interferometer for simultaneous measurement of refractive index and temperature," *Applied Physics Letters* **94**, 131110 (2009).

[26] J. Hsu, C. Lee, H. Chang, W. Shih, and C. Li, "Highly sensitive tapered fiber Mach–Zehnder interferometer for liquid level sensing," *IEEE Photonics Technology Letters* **25**,1354 (2013).

[27] B. Li, L. Jiang, S. Wang, Q. Wang, and J. Yang, "A new Mach-Zehnder interferometer in a thinned-cladding fiber fabricated by electric arc for high sensitivity refractive index sensing," *Optics and Lasers in Engineering* **50**, 829 (2012).

[28] J. Yang, L. Jiang, S. Wang, B. Li, M. Wang, H. Xiao, Y. Lu, and H. Tsai, "High sensitivity of taper-based Mach–Zehnder interferometer embedded in a thinned optical fiber for refractive index sensing," *Applied Optics* **50**, 5503 (2011).

[29] Q. Zhang, X. Zeng, F. Pang, M. Wang, and T. Wang, "Switchable multiwavelength fiber laser by using a compact in-fiber Mach–Zehnder interferometer," *Journal of Optics* **14**, 045403 (2012).

[30] F. Pang, H. Liu, H. Guo, Y. Liu, X. Zeng, N. Chen, Z. Chen, and T. Wang, "In-fiber Mach–Zehnder interferometer based on double cladding fibers for refractive index sensor," *IEEE Sensors Journal* **11**, 2395 (2011).

[31] Z. Tian, S. Yam, and H. Loock, "Single-mode fiber refractive index sensor based on core-offset attenuators," *IEEE Photonics Technology Letters* **20**, 1387 (2008).

[32] M. Sun, Y. Jin, and X. Dong, "All-fiber Mach–Zehnder interferometer for liquid level measurement," *IEEE Sensors Journal* **15**, 3984 (2015).

[33] D. Wu, T. Zhu, K. Chiang, and M. Deng, "All single-mode fiber Mach–Zehnder interferometer based on two peanut-shape structures," *Journal of Lightwave Technology* **30**, 805 (2012).

[34] G. Yin, S. Lou, and H. Zou, "Refractive index sensor with asymmetrical fiber Mach-Zehnder interferometer based on concatenating single-mode abrupt taper and core-offset section," *Optics & Laser Technology* **45**, 294 (2013).

[35] H. Wang, H. Meng, R. Xiong, Q. Wang, B. Huang, X. Zhang, W. Yu, C. Tan, and X. Huang, "Simultaneous measurement of refractive index and temperature based on asymmetric structures modal interference," *Optics Communications* **364**, 191 (2016).

[36] A. Dutta, B. Deka, and P. Sahu, "*Planar waveguide optical sensors from theory to applications*," Switzerland: Springer, 2016.

[37] B. Culshaw, "The optical fibre Sagnac interferometer: an overview of its principles and applications," *Measurement Science and Technology* **17**, R1 (2006).

[38] J. Kang, "*Fiber optic sensing and imaging*," New York: Springer, 2013.

[39] C. Zamarreño, I. Matías, and F. Arregui, "Nanofabrication techniques applied to the development of novel optical fiber sensors based on nanostructured coatings," *IEEE Sensors Journal* **12**, 2699 (2012).

[40] A. Lokman, H. Arof, S. Harun, Z. Harith, H. Rafaie, and R. Nor, "Optical fiber relative humidity sensor based on inline Mach–Zehnder interferometer with ZnO nanowires coating," *IEEE Sensors Journal* **16**, 312 (2016).

[41] B. Shivananju, S. Yamdagni, R. Fazuldeen, A. Kumar, S. Nithin, M. Varma, and S. Asokan, "Highly sensitive carbon nanotubes coated etched fiber Bragg grating sensor for humidity sensing," *IEEE Sensors Journal* **14**, 2615 (2014).

[42] K. Dissanayake, W. Wu, H. Nguyen, T. Sun, and K. Grattan, "Graphene-oxide-coated long-period grating-based fiber optic sensor for relative humidity and external refractive index," *Journal of Lightwave Technology* **36**, 1145 (2018).

[43] Y. Chiu, C. Wu, and C. Chiang, "Tilted fiber Bragg grating sensor with graphene oxide coating for humidity sensing," *Sensors* **17**, 1 (2017).

[44] X. Luo, A. Mrrin, A. Killard, and M. Smyth, "Application of nanoparticles in electrochemical sensors and biosensors," *Electroanalysis* **18**, 319 (2006).

[45] H. Liu, Y. Miao, B. Liu, W. Lin, H. Zhang, B. Song, M. Huang, and L. Lin, "Relative humidity sensor based on s-taper fiber coated with SiO_2 nanoparticles," *IEEE Sensors Journal* **15**, 3424 (2015).

[46] S. James, and R. Tatam, "Fibre optic sensors with nano-structured coatings," *Journal of Optics A: Pure and Applied Optics* **8**, S430 (2006).

[47] I. Peterson, "Langmuir-blodgett films," *Journal of Physics D: Applied Physics* **23**, 379 (1990).

[48] M. Petty, "*Langmuir-Blodgett films*," New York: Cambridge University Press, 1996.

[49] G. Decher, J. Hong, and J. Schmitt, "Buildup of ultrathin multilayer films by a self-assembly process: III. consecutively alternating adsorption of anionic and cationic polyelectrolytes on charged surfaces," *Thin Solid Films* **210**, 831(1992).

[50] M. Aliofkhazraei, "*Anti-abrasive nanocoatings: current and future applications*," Sawston: Elsevier, 2015.

[51] S. Vozar, Y. Poh, T. Serbowicz, M. Bachner, P. Podsiadlo, M. Qin, E. Verploegen, N. Kotov, and A. Hart, "Automated spin-assisted layer-by-layer assembly of nanocomposites," *Review of Scientific Instruments* **80**, 023903 (2009).

[52] Y. Li, X. Wang, and J. Sun, "Layer-by-layer assembly for rapid fabrication of thick polymeric films," *Chemical Society Reviews* **41**, 5998 (2012).

[53] S. Korposh, S. James, S. Lee, S. Topliss, S. Cheung, W. Batty, and R. Tatam, "Fiber optic long period grating sensors with a nanoassembled mesoporous film of SiO_2 nanoparticles," *Optics Express* **18**, 13227 (2010).

[54] S. Korposh, S. Lee, S. James, and R. Tatam, "Refractive index sensitivity of fibre-optic long period gratings coated with SiO_2 nanoparticle mesoporous thin films," *Measurement Science and Technology* **22**, 075208 (2011).

[55] F. Tian, X. Li, J. Kanka, and H. Du, "Fiber optic index sensor enhanced by gold nanoparticle assembly on long period grating," *Optik* **132**, 445 (2017).

[56] A. Socorro, I. Villar, J. Corres, F. Arregui, and I Matias, "Tapered single-mode optical fiber pH sensor based on lossy mode resonances generated by a polymeric thin-film," *IEEE Sensors Journal* **12**, 2598 (2012).

[57] C. Zamarreño, M. Hernaez, P. Sanchez, I. Villar, I. Matias, and F. Arregui, "Optical fiber humidity sensor based on lossy mode resonances supported by TiO_2/PSS Coatings," *Procedia Engineering* **25**, 1385 (2011).

[58] D. Lopez-Torresa, C. Elosuaa, J. Villatoroc, J. Zubiac, M. Rothhardte, K. Schustere, and F. Arreguia, "Photonic crystal fiber interferometer coated with a PAH/PAA nanolayer as humidity sensor," *Sensors & Actuators: B. Chemical* **242**, 1065 (2017).

[59] P. Rivero, A. Urrutia, J. Goicoechea, and F. Arregui, "Optical fiber humidity sensors based on localized surface plasmon resonance LSPR and lossy-mode resonance LMR in overlays loaded with silver nanoparticles," *Sensors & Actuators: B. Chemical* **173**, 244 (2012).

[60] Q. Li, X. Zhang, H. He, Q. Meng, J. Shi, J. Wang, and W. Dong, "Improved detecting sensitivity of long period fiber gratings by polyelectrolyte multilayers: the effect of film structures," *Optics Communications* **331**, 39 (2014).

[61] Q. Li, X. Zhang, Y. Yu, Y. Qian, W. Dong, Y. Li, J. Shi, J. Yan, and H. Wanga, "Enhanced sucrose sensing sensitivity of long period fiber grating by self-assembled polyelectrolyte multilayers," *Reactive and Functional Polymers* **71**, 335 (2011).

[62] L. Marques, F. Hernandez, S. James, S. Morgan, M. Clark, R. Tatam, and S. Korposh, "Highly sensitive optical fibre long period grating biosensor anchored with silica core gold shell nanoparticles," *Biosensors and Bioelectronics* **75**, 222 (2016).

[63] Z. Wang, J. Heflin, K. Cott, R. Stolen, S. Ramachandran, and S. Ghalmi, "Biosensors employing ionic self-assembled multilayers adsorbed on long-period fiber gratings," *Sensors and Actuators B: Chemical* **139**, 618 (2009).

[64] Z. Wang, J. Heflin, R. Stolen, and S. Ramachandran, "Highly sensitive optical response of optical fiber long period gratings to nanometer-thick ionic self-assembled multilayers," *Applied Physics Letters* **86**, 223104 (2005).

[65] Y. Lin, Y. Zou, Y. Mo, J. Guo, and R. Lindquist, "E-Beam patterned gold nanodot arrays on optical fiber tips for localized surface plasmon resonance biochemical sensing," *Sensors* **10**, 9397 (2010).

[66] Y. Lin, Y. Zou, and R. Lindquist, "A reflection-based localized surface plasmon resonance fiber-optic probe for biochemical sensing," *Biomedical Optics Express* **2**, 478 (2011).

[67] P. Pilla, P. Manzillo, V. Malachovska, A. Buosciolo, S. Campopiano, A. Cutolo, L. Ambrosio, M. Giordano, and A. Cusano, "Long period grating working in transition mode as promising technological platform for label-free biosensing," *Optics Express* **17**, 20039 (2009).

[68] S. Cheng and L. Chau, "Colloidal gold-modified optical fiber for chemical and biochemical sensing," *Analytical Chemistry* **75**, 16 (2003).

[69] J. Tang, S. Cheng, W. Hsu, T. Chiang, and L. Chau, "Fiber-optic biochemical sensing with a colloidal gold-modified long period fiber grating," *Sensors & Actuators: B. Chemical* **119**, 105 (2006).

[70] B. Gu, M. Yin, A. Zhang, J. Qian, and S. He, "Low-cost high-performance fiber-optic pH sensor based on thin-core fiber modal interferometer," *Optics Express* **17**, 22296 (2009).

[71] L. Shao, M. Yim, H. Tam, and J. Albert, "Fiber optic pH sensor with self-assembled polymer multilayer nanocoatings," *Sensors* **13**, 1425 (2013).

[72] T. Yadav, R. Narayanaswamy, M. Abu Bakar, Y. Kmail, and M. Mahdi, "Single mode tapered fiber-optic interferometer based refractive index sensor and its application to protein sensing," *Optics Express* **22**, 22802 (2014).

[73] R. Jarzebinska, S. Korposh, S. James, W. Batty, R. Tatam, and S. Lee, "Optical gas sensor fabrication based on porphyrin-anchored electrostatic self-assembly onto tapered optical fibers," *Analytical Letters* **45**, 1297 (2012).

[74] K. Kieu and M. Mansuripur, "Biconical fiber taper sensors," *IEEE Photonics Technology Letters* **18**, 2239 (2006).

[75] M. Zibaii, H. Latifi, M. Karami, M. Gholami, S. Hosseini, and M. Ghezelayagh, "Non-adiabatic tapered optical fiber sensor for measuring the interaction between α-amino acids in aqueous carbohydrate solution," *Measurement Science and Technology* **21**, 105801 (2010).

[76] H. Latifi, M. Zibaii, S. Hosseini, and P. Jorge, "Nonadiabatic tapered optical fiber for biosensor applications," *Photonic Sensors* **2**, 340 (2012).

[77] J. Love, W. Henry, W. Stewart, R. Black, S. Lacroix, and F. Gonthier, "Tapered single-mode fibres and devices. Part 1: adiabaticity criteria," *IEEE Proceedings J Optoelectronics* **138**, 343 (1991).

[78] Z. Tian and S. Yam, "In-line abrupt taper optical fiber Mach–Zehnder interferometric strain sensor," *IEEE Photonics Technology Letters* **21**, 161 (2009).

[79] B. Musa, Y. Kamil, M. Abu Baker, A. Noor, A. Ismail, and A. Mahdi, "Effects of taper parameters on free spectral range of non-adiabatic tapered optical fibers for sensing applications," *Microwave and Optical Technology Letters* **58**, 798 (2016).

[80] A. Leung, P. Shankar, and R. Mutharasan, "A review of fiber-optic biosensors," *Sensors and Actuators B: Chemical* **125**, 688 (2007).

[81] L. Xu, Y. Li, and B. Li, "Nonadiabatic fiber taper-based Mach-Zehnder interferometer for refractive index sensing," *Applied Physics Letters* **101**, 153510 (2012).

[82] D. Monzón-Hernández, V. Minkovich, and J. Villatoro, "High temperature sensing with tapers made of microstructured optical fiber," *IEEE Photonics Technology Letters* **18**, 511 (2006).

[83] J. Chandalia, B. Eggleton, R. Windeler, S. Kosinski, X. Liu, and C. Xu, "Adiabatic coupling in tapered air-silica microstructured optical fiber," *IEEE Photonics Technology Letters* **13**, 52 (2001).

[84] S. Harun, K. Lim, A. Jasim, and H. Ahmad, "Dual wavelength erbium-doped fiber laser using a tapered fiber," *Journal of Modern Optics* **57**, 2111 (2010).

[85] Y. Tian, W. Wang, N. Wu, X. Zou, and X. Wang, "Tapered optical fiber sensor for label-free detection of biomolecules," *Sensors* **11**, 3780 (2011).

[86] T. Dimmick, G. Kakarantzas, T. Birks, and P. Russell, "Carbon dioxide laser fabrication of fused-fiber couplers and tapers," *Applied Optics* **38**, 6845 (1999).

[87] B. Li, L. Jiang, S. Wang, J. Yang, M. Wang, and Q. Chen, "High sensitivity Mach–Zehnder interferometer sensors based on concatenated ultra-abrupt tapers on thinned fibers," *Optics & Laser Technology* **44**, 640 (2012).

[88] D. Wu, Y. Zhao, and J. Li, "PCF taper-based Mach–Zehnder interferometer for refractive index sensing in a PDMS detection cell," *Sensors and Actuators B: Chemical* **213**, 1 (2015).

[89] B. Li, L. Jiang, S. Wang, L. Zhou, H. Xiao, and H. Tsai, "Ultra-abrupt tapered fiber Mach-Zehnder interferometer sensors," *Sensors* **11**, 5729 (2011).

[90] Y. Xu, P. Lu, Z. Qin, J. Harris, F. Baset, P. Lu, V. Bhardwaj, and X. Bao, "Vibration sensing using a tapered bend-insensitive fiber based Mach-Zehnder interferometer," *Optics Express* **21**, 3031 (2013).

[91] Y. Li, L. Chen, E. Harris, and X. Bao, "Double-pass in-line fiber taper Mach–Zehnder interferometer sensor," *IEEE Photonics Technology Letters* **22**, 1750 (2010).

[92] C. Bariain, I. Matias, F. Arregui, M. Lopez-Amo, "Optical fiber humidity sensor based on a tapered fiber coated with agarose gel," *Sensors and Actuators B: Chemical* **69**, 127 (2000).

[93] J. Shi, S. Xiao, L. Yi, M. Bi, "A sensitivity-enhanced refractive index sensor using a single-mode thin-core fiber incorporating an abrupt taper," *Sensors* **12**, 4697 (2012).

[94] Q. Wang, W. Wei, M. Guo, and Y. Zhao, "Optimization of cascaded fiber tapered Mach–Zehnder interferometer and refractive index sensing technology," *Sensors and Actuators B: Chemical* **222**, 159 (2016).

[95] Y. Zhao, L. Cai, and H. Hu, "Fiber-optic refractive index sensor based on multi-tapered SMS fiber structure," *IEEE Sensors Journal* **15**, 6348 (2015).

[96] P. Wang, L. Bo, Y. Semenova, G. Farrell, and G. Brambilla, "Optical microfibre based photonic components and their applications in label-free biosensing," *Biosensors* **5**, 471 (2015).

[97] M. Zibaii, H. Latifi, Z. Saeedian, and Z. Chenari, "Nonadiabatic tapered optical fiber sensor for measurement of antimicrobial activity of silver nanoparticles against escherichia coli," *Journal of Photochemistry & Photobiology, B: Biology* **135**, 55 (2014).

[98] M. Ahmad and L. Hench, "Effect of taper geometries and launch angle on evanescent wave penetration depth in optical fibers," *Biosensors and Bioelectronics* **20**,1312 (2005).

[99] Y. Kamil, M. Abu Bakar, M. Mustapa, M. Yaacob, N. Abidin, A. Syahir, H. Lee, and M. Mahdi, "Label-free Dengue E protein detection using a functionalized tapered optical fiber sensor," *Sensors & Actuators: B. Chemical* **257**, 820 (2018).

[100] J. Ding, A. Zhang, L. Shao, J. Yan, and S. He, "Fiber-taper seeded long-period grating pair as a highly sensitive refractive-index sensor," *IEEE Photonics Technology Letters* **17**, 1247 (2005).

[101] G. Cardenas-Sevilla, D. Monzon-Hernandez, I. Torres-Gomez, A. Martinez-Rios, "Tapered Mach–Zehnder interferometer based on two mechanically induced long-period fiber gratings as refractive index sensor," *Optics & Laser Technology* **44**, 1516 (2012).

[102] F. Xia, Y. Zhao, and M. Chen, "Optimization of Mach–Zehnder interferometer with cascaded up-tapers and application for curvature sensing," *Sensors and Actuators A: Physical* **263**, 140 (2017).

[103] H. Kim and A. Gnauck, "Chirp characteristics of dual-drive Mach–Zehnder modulator with a finite DC extinction ratio," *IEEE Photonics Technology Letters* **14**, 298 (2002).

[104] F. Arregui, "*Sensors based on nanostructured materials*," New York: Springer Science.Business Media, LLC, 2009.

[105] M. Ventra, S. Evoy, and J. Heflin "*Introduction to nanoscale science and technology*," Boston: Kluwer Academic Publishers, 2004.

[106] C. Zamarreñoa, M. Hernaeza, P. Sancheza, I. Villara, I. Matiasa, and F. Arreguia, "Optical fiber humidity sensor based on lossy mode resonances supported by TiO_2/PSS coatings," *Procedia Engineering* **25**, 1385 (2011).

[107] J. Corres, F. Arregui, and I. Matias, "Design of humidity sensors based on tapered optical fibers," *Journal of Lightwave Technology* **24**, 4329 (2006).

[108] J. Corres, I. Matias, M. Hernaez, J. Bravo, and F. Arregui, "Optical fiber humidity sensors using nanostructured coatings of SiO_2 nanoparticles," *IEEE Sensors Journal* **8**, 281 (2008).

[109] M. Jiang, Q. Li, J. Wang, W. Yao, Z. Jin, Q. Sui, J. Shi, F. Zhang, L. Jia, and W. Dong, "Optical response of fiber-optic Fabry-Perot refractive-index tip sensor coated with polyelectrolyte multilayer ultra-thin films," *Journal of Lightwave Technology* **31**, 2321 (2013).

[110] Z. Tou, C. Chan, and S. Leong, "A fiber-optic pH sensor based on polyelectrolyte multilayers embedded with gold nanoparticles," *Measurement Science and Technology* **25**, 075102 (2014).

[111] S. Korposh, R. Selyanchyn, W. Yasukochi, S. Lee, S. James, and R. Tatam, "Optical fibre long period grating with a nanoporous coating formed from silica nanoparticles for ammonia sensing in water," *Materials Chemistry and Physics* **133**, 784 (2012).

[112] L. Chena, C. Chan, K. Ni, P. Hu, T. Li, W. Wong, P. Balamurali, R. Menon, M. Shaillender, B. Neu, C. Poh, X. Dong, X. Ang, P. Zu, Z. Tou, and K. Leong, "Label-free fiber-optic interferometric immunosensors based on waist-enlarged fusion taper," *Sensors and Actuators B: Chemical* **178**, 176 (2013).

[113] M. Wan, P. Luo, J. Jin, J. Xing, Z. Wang, and S. Wong, "Fabrication of localized surface plasmon resonance fiber probes using ionic self-assembled gold nanoparticles," *Sensors* **10**, 6477 (2010).

[114] Y. Yong-jiang, Z. Ying, L. Qiu-shun, Y. Yan, S. Jian-guo, L. Ming-yu, Y. Wei-guo, W. Jun-nan, D. Wen-fei, and Q. Zhi-mei, "In situ molecular self-assembly and sensitive label-free detection of streptavidin via a wavelength interrogated surface plasmon resonance sensor," *Chemical Research in Chinese Universities* **29**, 1219 (2013).

[115] C. Barrios, M. Banuls, V. Gonzalez-Pedro, K. Gylfason, B. Sanchez, A. Griol, A. Maquieira, H. Sohlstrom, M. Holgado, and R. Casquel, "Label-free optical biosensing with slot waveguides," *Optics Letters* **33**,708 (2008).

[116] W. Yu, T. Lang, J. Bian, and W. Kong, "Label-free fiber optic biosensor based on thin-core modal interferometer," *Sensors and Actuators B: Chemical* **228**, 322 (2016).

[117] H. Li, S. Park, J. Reif, T. Labean, and H. Yan, "DNA-templated self-assembly of protein and nanoparticle linear arrays," *Journal of the American Chemical Society* **126**, 418 (2004).